THE KINEMATICS OF IONIZED GAS IN NEARBY, EDGE-ON GALAXIES FROM MULTI-LONG-SLIT SPECTROSCOPY

BY

CATHARINE ELIZABETH WU, B.A., M.S.

A dissertation submitted to the Graduate School

in partial fulfillment of the requirements

for the degree

Doctor of Philosophy

Major Subject: Astronomy

New Mexico State University

Las Cruces New Mexico

November 2014

"The Kinematics of Ionized Gas in Nearby, Edge-on Galaxies from Multi-long-slit Spectroscopy," a dissertation prepared by Catharine E. Wu in partial fulfillment of the requirements for the degree, Doctor of Philosophy, has been approved and accepted by the following:

Dr. Loui Reyes
Dean of the Graduate School

Rene A. M. Walterbos
Chair of the Examining Committee

Date

Committee in charge:

Dr. Rene A. M. Walterbos, Chair

Dr. Christopher W. Churchill

Dr. Jon Holtzman

Dr. Daniel P. Dugas

DEDICATION

For Grandpa Wu, Aunt Lily, Grandma and Grandpa Harmison, Grandma Kuehn, and TC — I think you would have thought this was pretty cool.

ACKNOWLEDGMENTS

This research was supported by an award from Research Corporation for the Advancement of Science. I also acknowledge support from NSF grant AST-0908126.

This research is based on observations obtained with the Apache Point Observatory 3.5-meter telescope, which is owned and operated by the Astrophysical Research Consortium. I am very grateful for the Observing Specialists and staff and for all of their help.

I extend a special thank you to the HALOGAS team for providing instrumental feedback and support, especially during the early stages of this research project.

And many thanks to my girls, Chloe and Kelbee, for literally being by my side, convincing me to take breaks and go for walks, dealing with my unwanted hugs, tolerating those halloween costumes, and protecting me from men with beards; my fellow '05-ers, Wes peeps, India buddies (especially Erik and Vigeesh), and Puerto Rico crew for keeping academics fun; Jillian, Liz, Paul, Joe, Ling-Hong, Sean, Kirk, Ryan, Allison, Glenn, and Brandon for late night office shenanigans and for making my time in LC pretty freakin' fun; Maria for technical help and sanity checks at all hours of the night and day and for being a great travel buddy; Candace for the girls' nights; my OMTRS buddies for rock climbing, 18-hour hikes in the Organs, searching, and rescuing; Dom, Aaron, Malynda, and Bob for being my gymnastics buddies; Chas, Ryan, and AGSO films for comic relief; Jeff for making the greatest dissertation template; Ofelia and Lorenza for performing magic; Orion, Inishi, and their parents for the doggie dates; Cosmo, Mei Mei, and

Lupin for the entertainment; Downstairs for complementing my healthy diet with leftover pizza and eating every meal at home with 4 hopeful eyes staring at him; Sussman and Adam for turning 121 planetary; Jean and Sean for turning 121 blond; and The Council of Elders, the WIA group, Body by Scoti, the IM softball teams, and everyone else for making this department a pretty awesome one.

Teresa, Kenza, Diane, Carlos, Jacob, Hayden — thank you SO MUCH for being my practice audience. Jean, thank you for all the printing and proof-reading help.

Cat — I mean Liz — thank you for being the twin I never had.

To my parents and sisters, thank you for all your support.

Rock climbing in Jordan, hanging out at the pyramids in Cairo, Rhine River boat tour, German beer fests, playing cricket in Bangalore, water buffalo in southern India, hiking in the Himalayas, visiting the Taj Mahal, star-gazing at Arecibo, floating in the Dead Sea, throwing tennis balls (with permission) into the largest radio dish in existence, caving in Hungary, swimming in a bioluminescent bay in Puerto Rico, and being the winning pitcher in the Women's IM Softball Championship game.

I took the scenic route, but I made it.

VITA

EDUCATION

2010 M.S., Astronomy
New Mexico State University
Las Cruces, New Mexico, USA

2003 B.A., Astronomy and Physics, with Honors
Wesleyan University
Middletown, Connecticut, USA

AWARDS AND GRANTS

2014 NMSU Alumni Association Outstanding Graduate Award

2007-2010 NM Higher Education Department Scholarship for Women in Science

2007-2009 NM Space Grant Consortium Graduate Research Fellowship

2007 NMSU Astronomy Pegasus Award for Excellence in Teaching

PROFESSIONAL ORGANIZATIONS

American Astronomical Society

PUBLICATIONS

Wu, C.E., Waterbos, R., Choi, J., Rand, R.J. 2012, in EAS Publication Series 56, The Role of the Disk-Halo Interaction in Galaxy Evolution: Outflow vs. Infall?, ed. Miguel A. de Avillez (Les Ulis Cedex A, France: EDP Sciences), 121. *Halo Gas Velocities of NGC 4244 and NGC 891 Using Multi-Long-Slit Spectroscopy*

FIELD OF STUDY

Major Field: Galaxy Thick Disks and Halos

ABSTRACT

THE KINEMATICS OF IONIZED GAS IN NEARBY, EDGE-ON GALAXIES FROM MULTI-LONG-SLIT SPECTROSCOPY

BY

CATHARINE ELIZABETH WU, B.A., M.S.

Doctor of Philosophy

New Mexico State University

Las Cruces, New Mexico, 2014

Dr. Rene A.M. Walterbos, Chair

Several galaxies show decreasing rotational velocities of hydrogen gas with increasing height above the disk. This is likely due to a combination of outflowing gas from galactic fountains and infalling gas with lower angular momentum from the CGM, IGM or satellite accretion. The degree to which each scenario contributes to a galaxy's extra-planar (EP) gas affects the velocity gradient and has implications for halo formation and evolution. Until recently, it was believed that most of this gas originates from fountain flows, but simulations have shown that as much as 15% of observed EP gas is infalling material. To study the behavior of ionized EP gas, we present optical observations of 13 edge-on galaxies from a multi-slit spectroscopic setup on the ARC 3.5m telescope at Apache Point Observatory, NM. Our setup allows us to measure velocities of H-alpha-emitting gas

as a function of height above the midplane in 11 radial distance bins in a single exposure. Our sample covers a range of star formation rates (L_{FIR}/D_{25}^2 of 0.03 – 8.9×10^{40}) and includes active and passive galaxies. To aid in the analysis of our spectra, which suffer from projection effects due to our targets' edge-on nature, we developed modeling software for our multi-slit setup. We detect lagging EP gas in four galaxies. NGC 891, NGC 4517, and NGC 4565 have large lags that likely originate from galactic fountain flows and accretion of lower angular momentum material. NGC 4631 has a small lag on its west side that is likely from fountain flows alone. We find evidence of a warped spiral arm on the east side of NGC 4631 and large outflows near the center of the galaxy. Three galaxies (NGC 3628, NGC 4013, NGC 5907) have non-lagging EP gas. Two galaxies (NGC 3044, NGC 3079) show EP gas with complicated kinematics, and we cannot determine if the gas is lagging. We detected no EP gas in three galaxies (UGC 4278, NGC 5229, UGC 7321), and we had one non-detection (NGC 4762). We see no trend between lagging gas and star formation, but the extent of EP gas does appear to be correlated with star formation.

Contents

LIST OF TABLES

LIST OF FIGURES

1. INTRODUCTION

Substantial amounts of material have been observed above and below the star-forming disks of spiral galaxies. This extraplanar material forms a thick disk and acts as the interface between the thinner star-forming disk, the halo, and the intergalactic medium (IGM). Its behavior can lend insight to the formation and evolution of galaxy disks and their halos, and it has implications for refueling mechanisms to replenish gas that has been lost to star formation. Thick disks in external galaxies have been shown to be multi-phase environments, with observations showing spatially extensive components in x-ray (e.g. Strickland et al. 2004a; Tüllmann et al. 2006), radio continuum (e.g. Dahlem et al. 2006), dust (e.g. Howk & Savage 1999a; Alton et al. 2000; Ménard et al. 2010), neutral hydrogen (e.g. Fraternali et al. 2002; Oosterloo et al. 2007; Heald et al. 2011), and ionized gas (e.g. Rand 1996; Hoopes et al. 1999; Rossa & Dettmar 2000).

1.1. Ionized Extraplanar Gas

Nearby, edge-on spiral galaxies provide the opportunity to study extraplanar (EP) gas with no confusion from gas in the disk. Optical observations of such galaxies show substantial amounts of EP diffuse ionized gas (DIG) up to a few kpc above the midplane. This diffuse gas often has a varied morphology, ranging from smooth and extended to being dominated by filaments, loops, or structures concentrated near the galactic nucleus (e.g. Rand 1996; Hoopes et al. 1999; Rossa & Dettmar 2000). Observations of the Milky Way also show diffuse Hα emission in a thick layer above the disk, which is referred to as the Reynolds layer or the warm ionized medium (WIM). Most of the Galaxy's ionized gas (by mass) is contained

in this layer (Haffner et al. 2009; Reynolds 1990).

The extent and thickness of EP DIG have been shown to be correlated with star formation rates in the underlying disk (e.g. Lehnert & Heckman 1996; Rossa & Dettmar 2000; Heald et al. 2007). Higher rates of star formation lead to more galactic winds and supernovae, which are capable of puffing up a galaxy's EP gas layer, and massive stars and supernovae in the disk provide an ionization source for this gas.

1.2. Galactic Fountain Flows as a Possible Origin

There has been much debate about the origin of EP gas. Shapiro & Field (1976) and Bregman (1980) described a galactic fountain mechanism as the primary origin of gas in thick disks and halos. Hot gas in the disk is expelled by supernovae, and as it rises, its rotational velocity slows. It moves radially outward to conserve angular momentum. If it cools sufficiently quickly, it will fall back to the disk, completing the cycle of the fountain. This fountain model can therefore explain the presence of EP gas. It also predicts an EP component with a decrease in rotational velocity as height increases above the disk, and this phenomenon has been observed in several galaxies in both HI (e.g. Swaters et al. 1997; Oosterloo et al. 2007; Zschaechner et al. 2011; Gentile et al. 2013; Kamphuis et al. 2013) and ionized gas (e.g. Rand 1997; Heald et al. 2007). NGC 891, which has a high star formation rate and thick HI and ionized gas disks, was one of the first galaxies in which a lagging component was observed (Rand 1997; Swaters et al. 1997), and vertical velocity gradients for this and a handful of other galaxies were used to test the idea that EP gas primarily has a galactic fountain origin. Fraternali & Binney

(2006) and Collins et al. (2002) found that this is not the case. They showed that ballistic models of fountain flows as a means of generating a neutral or ionized thick disk for a galaxy such as NGC 891 produce velocity gradients that are too shallow compared to observations by roughly an order of magnitude.

One way to further slow the rotation of the EP gas would be accretion of low-angular momentum material in addition to fountain flows, resulting in a steeper vertical velocity gradient. Fraternali & Binney (2008) modeled the halos of NGC 891 and NGC 2403 as ballistic fountain flows with accretion of external cold, infalling clouds. They assumed accretion rates roughly equal to the star formation rates in each galaxy, and their simulated halos successfully reproduced the observed velocity gradients. Their models indicate that accreted gas constitutes 10-20% of EP gas, and the remaining 80-90% of the gas is from galactic fountain flows.

Fraternali et al. (2007) and Marinacci et al. (2011) investigated whether fountain flows interacting with an almost-static, hot corona can explain observed velocity gradients. Models by Fraternali et al. (2007) indicate that a hot corona cannot cause a steeper velocity gradient because the coronal gas spins up on short timescales, while cosmological simulations by Marinacci et al. (2011) indicate that a hot corona can cause a steeper lag. However, regardless of whether factors internal to a galaxy are a viable option for steepening the vertical velocity gradient, there are ample indications that external factors may play a non-trivial role.

1.3. Additional Evidence for Accretion

HI observations of the Milky Way and external galaxies indicate that accretion is an important process in shaping the structure and behavior of EP gas. Fraternali et al. (2001) observed a substantial amount of gas (∼10% of the total HI mass) with anomalous velocities in NGC 2403, which has an extended HI layer with fairly regular kinematics. Boomsma et al. (2005) observed plumes extending up to 12 kpc from the midplane in NGC 253, a nuclear starburst galaxy. Thilker et al. (2004) observed clouds in the halo of M31 that are either from tidal streams or accretion of IGM. Oosterloo et al. (2007) found a plume extending up to 22 kpc from the midplane and counter-rotating clouds in the halo of NGC 891. Coherent plumes can be explained by a starburst event, but this is unlikely for plumes as extensive as those in NGC 253 and NGC 891. Counter-rotating gas cannot be explained by disk-driven fountain flows. Instead, a non-galactic fountain origin, such as accretion of material from an external source, is a more likely scenario for both phenomena. In particular, extended filaments could be tidally stretched, infalling companions.

In addition to coherent plumes and counter-rotating clouds, van der Hulst & Sancisi (2005) found HI bridges connecting NGC 3359 and NGC 6946 to smaller companion galaxies. Wannier & Wrixon (1972) were the first to observe the Magellanic Stream in our own Galaxy, and Wakker & van Woerden (1997), Lockman (2004), and Richter (2012) have all studied high velocity clouds (HVCs) within the Milky Way. HVCs are most likely the result of cold gas accretion, possibly from minor mergers with small companions.

In general, warps, asymmetric spatial extents, and kinematic lopsidedness are

almost ubiquitous characteristics of galaxy disks. All of these point to accretion of the IGM or minor mergers playing a role in the evolution of these galaxies, even if no coherent counterpart can be detected.

Further evidence for accretion comes from observed star formation rates (SFRs). SFRs in spiral galaxies indicate that there must be an external source of gas to maintain star formation, otherwise they would use up their available gas supply on timescales shorter than their lifetimes (Larson et al. 1980). More specifically, several studies have shown that a large amount of this external gas is likely ionized. In the Milky Way, neutral hydrogen gas from satellite galaxies and HI clouds in the halo do not provide enough material to maintain star formation at current rates (Grcevich & Putman 2009). Lehner & Howk (2011) found that gas from ionized HVCs in the local Galactic halo can provide enough infalling material to sustain observed SFRs in our Galaxy. Hydrodynamic simulations of a Milky Way-mass galaxy at redshift $\sim$0 show that accretion rates of ionized hydrogen are much greater than those of neutral hydrogen gas (Joung et al. 2012), and direct evidence of infalling ionized gas is seen in our own Galaxy, where the WIM layer shows low-velocity infall toward the disk (Haffner et al. 2003).

If infalling ionized gas is a key constituent of fresh fuel for star formation, we should see the effects of this in galaxies external to our own. Understanding the behavior of ionized gas is therefore critical to understanding the evolution of disk galaxies.

1.4. Motivation for this Work

Our survey aims to characterize the behavior and extent of EP ionized gas to determine whether we can detect lagging gas in a sample of nearby, edge-on spiral galaxies. Previous studies of the kinematics of EP gas targeted galaxies with high SFRs and were looking for a lagging component. Our sample covers a range of SFRs (L_{FIR}/D_{25}^2 0.03 – 8.9) and includes active and passive galaxies, which will help us shed light on how common lagging EP gas is. Aside from detecting a lagging component, our survey will also study the extent to which EP gas is detected above the midplane. The presence of EP DIG being correlated with SFR per unit area has been established for a handful of galaxies, but several of those studies targeted galaxies with known high star formation rates. Our study will investigate whether this trend holds true for galaxies with low SFRs.

Additionally, studies that have measured vertical velocity gradients of EP gas have generally been done with single long-slit spectroscopy, integrated field units, or Fabry-Perots. We employ another technique to measure velocities of ionized gas: multi-long-slit spectroscopy. Multi-long-slit spectroscopy is similar to a combination of traditional single slit spectroscopy and imaging. It allows us to isolate any desired spectral line (given available narrowband filters), and we are able to measure that spectral line over a wide spatial area of our target in a single exposure. Since we only need a single line to measure gas velocities, the multi-long-slit setup is a much more time-efficient way to observe each of our targets than using single slit spectroscopy.

Our multi-long-slit set-up consists of a slit mask with 11 uniform, parallel slits that produces a spectrum that is a montage of 11 spectra side by side. We

use a narrowband filter centered near our target's redshifted Hα in series with the slit mask to prevent neighboring spectra from overlapping. By arranging the slits parallel to the minor axis, we are able to measure Hα velocities as a function of distance from the midplane in 11 radial distance bins simultaneously over a 3.75' field. This is effective for characterizing the kinematics of an extended object, such as a planetary nebula or galaxy's thick disk or halo. The narrowband filter can be chosen to isolate any desired spectral line, or a specific spectral line at a range of recessional velocities.

Our targets were selected from the 2MASS Large Galaxy Atlas (Jarrett et al. 2003) with the following requirements: K-band radii (R_{K20}) greater than 2.2′, minor/major axis ratio less than 0.3, and v_{hel} less than 1600 km s^{-1}. They also had to be observable from northern hemisphere and be very close to edge-on. UGC 7321 was added to the sample even though its R_{K20} is only 1.0′ because it is a low surface brightness galaxy but has an extended HI layer. Our target galaxies and their basic properties are listed in Table 1.1. When not cited elsewhere in the dissertation, galaxy parameters in that table are from the HALOGAS Survey (Heald et al. 2011), NED, or the Extragalactic Distance Database (Tully et al. 2009). We use L_{FIR}/D_{25}^2 as a proxy for star formation rate, and our values are adapted from R. Walterbos.

The requirement that our targets have inclinations close to 90° allows us to distinguish between disk gas and extra-planar gas. This also complicates the analysis of the emission profiles we observe. Our aim is to measure the rotational velocity of the ionized gas at a specific point in the galaxy, but each line-of-sight (LOS) through an edge-on system produces a line profile that is a superposition of all the velocities observed along that LOS through the disk (eg. Kregel &

van der Kruit 2004). Assuming circular rotation througout a disk and a smooth distribution of emitting gas, the maximum observed velocity occurs at a point along the observer's LOS where the LOS passes closest to the galaxy's center. At this point, the LOS is tangent to gas moving in a circular orbit at that radius, and the entirety of the gas's velocity is along the LOS. In front of and behind that point, only part of the gas's rotational velocity is along the LOS, so the observed velocity is less than the actual rotational velocity. This results in an asymmetric, non-Gaussian emission profile with a low-velocity tail. This tail is relatively faint and not fully resolved in our data. Therefore we do fit a Gaussian profile to each of our observed emission profiles and use the centroid to measure the wavelength and velocity of the Hα-emitting gas. Centroid fitting has been used previously to measure lagging components in edge-on galaxies (e.g. Rand (1997, 2000b); Tüllmann et al. (2000); Miller & Veilleux (2003)). It is a legitimate method to measure gas kinematics, but it is less accurate for an edge-on system because the observed line profiles have low-velocity tails and are not Gaussian in nature. Depending on the resolution of the data and the profile-fitting routine, this can introduce a bias to the measured velocities.

To account for this, we model each of our targets specifically for the field of view of our multislit setup. We introduce various vertical velocity gradients to the models, fit Gaussian profiles to the model emission profiles, and compare the subsequent model centroid velocities to the centroid velocities we measure from our data. We test a range of velocity gradients to see which one, if any, produces a velocity profile that best fits the data.

We apply our observing and modeling technique to a sample of 13 edge-on targets and two additional non-edge-on targets, which act as test galaxies to show

that our multi-long-slit setup is a viable one for measuring ionized gas velocities. By characterizing the kinematics of the EP gas for our sample of galaxies, we will be able to provide constraints for models of the origin of EP gas. Several of our targets are a subset of the HALOGAS survey, which is investigating cold gas accretion in spiral galaxies in the local universe with deep WSRT observations, and our data provide an optical complement to theirs.

In Chapter 2 we describe our multi-long-slit observing setup, and we present 2D velocity fields for two inclined galaxies, NGC 4559 and NGC 5055. We show a comparison between our Hα velocities and HI velocities to demonstrate the validity of our observing technique. We discuss our multi-long-slit modeling for edge-on galaxies in Chapter 3 and present our observations and modeling for two edge-on galaxies, NGC 891 and NGC 4631. Chapter 4 consists of our observations and modeling for three highly inclined galaxies, NGC 4517, NGC 4565, and NGC 5907. Chapter 5 contains our mulit-long-slit data and velocity fields for galaxies for which we did not detect extended DIG, did not detect a lagging component, or were unable to model due to irregular kinematics in the galaxy's disk. We include a summary of our study and concluding remarks in Chapter 6.

Table 1.1. Multi-slit Sample: Galaxy Parameters

Galaxy	Type	Distance (Mpc)	v_{sys} km s^{-1}	i (°)	v_{rot} km s^{-1}	D_{25} (arcmin)	M_B (mag)	L_{FIR}/D_{25}^2 10^{40} erg s^{-1} kpc^{-2}
NGC 891	Sb	9.5	528	90	212.1	12.2	-19.96	2.2
NGC 3044	Sc	21.7	1335	85	153.1	4.4	-19.74	3.3
NGC 3079	Sm	15.0	1125	88	208.4	7.7	-21.01	8.9
NGC 3628	Sb	7.7	843	87	211.7	14.8	-19.96	2.0
NGC 4013	Sbc	17.1	831	84	181.7	4.7	-19.55	2.7
NGC 4517	Scd	11.1	1131	87.4	139.8	9.5	-19.58	0.5
NGC 4565	Sb	10.8	1230	87.5	244.9	16.2	-20.34	0.5
NGC 4631	Sd	7.6	606	85	138.4	14.7	-20.12	1.8
NGC 4762	SO	16.8	942	87	110.0	8.3	-20.04	>0.2
NGC 5229	Sc	5.1	365	90	55.8	3.5	-15.82	>0.1
NGC 5907	Sc	11.0	666	87	226.7	12.6	-20.55	0.8
UGC 4278	Sd	13.6	565	90	78.9	4.3	-17.45	0.2
UGC 7321	Scd	10.0	403	90	94.5	5.1	-14.79	0.03
NGC 4559	Scd	7.9	816	69	102.8	11.3	-20.07	-
NGC 5055	Sbc	8.5	497	55	178.5	13.0	-20.14	-

Note. — See text, section 1.4, for references.

2. MULTI-LONG-SLIT OBSERVATIONS OF NGC 4559 AND NGC 5055

2.1. Multi-long-slit Spectroscopy

The technique of multi-long-slit spectroscopy, which uses a mask with a series of parallel slits instead of a single slit, was first used by Wilson (1958) to study the kinematics of planetary nebulae. He measured how expansion velocities in the inner parts of PNe compare to expansion velocities in the outer parts using a single spectral line, λ3869 [NeIII]. Wilson et al. (1959) used multi-long-slit spectroscopy to measure radial velocities of the Orion Nebula from three spectral lines (λ5007 [OIII], λ4341 [Hγ], and λ3726,3728 [OII doublet]). These two studies were among the first to use a multi-long-slit spectroscopic setup to observe extended objects. In cases of kinematic studies, where velocities from a single spectral line are sufficient to characterize motions of the gas, multi-long-slit spectroscopy offers a more time efficient method of observing than traditional single-slit observing. From a single exposure, velocities can be measured at several locations in an extended source. Using single-slit spectroscopy would require multiple exposures to achieve the same purpose. A slit mask with n slits can therefore reduce the observing time by a factor of n while still providing the same spatial coverage and depth of observations.

More recent studies using multi-slit observing consist of blind searches for Lyα emitters (eg. Crampton & Lilly 1999; Stockton 1999; Martin & Sawicki 2004; Tran et al. 2004). To search for faint, Lyα-emitting galaxies at high redshift ($z \sim$5 or greater), large sky coverage and deep observations to obtain sufficient signal-to-noise levels are ideal. The multi-slit approach can provide large coverage if the slit mask is designed with many slits in parallel. Using spectroscopy instead of

narrowband imaging to detect the Lyα line disperses the background light, which decreases sky levels and noise beneath the observed emission line and makes the Lyα line easier to detect for a given length exposure. Multi-slit observing with a narrowband filter therefore decreases the exposure time necessary to achieve the same signal-to-noise level as with narrowband imaging.

This study uses multi-long-slit spectroscopy to measure the extent and kinematics of Hα-emitting extra-planar (EP) gas for a small sample of nearby, edge-on galaxies. The goal of our study is to help determine how common it is for the ionized EP gas to lag the disk in rotation. The multi-long-slit setup is ideal for our observations because it allows us to measure gas velocities at several galactocentric radii simultaneously. In addition to having more spatial locations from which we can measure a potential lagging component, we can also look for radial variations in the value of the vertical velocity gradient.

2.2. Multi-long-slit Mask Design

We designed our primary slit mask to be used on the Double Imaging Spectrograph (DIS) on the 3.5m ARC telescope at Apache Point Observatory (APO) in New Mexico with the highest resolution grating, which is the R1200 grating (1200 lines mm^{-1}). The mask is used in series with a filter with a full-width at half-maximum (FWHM) value of 25 Å. There are several considerations when designing a mask for use with a particular filter, spectrograph, and grating. Grating and slit width affect the spectral resolution of the data, with fewer lines per mm or wider slits resulting in lower spectral resolution for a given pixel scale of a CCD. A low resolution setup disperses light over a smaller angle on the CCD, so the light is

more concentrated on a smaller number of pixels. This results in higher sensivity for detection of faint emission, provided the line remains resolved. A setup with lower resolution also allows for slits to be placed closer together without significant overlap of neighboring spectra. This means more slits can be placed on the slit mask, so a lower dispersion setup provides greater sky coverage.

More coverage and higher sensitivity are ideal for observing faint, extended sources, but one must also take into account the expected line width of the spectral features that will be measured. If the observer wants to measure spectral features that are closely spaced or have narrow line widths, then a higher resolution setup must be used. Lyα line widths can be large ($\sim$250 km s^{-1} or more, e.g. Ajiki et al. 2002; Bunker et al. 2003), but the Hα linewidths we measure are much smaller, so a higher dispersion grating is necessary for our observations.

The filters we use with our slit mask also affect our mask design. A filter with a wide passband offers more versatility to observe galaxies at a larger range of recessional velocities. But wide filters also let in more background light, which means neighboring spectra will overlap. This can be a problem if the Hα line we wish to observe falls near the edge of the filter passband, so using a wide filter requires the slits to be spaced farther apart.

A narrowband filter is less versatile in terms of observing galaxies at different redshifts, but the spectra it produces are narrower in wavelength space. Slits on the slit mask can be placed closer together without neighboring spectra interferring with each other. This allows us to measure gas velocities at a larger number of galactocentric radii for each of our targets. The range in recessional velocities of our targets is small (350 km s^{-1} – 1300 km s^{-1}), so we need only a few narrowband

filters for our observations.

After testing various combinations of slit mask parameters, we designed our primary slit mask with 11 parallel 1.5″-wide slits, each of which is 4' long. The limiting factor for the length of the slits is the physical size of our filters. The spacing between the slits is 22.5″, and the slit mask is coupled with a 25 Å FWHM filter. This slit spacing maximizes the number of slits on the mask while minimizing the amount that neighboring spectra overlap.

The pixel scale of DIS is 0.4 arcsec pix^{-1}. Given our slit spacing of 22.5″, the theoretical spacing between slits as they appear on the CCD detector is 56.3 pixels. At a dispersion of 0.58 Å pix^{-1}, which is the average dispersion of the R1200 grating, this spacing corresponds to 32.6 Å. However, anamorphic demagnification of the spectrograph (Schweizer 1979) decreases the projected spacing of the slits on the CCD by ∼25% for this setup, resulting in an actual spacing between the slits of 42.4 pixels, or 24.6 Å. This is roughly equal to the FWHM of our filter, which means overlapping regions of neighboring spectra are at the edges of the filter passband where transmission is low and we are not making velocity measurements. To ensure that we avoid these regions, we restrict our observations to fields with observed Hα at wavelengths that are no more than half of the FWHM value from the center of the passband.

We have 25 Å FWHM filters with central wavelengths of 6560 Å, 6570 Å, 6580 Å, and 6590 Å to accomodate targets with a range of recessional velocities. We also designed and manufactured other slit masks with varying numbers of slits and various slit widths to provide options for other users who might want to use the multi-long-slit spectroscopic setup at APO.

Using line widths from an Hα lamp, we determined that our multi-long-slit mask on DIS with the R1200 grating has a spectral resolution of 1.45Å. At the wavelength of Hα (6562.8Å), this results in a resolving power ($\lambda/\Delta\lambda$) of $\sim$4500 and a velocity resolution of $\sim$65 km s^{-1}. However, through profile fitting, we are able to measure velocities to an accuracy of $\sim$5-10 km s^{-1}.

2.3. Multi-long-slit Test Galaxies

Our sample for this project consists of edge-on galaxies, but we use two nearby, non-edge-on galaxies for which we have HI data, NGC 4559 and NGC 5055, to demonstrate our multi-long-slit setup for measuring rotational velocities of galaxies. Our methods for data reduction and velocity measurements for these two galaxies are the same as for the rest of our sample and are described in §2.5.

NGC 4559 is an Scd spiral with an inclination of 67° and a distance of 9.7 Mpc (Tully 1994). It does not appear to be interacting with any neighboring companions. It has a fairly high star formation rate of 1.3 $M_\odot$ yr $^{-1}$ (Kennicutt et al. 2003) and has been found to have a thick, HI disk that lags its thin disk in rotation (Barbieri et al. 2005). NGC 5055 is an Sbc spiral (de Vaucouleurs et al. 1976) with an inclination of 64° (Battaglia et al. 2006) and a distance of 7.2 Mpc (Pierce 1994). It is a warped galaxy and shows signs of interactions. However, it is a fairly symmetrical galaxy (Battaglia et al. 2006). Both galaxies are part of the Hydrogen Accretion in Local Galaxies (HALOGAS) Sample, which is a Westerbork Synthesis Radio Telescope (WSRT) deep HI survey studying cold gas accretion in the local universe (Heald et al. 2011). We compare our Hα velocities to HI velocities from HALOGAS data to show that our multi-long-slit

setup produces accurate velocities.

2.4. Observations

We observed NGC 4559 and NGC 5055 with DIS and the R1200 grating on the ARC 3.5m telescope at Apache Point Observatory near Sunspot, NM. We used our 11-slit mask, which consists of 11 1.5″ wide and 4′ long slits. The DIS grating has a dispersion of 0.58 Å pix^{-1}, and our velocity resolution for the setup was ∼65 km s^{-1}. The observing parameters for each galaxy are shown in Table 2.1. We observed NGC 4559 on 30 March, 2011. We observed the east and west fields of NGC 5055 on 28 and 29 April, 2011, respectively. Slit positions for the two galaxies are shown in Figures 2.1 and 2.2. In each figure, the slits are overlaid on an Hα KPNO image (Patterson & Walterbos 2013; Patterson 2013).

We used a 6570 Å filter with a FWHM of 25 Å in series with our slit mask to observe the approaching and receding sides of NGC 5055. Emission from these fields falls within the acceptable range for that filter of 6570 Å ±12.5 Å. For NGC 4559, we used a filter centered at 6580 Å, and we observed the receding side of the galaxy. We aligned the slits perpendicular to the major axis of each galaxy for

Table 2.1. Observing Parameters: NGC 4559 and NGC 5055

Field	RA [a] (J2000)	Dec [a] (J2000)	Field Offset [b] (″)	PA (°)	Total Integration Time (hrs)	V_{sys} (km s^{-1})	Observed Hα[c] (Å)
NGC 4559	$12^h35^m57.60^s$	+27°57′31.4″	90	150	1.0	810	6580.5
NGC 5055 East	$2^h22^m33.41^s$	+42°20′56.9″	−105	105	0.75	498	6573.7
NGC 5055 West	$2^h22^m33.41^s$	+42°20′56.9″	142.5	105	1.0	498	6573.7

[a]Coordinates of the galaxy center.
[b]Distance from galaxy center to the central slit. Negative values indicate the central slit is east of the galaxy center.
[c]Observed Hα at the systemic velocity of that galaxy.

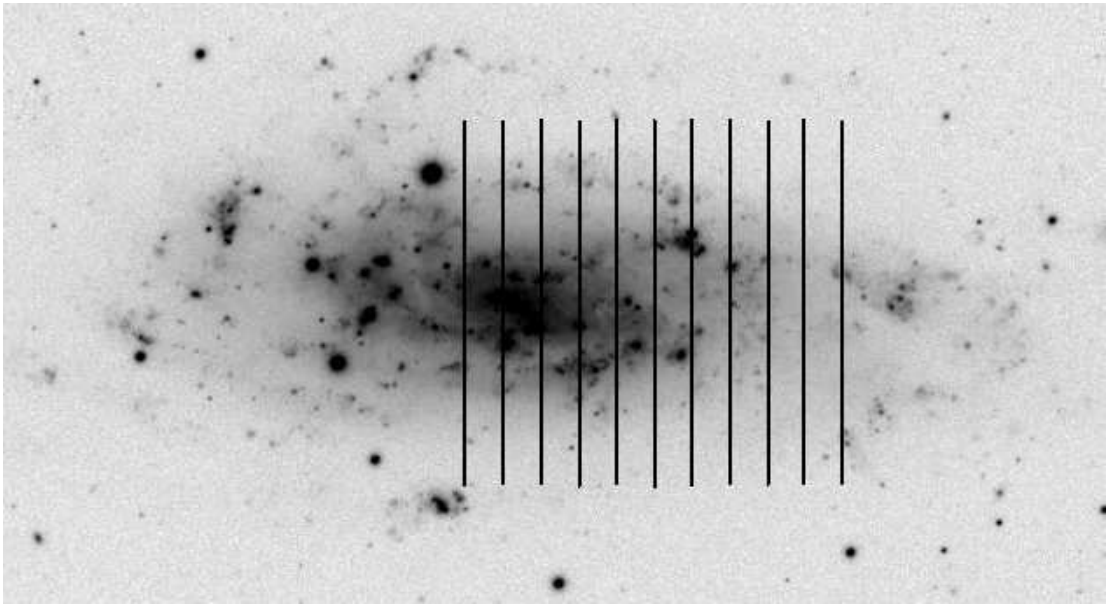

Fig. 2.1.— Slit positions of the 11 slits for NGC 4559 are shown on an Hα image (Patterson 2013). North is up, and east is to the left. The center of the galaxy is between the 1st and 2nd eastern-most slits. The west (right) side of the galaxy is receding. The slits are 4$'$ long, which corresponds to 9.2 kpc at a distance of 7.9 Mpc.

both targets, and the observations for each field in consisted of a single exposure.

Our slit mask setup is mounted in a filterwheel on DIS that also includes the standard 1.5$''$ slit. The single slit is coupled to a slitviewer, which allows the observer to see where the telescope is pointed. At the beginning of each night, we measure the spatial offset between the center of the single slit and the center of the central slit on the multi-long-slit mask. With the single slit in place, we use the slitviewer to center on our desired field. We then apply our measured spatial offsets, which centers our target in the central slit on the multi-long-slit mask, and rotate the filterwheel so our multi-long-slit mask is in place for observing.

During each night of observing, we took at least two blank sky frames for subtracting sky lines from our data. Sky frames were taken at similar heights

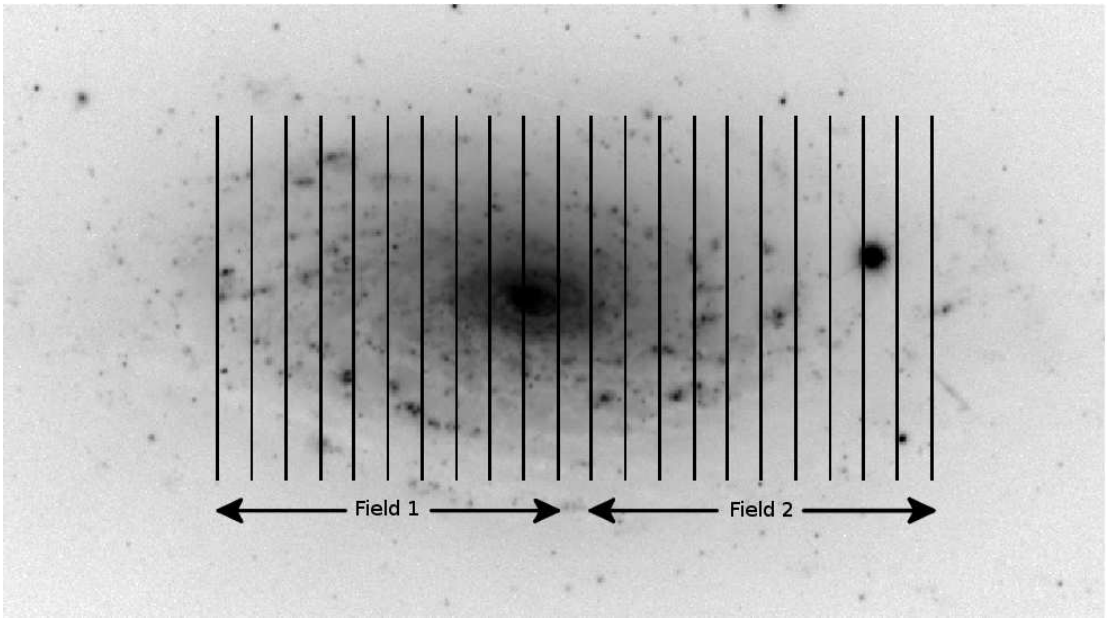

Fig. 2.2.— Slit positions for two fields for NGC 5055 are shown on an Hα image (Patterson 2013). North is up, and east is to the left. The western-most slit in Field 1 is 7.5″ west of the galaxy center. Most of Field 1 covers the receding side of the galaxy, and Field 2 is on the approaching side. The slits are 4′ long, which corresponds to 9.9 kpc at a distance of 8.5 Mpc.

above the horizon as our target frames so we observed through similar airmass. APO has the option of using a hydrogen lamp in addition to the standard HeNeAr lamps mounted in the telescope dome to take wavelength calibration frames. We used this lamp to take calibration frames with the telescope pointed in a similar position as the target frames to take into account any effects that flexure might have on the optics. All of our spectra and calibration frames were binned by 3 pixels in the spatial direction to increase the signal-to-noise ratio of our data.

2.5. Data Reduction

We use IRAF[1] to perform basic reduction and calibration steps on our data. Multi-long-slit data for NGC 5055 during various stages of data reduction and calibration are show in Figures 2.3 – 2.5. After subtracting the mean bias level, we flat field each frame with a normalized bright quartz lamp flat frame to remove pixel-to-pixel sensitivity variations of the CCD. We manually remove cosmic rays from our target spectra with the task IMEDIT. The majority of cosmic rays do not overlap with the Hα emission, which simplifies this step. To remove cosmic rays from blank sky frames, we first scale them so they have similar sky line and continuum level. We then average them together with the task IMCOMBINE, which has an automatic cosmic ray removal algorithm called CRREJECT. This rejection operation ignores positive pixels above a certain noise threshold that are present in one frame but not in the others.

After cosmic ray removal, we wavelength calibrate the target frame and our combined sky frame. This step also straightens the spectral lines, which are curved in the raw frames due to spectrograph optics. To apply the standard IRAF tasks for calibrating single-slit spectra to our multi-long-slit spectrum, we treat our data as one continuous spectrum instead of a series of repeated spectra. With an H-arc lamp and 6570 Å filter, which we used for NGC 5055, each slit on the mask produces one Hα line. This results in 11 lines on the calibration frame (see Figure 2.6), each of which is at 6562.8 Å. For galaxies observed with the 6580 Å filter, such as NGC 4559, we used the 6598.95 Å line from a standard Ne lamp as

[1]IRAF (Image Reduction and Analysis Facility) is distributed by the National Optical Astronomy Observatories, which are operated by the Association of Universities for Research in Astronomy, Inc., under cooperative agreement with the National Science Foundation.

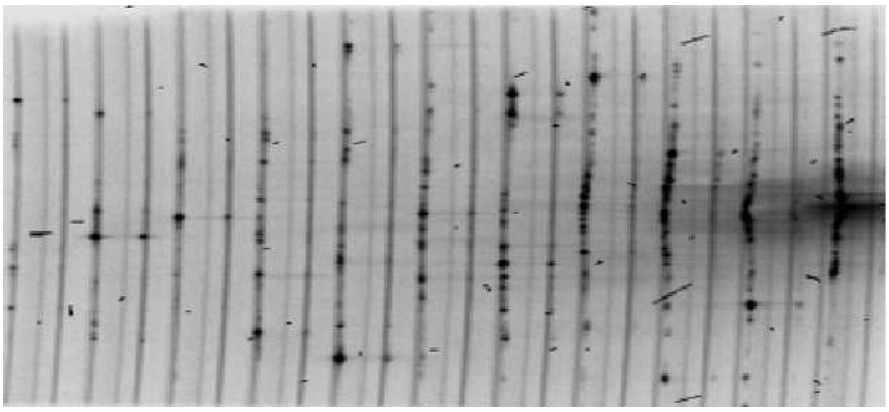

Fig. 2.3.— Raw spectrum for NGC 5055. The major axis of the galaxy runs horizontally through the middle of the spectrum. The vertical lines are sky lines, and the dark patches are Hα emission. The wavelength direction is along the x-axis, and wavelength increases to the left. The y-axis is the spatial direction. The vertical extent of the spectrum is 10.6 kpc, assuming a distance of 8.5 Mpc.

a calibration line. We can also use the Ne line for galaxies observed with the 6590 Å filter.

Regardless of which arc lamp we use, we assign artificial wavelengths to each arc line based on the pixel separation and spectrograph dispersion. To measure the dispersion of the spectrograph, we use a raw sky frame from that night. According to APO's instrument manual[2], the dispersion of DIS with the R1200 grating is 0.58 Å pix^{-1}. This can change slightly from night to night depending on instrument temperature or observing conditions, so when possible, we measure the dispersion empirically from sky lines.

Sky frames with the 6570 Å filter, which we used for NGC 5055, contain three sky lines per slit: atmospheric Hα at 6562.82 Å (which we refer to as line 1), an OH line at 6568.779 Å (line 2), and an OH doublet at 6577.183 Åand

[2]http://www.apo.nmsu.edu/arc35m/Instruments/DIS/

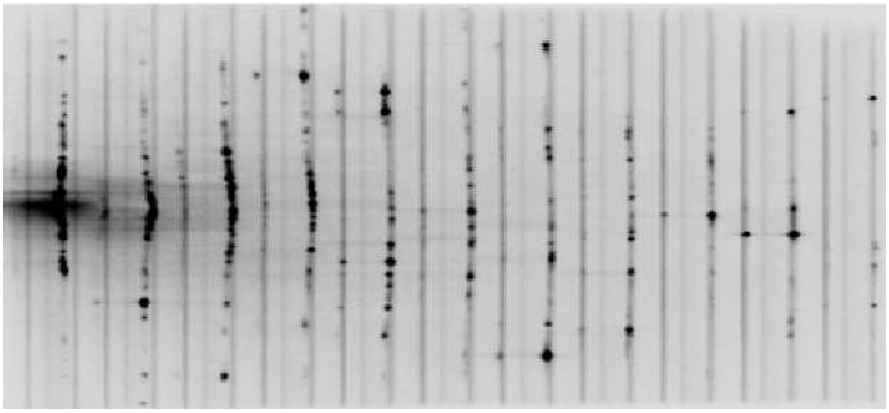

Fig. 2.4.— Wavelength calibrated spectrum for NGC 5055. This frame has also been bias subtracted and flat fielded. Spatially, north is down, and east is to the right. Wavelength is along the x-axis and increases to the right. The center of the galaxy is near the left-most slit, and the spatial extent of the spectrum is the same as in Figure 2.3.

6577.386 Å (Osterbrock 1996). With DIS's resolution, this doublet appears as one line. We assume a single wavelength of 6577.285 Å (line 3) for the doublet, which is the average wavelength of the two peaks. Figure 2.7 shows a combined sky frame with cosmic rays removed for the 6570 Å filter. We measure the pixel separation between each pair of sky lines in each slit at different heights along the slit. Together with the wavelength difference of each pair of sky lines, we calculate the dispersion of each slit at various heights. There are small variations in the measured dispersion from slit to slit, along each slit, and across the passband in each slit, so we take the average of all of our measurements to determine the dispersion for the entire field for that night.

Our dispersion measurements for the east field of NGC 5055 are shown in Figure 2.8. We measured the dispersion at 4 locations along each slit to see how the dispersion changed across the entire field. There is no general pattern to the variation in measured dispersion, but most measurements fall between 0.555 Å

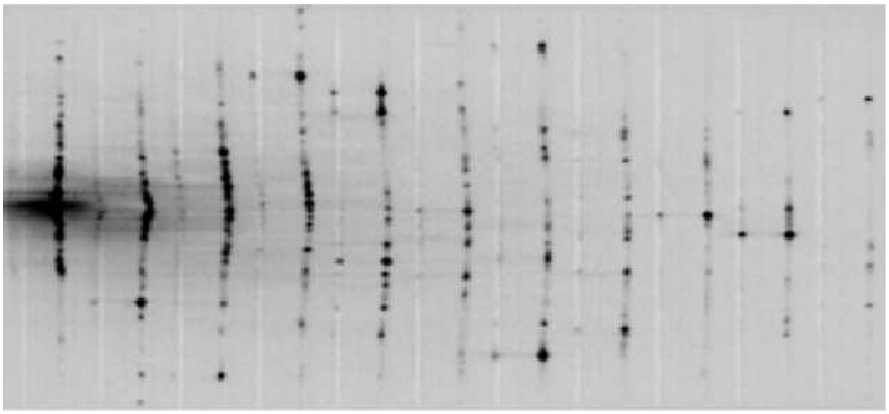

Fig. 2.5.— Sky line subtracted spectrum for NGC 5055. The white, vertical lines are over-subtracted sky lines, and the orientation and extent of the spectrum is the same as in Figure 2.4.

pix^{-1} and 0.585 Å pix^{-1}. The average dispersion is 0.5705 Å pix^{-1}. The observed emission in NGC 5055 shows a wide range of velocities along a single slit, which means the pixel location of the observed Hα can vary by as much as 5 pixels. A 5 pixel difference and an error of 0.016 Å pix^{-1}in dispersion, which is the maximum error for most points in this field, would result in a velocity error of 3.7 km s^{-1} for Hα measurements within a single slit. This value is within the error bars of our individual measurements, so we feel justified using a single, average value for the dispersion for all 11 slits. However, we do include this error as an instrumental error in our velocity calculations.

For NGC 4559, we used the 6580 Å filter, which only produces one sky line per slit. Since we could not measure the dispersion empirically, we initially used the published value for the dispersion of DIS. This resulted in an inconsistency between the Hα and HI velocities (see §3.3.1) that became larger and larger from slit to slit. One on side of the field, the velocities were in close agreement. For slits on the other side of the field, our Hα velocities were off by as much as 20 km

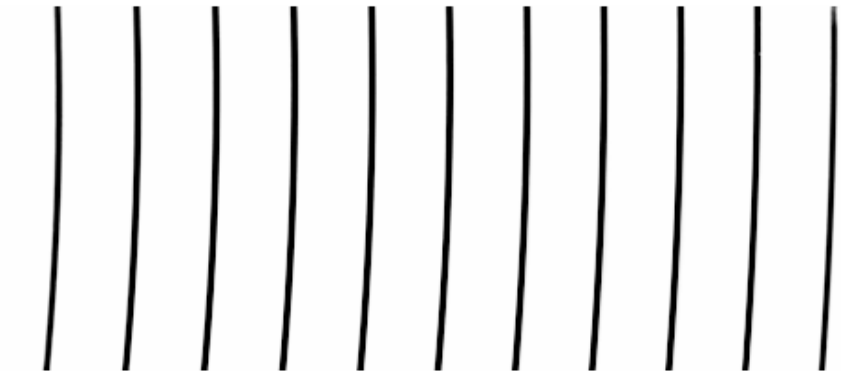

Fig. 2.6.— A Hydrogen arc lamp with the 6570 Å filter. Each slit produces one calibration line at 6562.8 Å. The curvature in the lines is due to the optics of the spectrograph and is removed during the wavelength calibration steps.

s^{-1} compared to the HI data. This increasing offset between the two data sets implied that there was an error in the dispersion. We re-calibrated our data using a dispersion of 0.570 Å pix^{-1}, which is the average of our measured dispersions from the two observing runs with the 6570 Å filter closest in time to the NGC 4559 observations (December 2010 and April 2011). This fixed the problem of increasing inconsistency between the HI and Hα data, so we took 0.570 Å pix^{-1} to be an accurate value for the dispersion for the NGC 4559 data. We assumed the same dispersion error of 0.016 Å pix^{-1} as the NGC 5055 data, and for NGC 4559, the observed Hα varies by only 3 pixels within a given slit. This produces a velocity error of 2.2 km s^{-1} from instrumental error.

With our measured dispersion from the sky frame, we can use the pixel difference between the centers of the Hα lines in the arc frame to calculate artificial wavelengths for each arc line. We assign 6562.82 Å to the central Hα line in the arc frame. Based on pixel differences blueward or redward of the central line, we determine wavelengths for the other 10 arc lines. This creates an artificial contin-

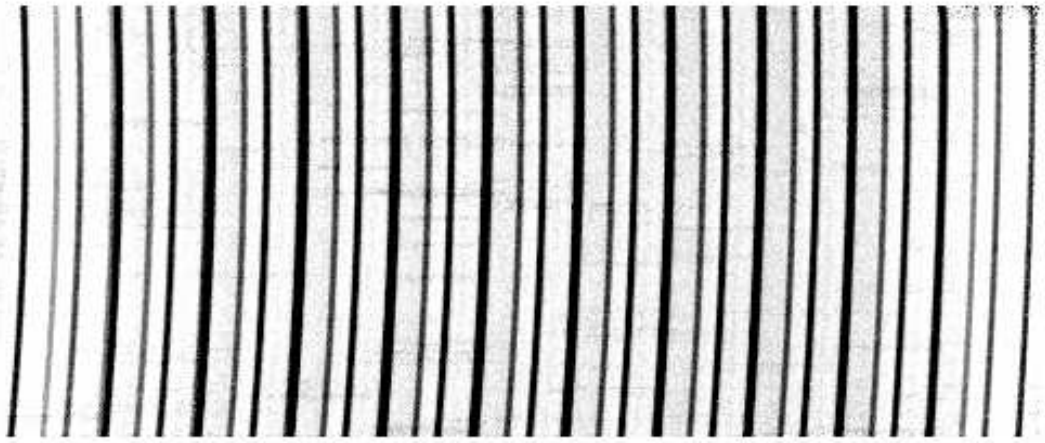

Fig. 2.7.— A blank sky frame with the 6570 Å filter consists of three atmospheric sky lines per slit. The boundary of each slit can be inferred from the sky lines. Starting on the left, each slit contains one bright line (6577.285 Å doublet) and two fainter lines (6568.779 Å and 6562.82 Å). The last line on the right-hand side of the frame appears as a faint sky line, but it is actually a reflection of the bright sky line and is not a sky line itself.

uous spectrum that serves as our wavelength calibration frame for all 11 slits. We use the IRAF tasks IDENTIFY and REIDENTIFY to assign an artificial wavelength to each arc line in our calibration frame. Then we use the FITCOORDS task to determine the wavelength solution of the calibration frame as a function of xy coordinates. We then use TRANSFORM to apply the wavelength solution to the target and sky frames.

After our target and sky frames are calibrated, we smooth the sky frame by three pixels in the spatial direction (along each slit) to reduce noise in the sky lines and in the background continuum. We scale the sky frame so the intensity of the sky line closest to the observed Hα of our target matches the intensity of that same sky line in the galaxy spectrum. We subtract the smoothed, scaled sky frame from our galaxy spectrum to remove sky lines, producing a final spectrum

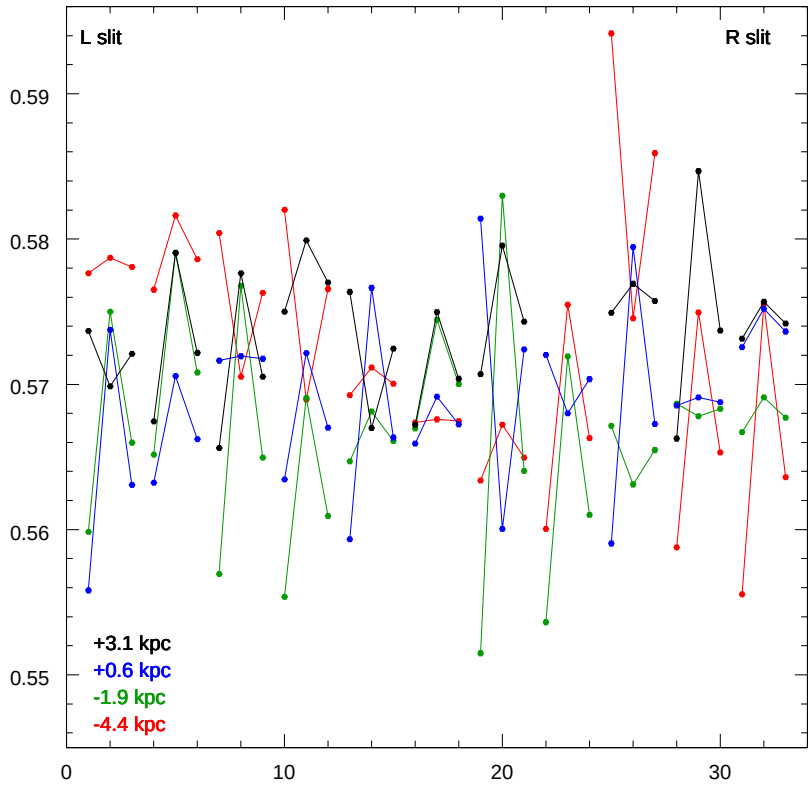

Fig. 2.8.— The measured dispersion for the NGC 5055 east field is shown at four locations for each of the 11 slits. We measured the dispersion at lines 20, 70, 120, and 170 (red, green, blue, and black, respectively). For reference, the major axis of the galaxy lies at line 108. Each set of three points are dispersion measurements from one slit.

for a given field for that night. Changes in sky conditions, such as weather, clouds, and moonlight, throughout the night can affect the relative intensities of the sky lines, which results in over- or under-subtraction of some sky lines. We choose our scaling so this does not occur close to the Hα emission, so it does not affect our measurements of the Hα velocities. If we need to further remove sky line remnants, we use the IRAF task BACKGROUND or IMEDIT. BACKGROUND fits a function along each column according to user-specified sections of the frame

that are free of Hα emission. This function is representative of the background level for that column and is subtracted from the spectrum. IMEDIT is a task for general editing of fits images. We choose regions of pixels that encompass the sky line remnants we want to subtract, and IMEDIT deletes those pixels and fills them in with the average value from neighboring pixels.

Two different forms of sky line subtraction for NGC 5055 west, a field for which we did not do our standard sky subtraction, are shown in Figures 2.9 – 2.11. The three panels show this field before sky line subraction, after standard sky line subtraction, and after using the BACKGROUND task only. Even after wavelength calibrating the sky and target frame, the sky lines did not match up in both frames. This is likely due to the sky frames not being taken close in time to the target frame. The arc frame used to calibrate this field was taken close in time to the target frame, so our wavelength solution and measured velocities should not be affected. We found that only using the BACKGROUND task to subtract sky from this field had favorable results, so that is how we produced our final spectrum for this field.

Our final spectra for NGC 4559 and the east field of NGC 5055 are shown in Figures 2.13 and 2.12. For these fields, we did our standard procedure for sky line subtraction.

2.5.1. Velocity Measurements

Once we have our final spectrum for a given field, we measure the wavelength of the emission at a range of positions along each slit. Since our slits are oriented parallel to the minor axis, each position along a given slit corresponds to a per-

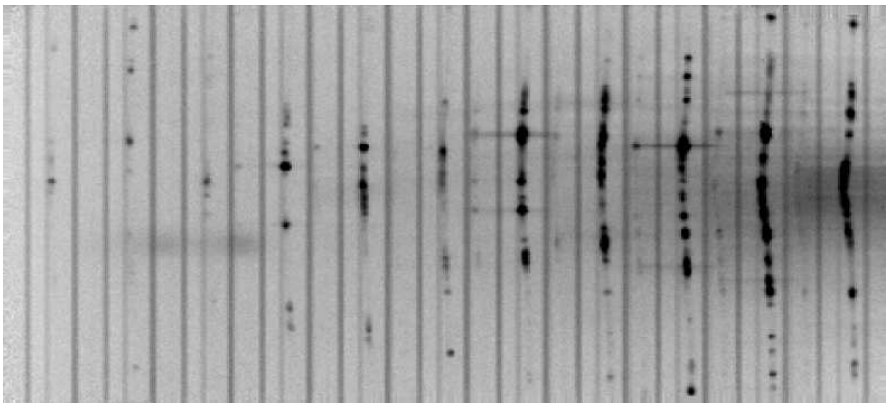

Fig. 2.9.— Spectrum for NGC 5055 west before sky line subtraction. North is down and east is to the right. The vertical extent is 9.0 kpc, assuming a distance of 7.2 Mpc.

pendicular distance from the major axis. Using Figure 2.12 as an example, in which north is down and east is to the right, we refer to the positions in each slit which are north of (below) the major axis as having a negative distance from the major axis. Positions which are above the major axis are designated as having a positive distance from the major axis.

Using the IRAF task SPLOT, we extract emission profiles for each slit at the fullest range of positions where there is measureable emission. Where there is ample emission, such as close to the major axis, we sum three rows and measure the resultant emission profile. At greater distances from the major axis, or in places where the emission is fainter, we sum up to eight rows. We fit a Gaussian function to each Hα emission profile and take the centroid to be the wavelength of the observed Hα emission. We apply the same process to a bright sky line in each slit in our blank sky frame so that we have an observed sky line wavelength at the same distance from the major axis and with the same number of rows summed as each Hα measurement. Using the difference between the wavelengths of the sky

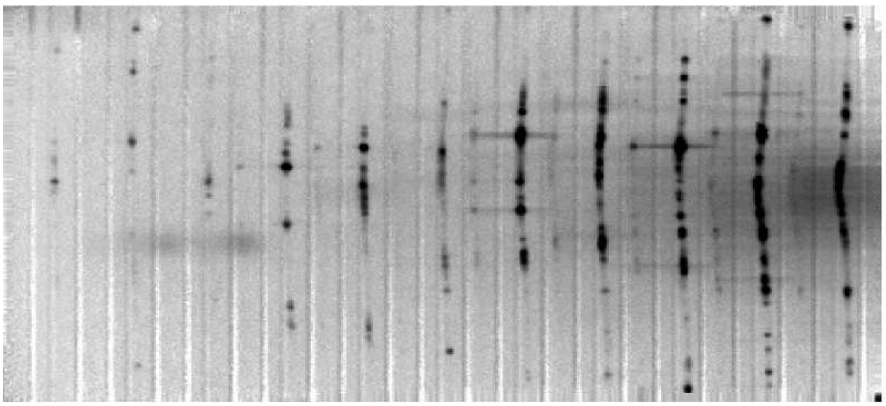

Fig. 2.10.— Standard sky line subtraction for NGC 5055 west. We obtained this frame by subtracting a blank sky frame, but the curvature of the sky lines differs between the sky and target frames. This results in an acceptable sky line subtraction for the top of the frame but not the bottom. The orientation and spatial extent of this spectrum is the same as in Figure 2.9.

line and the Hα emission, we calculate the velocity of the observed Hα emission:

$$v = \frac{\lambda_{sky} + (\lambda_{H\alpha,obs} - \lambda_{sky,obs}) - 6562.82 \text{ Å}}{6562.82 \text{ Å}} \times c \tag{2.1}$$

where $\lambda_{H\alpha,obs}$ is the observed wavelength (in artificial units) of the Hα emission, $\lambda_{sky,obs}$ is the observed wavelength (in artificial units) of the sky line, 6577.28 Å is the actual wavelength of the sky line doublet, 6562.8 Å is rest-frame Hα, and c is the speed of light. Based on the date and time of the observations, we use the IRAF task RVCORRECT to determine a velocity offset to correct for the Earth's motion, which gives us heliocentric velocities for our data.

SPLOT calculates an error for each Gaussian centroid based on the noise level in the data on either side of the profile. Lower signal-to-noise ratios at greater distances from the major axis result in greater errors. These centroid errors from both the Hα emission fit and the sky line fit are added in quadrature to the instrumental error from the dispersion measurement mentioned above to obtain the total error for each velocity measurement.

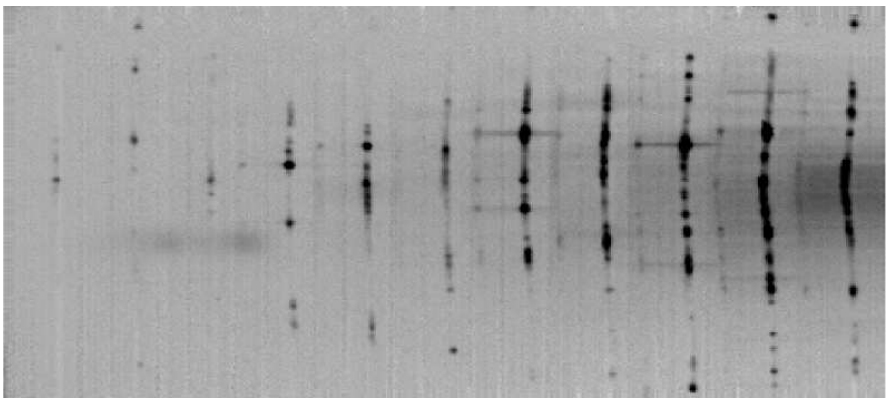

Fig. 2.11.— Alternate sky line subtraction for NGC 5055 west. This spectrum is the result of using only the BACKGROUND task to remove sky lines. This resulted in better sky line subtraction than the standard subtraction method. The orientation and spatial extent of this spectrum is the same as in Figure 2.9.

2.6. Results

To test the accuracy of our multi-long-slit setup to measure velocities, we compare our Hα data to HI velocity fields from HALOGAS data. The HALOGAS observations consist of 10 x 12 hr exposures with the WSRT. HI data for NGC 4559 and NGC 5055 both have a velocity resolution of $\sim$4 km s^{-1}. The NGC 4559 observations have a beamsize of $41.56'' \times 32.11''$, and the NGC 5055 observations have a beamsize of $35.63''\times$ $33.03''$. Our data have a velocity resolution of $\sim$65 km s^{-1}, but with centroid fitting, we can measure velocities to within $\sim$5 km s^{-1}, depending on the signal-to-noise ratio. Our spatial resolution is $1.2''$. The large beam size of the HI data effectively smooths out the HI velocities, so we are unable to see changes in velocity on small scales, but the overall pattern of the velocity profile should be similar to that of the Hα data. Additionally, our slit spacing ($22.5''$) is smaller than the HI beam size, so a single HI velocity profile incorporates velocities from two or three of our slit locations.

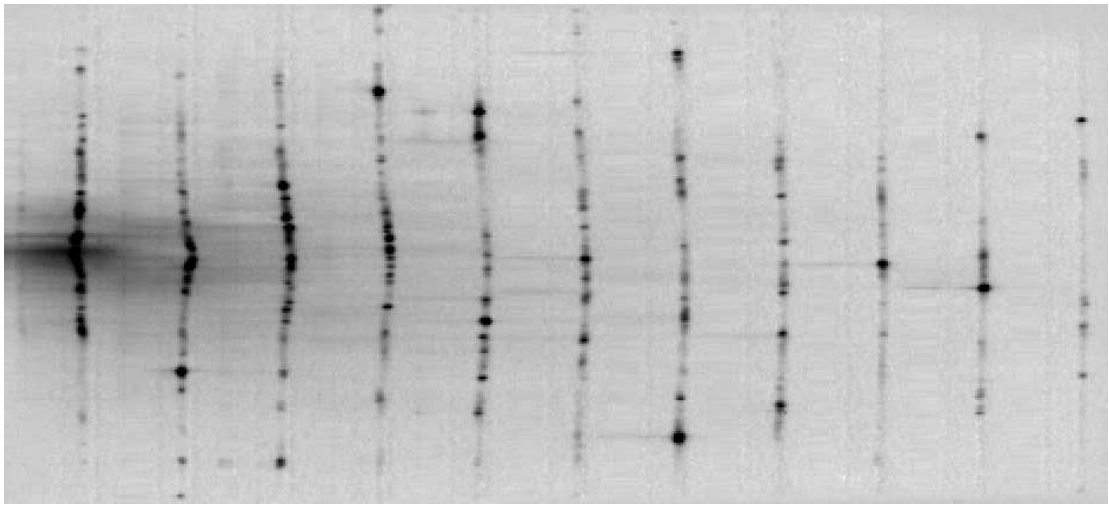

Fig. 2.12.— Final spectrum for NGC 5055 east. North is down and east is to the right. The center of the galaxy is between the right-most two slits. The vertical extent of the spectrum is 9.0 kpc, assuming a distance of 7.2 Mpc.

To obtain HI velocities at our slit locations, we used the Groningen Image Processing System (GIPSY; van der Hulst et al. 1992) task MOMENTS to create an intensity weighted mean velocity (moment-1) map from an HI data cube from the HALOGAS survey (Heald et al. 2011). We took cuts along the moment-1 map at the same locations as our slits to obtain HI velocity profiles as a function of perpendicular distance from the major axis. Because these galaxies are inclined, we expect their velocity profiles to show a curved, 'C'-shaped pattern on the approaching side of the galaxy and the opposite pattern on the receding side. Figure 2.14 shows the geometry of viewing a non-edge-on disk. The middle of the slit in the spatial direction crosses the major axis of the galaxy. At that point, the maximum rotational velocity is observed. At points above or below that along the slit, a smaller and smaller component of the rotational velocity is observed. Assuming a flat rotation curve, the observed velocity on the receding side of a galaxy will decrease with perpendicular distance from the major axis. On the

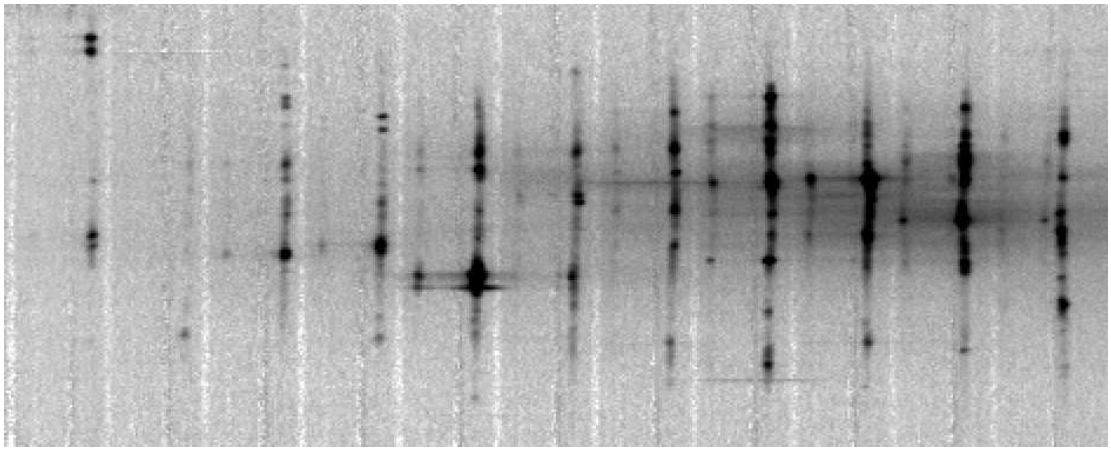

Fig. 2.13.— Final spectrum for NGC 4559. An over-subtracted sky line can be seen as a fuzzy, white vertical stripe in each slit. The second slit from the right is on the center of the galaxy. The vertical extent of the spectrum is 10.8 kpc, assuming a distance of 9.7 Mpc. Spatially, north is down and east is to the right.

approaching side, the opposite occurs.

Velocity profiles from Hα centroids overlaid on velocities from HI moment-1 maps for NGC 4559 and the east and west fields of NGC 5055 are shown in Figures 2.15 – 2.17. Slits 1 – 9 in Figure 2.15 are on the receding half of NGC 4559, and slits 10 and 11 are on the approaching side. At a distance of 9.7 Mpc, 1.2″ corresponds to a spatial size of 0.06 kpc, whereas the HI beam has dimensions of 1.95 kpc × 1.51 kpc. In general, the spatial extent of measurable Hα emission decreases as the slit distance from the center increases. Slit 1 overlaps a prominent spiral arm (see Figure 2.1, right-most slit), so emission is seen near the middle and top of the slit, but it is not seen along the slit between those detections. Slits 9 and 10, which straddle the center of the galaxy, show a bump in the Hα velocities near the major axis. This is likely due to radial motions of gas flowing inward or outward along a bar or streaming motions if the gas is entering a spiral arm. Both of these mechanisms can increase the speed at which the gas rotates.

Figure 2.16 shows the receding (east) side of NGC 5055 for slits 2 through 11, and the velocity profiles show a backward 'C'-shaped pattern. Slit 1 is on the approaching side of NGC 5055 and shows the opposite pattern. All of the slits in Figure 2.17 are on the approaching (west) side of NGC 5055. The Hα velocities for both fields are in close agreement with the HI velocities. Similar to NGC 4559, any small-scale discrepencies between the HI and Hα data are likely due to the difference in spatial resolution between the data sets. The 1.2″ resoution of the Hα data corresponds to 0.04 kpc at a distance of 7.2 Mpc, and the HI beamsize has a physical size of 1.24 kpc $\times$ 1.15 kpc.

2.7. Summary and Conclusions

We designed a multi-long-slit spectroscopic observing setup that allows us to observe the Hα spectral line at several spatial locations over a large field in a single exposure. This is ideal for studying the kinematics of extended objects, such as inclined galaxies or edge-on galaxies with thick disks. We show that our Hα velocities are in close agreement with HI data. Our Hα data have a spatial resolution of 1.2″, while the HI data have a beam size of 30″+. We can see small scale velocity changes in our Hα data, but these are smoothed out by beam smearing in the HI data. Overall, the shape of the Hα and HI velocity profiles follow similar trends, which confirms that our observing setup and data reduction process produce reliable velocities.

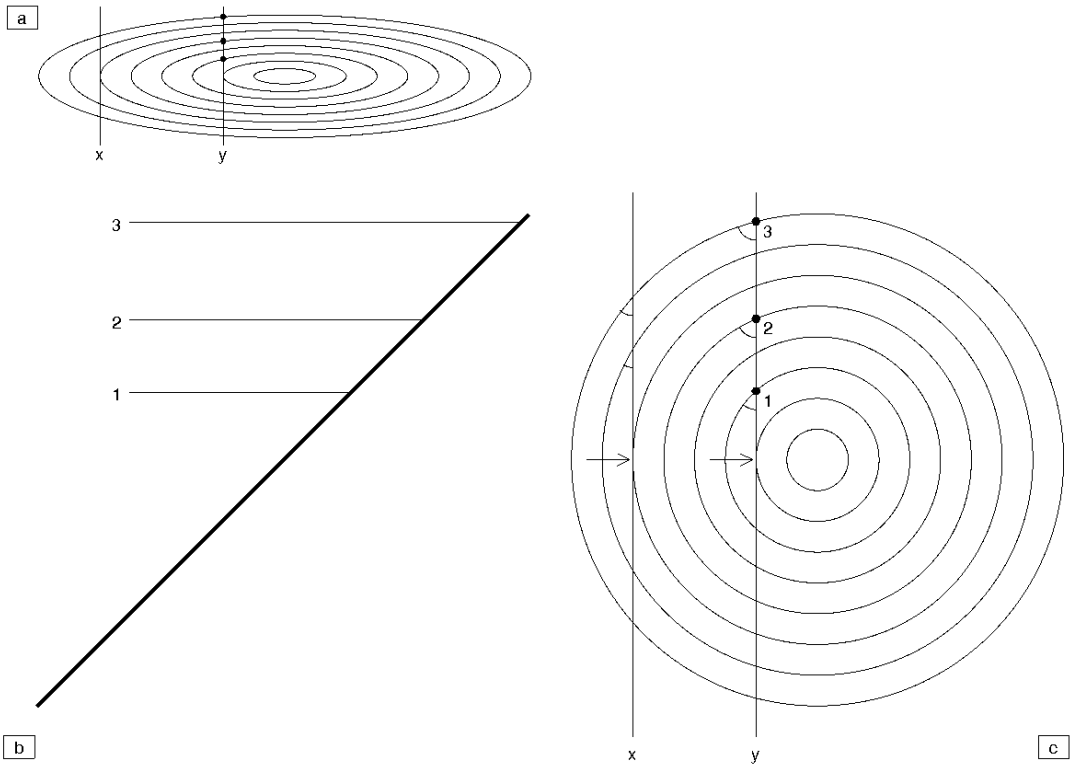

Fig. 2.14.— (a) shows a schematic for a non-edge-on disk with rings drawn at constant radial intervals. Our setup has 11 slits, but only two slits (x and y) are shown for simplicity. Three positions along slit y are marked with dots. (b) shows the same disk, but viewed from the side (relative to the observer's point of view). The same three positions along slit y in (a) are indicated. (c) shows the same disk, but viewed from a point directly above the disk on the disk's axis. The same two slits (x and y) are shown, and the points in the disk corresponding to positions 1, 2, and 3 are marked. Angles are drawn where each slit crosses one of the rings. Assuming constant velocity and circular rotation, a smaller angle (such as at position 1) means most (but not all) of the rotational velocity is along the observer's LOS. A greater angle (such as at position 3) means less of the rotational velocity is along the observer's LOS. Since the maximum rotational velocity is observed where the slit crosses the major axis (indicated by arrows), the observed rotational velocity will decrease as distance from the major axis increases. The change in observed velocity from the major axis to the edge of the disk is greater for slits closer to the center of the disk (slit y) than for slits near the edge of the disk (slit x) because the direction of rotation of the outermost ring is almost perpendicular to the LOS for the central slits.

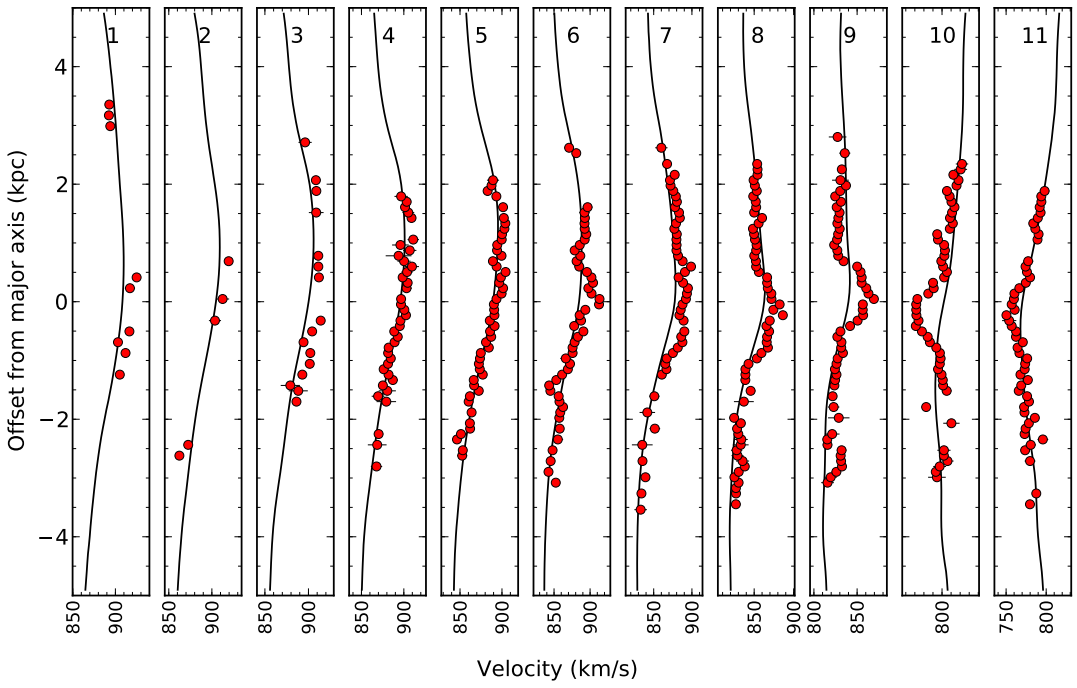

Fig. 2.15.— Heliocentric Hα velocities (circles) and HI velocities (solid line) are shown for each slit for NGC 4559. The kinematic center of the galaxy is between slits 9 and 10. Slits 10 and 11 are on the approaching (east) side of the galaxy, and the velocity profiles show a 'C'-shaped pattern. The remaining slits are on the receding (west) side of the galaxy and show the opposite pattern. This pattern is due to the viewing geometry of a non-edge-ondisk. The orientation of the slits (N is down, E is to the right) is the same as in Figure 2.13.

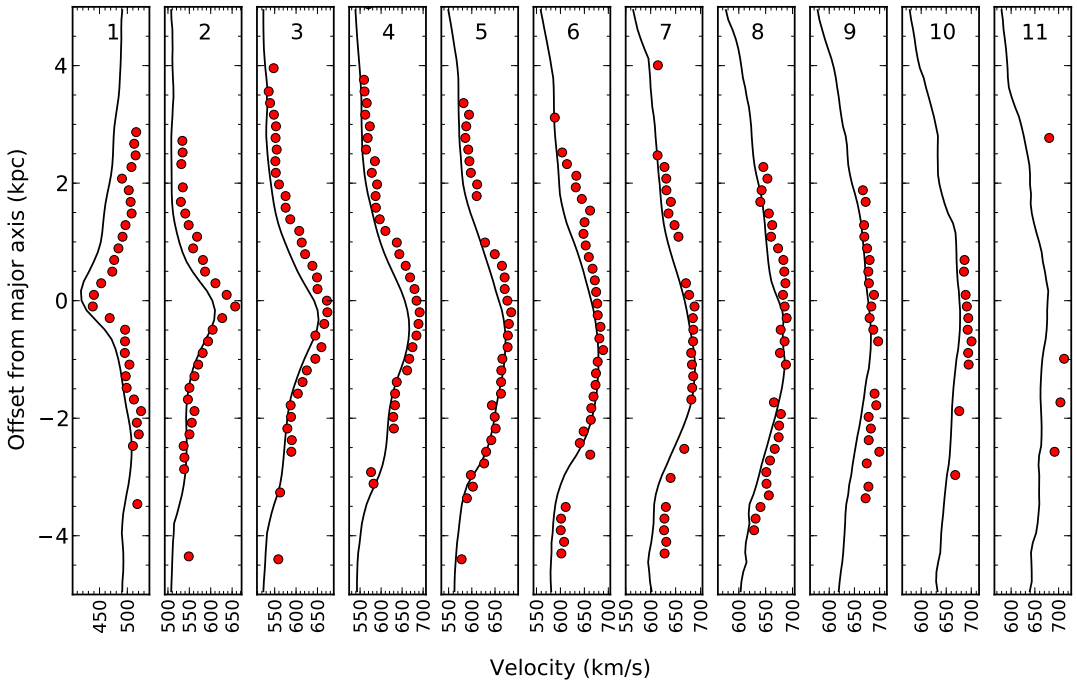

Fig. 2.16.— Heliocentric Hα velocities (circles) and HI velocities (solid line) are shown for each slit in the east field of NGC 5055. The center of the galaxy is between slits 1 and 2. Slit 1 is on the approaching (west) side of the galaxy, and the remaining slits are on the receding (east) side of the galaxy. The same curved pattern mentioned in Fig. 2.15 can also be seen in these velocity profiles. North is down, and east is to the right.

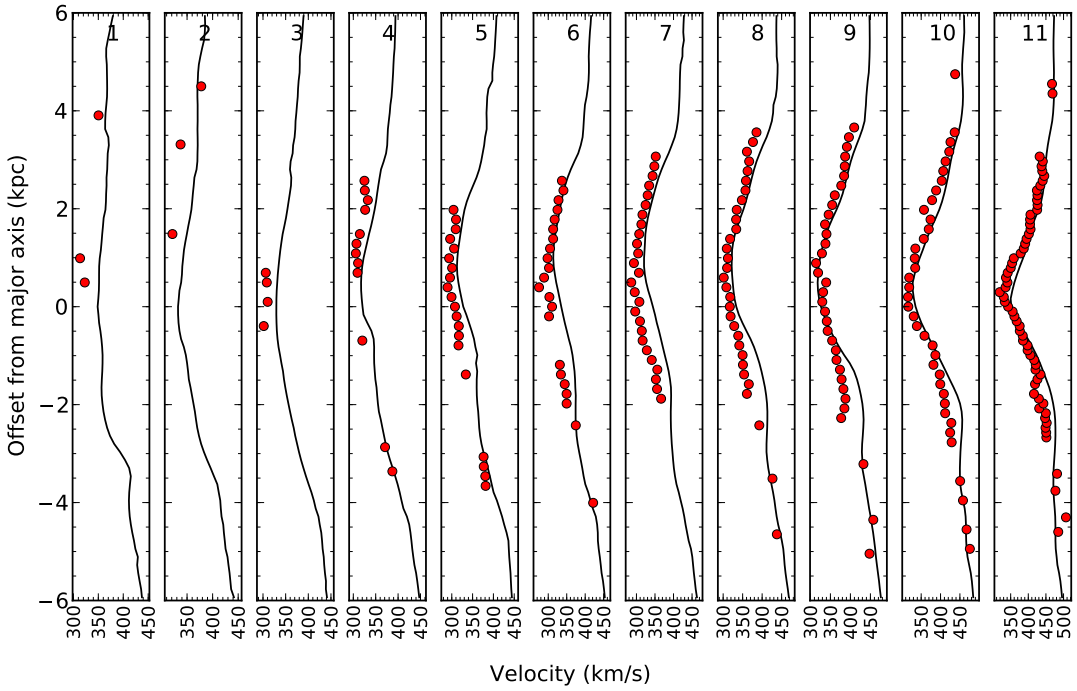

Fig. 2.17.— Heliocentric Hα velocities (circles) and HI velocities (solid line) are shown for each slit in the west (approaching) field of NGC 5055. Slit 11 is 7.5″ west of the center of the galaxy. North is down, and east is to the right.

3. MULTI-LONG-SLIT MODELING AND APPLICATIONS FOR NGC 891 AND NGC 4631

3.1. Introduction

We use a multi-long-slit spectroscopic setup to investigate the structure and kinematics of the extra-planar (EP) gas in two nearly edge-on galaxies, NGC 891 and NGC 4631. Our slit mask consists of 11 parallel slits that are overlaid with a narrowband filter to prevent neighboring spectra from overlapping. This setup is well-suited to measure velocities of Hα-emitting gas over a large field in each galaxy in a single exposure. By arranging the slits perpendicular to the major axis, we are able to measure radial velocity as a function of distance from the midplane at several radial distances within the galaxy. We can use this data to study the kinematics of EP ionized gas and to see if it lags the disk in rotation, which has been observed in several galaxies. We can also use line widths from our spectra to determine the locations and spatial extent of regions with broadened spectral lines, indicating possible outflows.

NGC 891 is a large Sb galaxy with a systemic velocity of 528 km s^{-1} (de Vaucouleurs et al. 1995) and a distance of 9.5 Mpc (van der Kruit & Searle 1981b). It has an inclination greater than 87.5° (e.g. Sancisi & Allen 1979; Rupen et al. 1987; Kregel & van der Kruit 2005), and Heald et al. (2006) assumed an inclination of 90° for their study of its ionized gas. Rossa & Dettmar (2003) measured a far-infrared luminosity surface density (L_{FIR}/D_{25}^2) of 3.19×10^{40} ergs s^{-1} kpc^{-2}. This indicates a moderate to high star formation rate, which Popescu et al. (2004) measured to be 3.8 M$_\odot$ yr^{-1}. Previous studies have shown that NGC 891 has a thick, extended EP gas layer in HI (e.g. Sancisi & Allen 1979; Swaters et al. 1997; Oosterloo et al. 2007) and in Hα (e.g. Rand et al. 1990; Dettmar 1990; Hoopes

et al. 1999).

A lagging component has been observed in NGC 891 in both optical (Rand 1997; Heald et al. 2006) and HI (Swaters et al. 1997; Oosterloo et al. 2007) data. Rand (1997) used single-slit spectroscopy, and Heald et al. (2006) integrated field unit observations. Because of the spatial coverage, our multi-long-slit setup is another technique that is well-suited to search for a lagging component in edge-on galaxies.

NGC 4631 is classified as an SBd galaxy with a systemic velocity of 613 km s^{-1} (Tully 1994) and an inclination between 85°and 90° (e.g. Hummel & Dettmar 1990 and Rand 1994, 85°; Israel 2009, 86°; Paturel et al. 2003 and Tikhonov et al. 2006, 90°). The west side of the galaxy appears closer to edge-on than the east side (see Figure 3.2). It is at a distance of 7.6 Mpc and has a star formation rate of 2.6 $M_{\odot}$ yr^{-1} (Heald et al. 2012). NGC 4631 has an extensive radio continuum halo (e.g. Ekers & Sancisi 1977; Hummel & Dettmar 1990; Irwin et al. 2012) and a large EP component of HI gas (Rand 1994). Extensive EP diffuse ionized gas (Rand et al. 1992; Hoopes et al. 1999; Martin & Kern 2001), dust (Neininger & Dumke 1999; Martin & Kern 2001), molecular gas (Rand 2000a; Irwin et al. 2011), and x-ray emission (Wang et al. 1995; Vogler & Pietsch 1996; Yamasaki et al. 2009) have also been observed in NGC 4631, implying this galaxy has a complex, multi-phase halo.

NGC 4631 has several companion galaxies and shows signs of interacting. There is an HI bridge between it and NGC 4656, a large, edge-on spiral located $\sim 30'$ ($\sim$70 kpc) to its southeast (Roberts 1968; Weliachew 1969; Weliachew et al. 1978). Martinez-Delgado et al. (2014) recently observed a stellar stream with one

component extending toward NGC 4656 and another component extending in the opposite direction with a ∼6.5 hour optical exposure. Their n-body simulations indicate this stream is consistent with satellite encounter. There is also a dwarf elliptical, NGC 4627, ∼3.0′ (∼7 kpc) to its northwest (e.g. Rand 1994; Irwin et al. 2011) and a possible optical dwarf galaxy, NGC 4631 DwA, ∼2 kpc south of its disk (Seth et al. 2005). Rand & van der Hulst (1993) and Rand (1994) found several HI spurs emanating from NGC 4631, which could be the result of tidal interactions with companion galaxies, and Rand (1994) identified three additional dwarfs near NGC 4631 with HI observations. Rand (2000a) found a CO shell, and Rand & van der Hulst (1993) found two HI supershells, and all three shells are within the optical disk of the galaxy. Based on the mechanical energy needed to produce these shells, their origin is best explained by interactions with small companions or large gas clouds falling onto the disk (Rand & van der Hulst 1993).

We describe our observations in §3.2 and our data reduction and calibration in §3.3. In §3.4 we discuss why modeling is necessary to analyze our data from edge-on galaxies and explain our modeling process. Results and analysis of our data and models are in §3.5, and we include a summary in §3.6.

3.2. Observations

We observed three fields (east, central, and west) in NGC 4631 in February and April, 2009, and in April, 2011. One field on the approaching side of NGC 891 was observed in November, 2009. We used the Dual Imaging Spectrograph (DIS) with the R1200 grating on the ARC 3.5m telescope at Apache Point Observatory near Sunspot, NM for all of our observations. We used a narrowband filter centered

on 6570 Å with a FWHM of 25 Å in series with our 11-slit mask, which consists of 11 1.5″ wide and 4′ long slits. The DIS grating has a dispersion of 0.58 Å pix^{-1}, and our velocity resolution for the setup was ∼65 km s^{-1}. The observing parameters are shown in Table 3.1. We aligned our slits perpendicular to the major axis in each galaxy, and slit positions for all four fields, overlaid on Hα KPNO images (Patterson & Walterbos 2013; Patterson 2013), are shown in Figures 3.1 and 3.2.

During each night of observing, we took blank sky frames for sky line subtraction at similar heights above the horizon as our target frames so we observed through a similar airmass. We took flat-fielding frames with a quartz lamp and wavelength calibration frames with an H-arc lamp mounted in the dome with the telescope in a similar position to the target frames to take into account any effects that flexure might have on the optics or rotation angle might have on the image rotator. All of our spectra and arc calibration frames were binned spatially by three pixels along the slit to increase the signal-to-noise ratio and decrease read out time.

Our slitmask setup was mounted in a filterwheel on DIS that also included the standard 1.5″ slit. The single slit is coupled to a slitviewer, which allows the observer to see where the telescope is pointed. At the beginning of each night, we measured the spatial offset between the center of the single slit and the center of the central slit on the multi-long-slit mask. With the single slit in place, we used the slitviewer to center on our desired field. We then applied our measured spatial offsets, which centers our target in the central slit on the multi-long-slit mask, and rotated the filterwheel so our multi-long-slit mask was in place for observing.

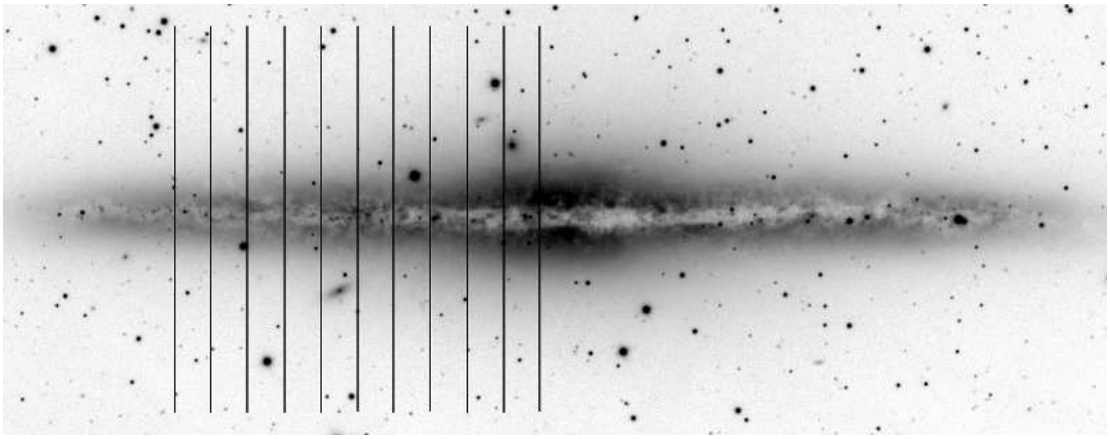

Fig. 3.1.— Slit positions for NGC 891 are shown on an Hα image (Patterson 2013). North is up, and east is to the left. The western-most slit is 7.5″east of the galaxy center, and the slits are spaced by 22.5″. The 11 slits span a horizontal range of 3.75′ (10.575 kpc), and each slit is 4′ (11.28 kpc) long.

3.3. Data Reduction

We use IRAF to perform basic reduction and calibration steps on our data. Multi-long-slit data for NGC 891 during various stages of data reduction and calibration are show in Figure 3.3 – 3.5. After subtracting the bias and flat fielding the galaxy and sky frames, we manually remove cosmic rays from our target spectra with the task IMEDIT. The spectra are visually inspected with varying levels of constrast and blinked against other exposures from the same field to remove cosmic rays to the best of our ability. The majority of cosmic rays do not overlap with the Hα emission, which simplifies this step. Cosmic rays in blank sky frames are removed automatically. We scale each of the sky spectra so they have similar sky line and continuum levels and then average them together with the task IMCOMBINE, which has a cosmic ray removal algorithm, CRREJECT, which ignores pixels with positive values above a certain threshold that are present in one frame but not the others. We do not use this automatic

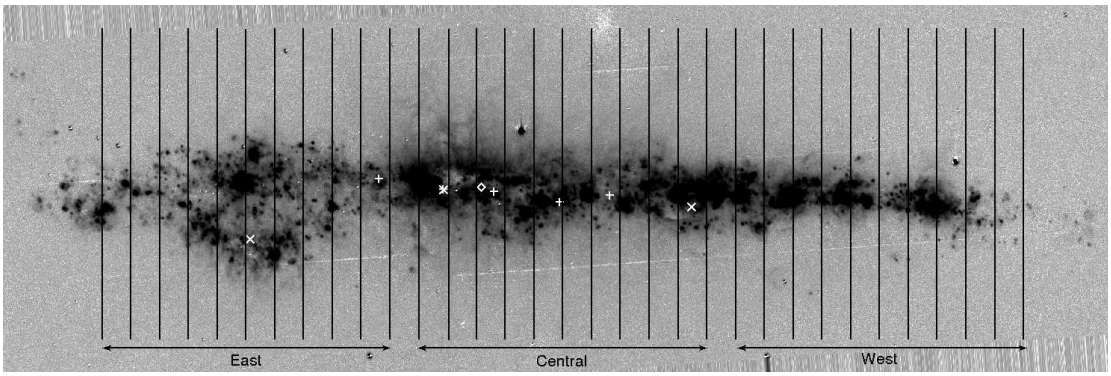

Fig. 3.2.— Slit positions for each of the three fields for NGC 4631 are shown on a continuum-subtracted Hα image (Patterson 2013). North is up, and east is to the left. The center of the galaxy is marked with a diamond. The five crosses mark locations of molecular outflow discovered by Irwin et al. (2011). The central X is where Rand (2000a) observed molecular outflow, and the outer two X's are HI supershells found by Rand & van der Hulst (1993). An X and a cross overlap to the left of the galaxy center. The 33 slit positions cover an area $12'$ (26.52 kpc) wide by $4'$ (8.84 kpc) long.

algorithm to remove cosmic rays from our galaxy frames because small shifts in the telescope pointing from one exposure to the next can cause large variations in brightness of the Hα emission we observe. Using an automatic clipping routine might accidentally remove Hα emission, which we would like to avoid.

After cosmic ray removal, all target spectra from the same field are aligned and co-added. We then wavelength calibrate our combined target frame and our combined sky frame with the tasks IDENTIFY, REIDENTIFY, FITCOORDS, and TRANSFORM. This straightens the spectral lines, which are curved due to spectrograph optics. To apply the standard IRAF tasks for calibrating single-slit spectra to our multi-slit spectrum, we treat our data as one continuous spectrum instead of a series of repeated spectra. The calibration frames for NGC 891 and NGC 4631 both consist of a series of 11 arc lines, each of which is at 6562.8 Å, but we assign artificial wavelengths to each arc line based on pixel separation

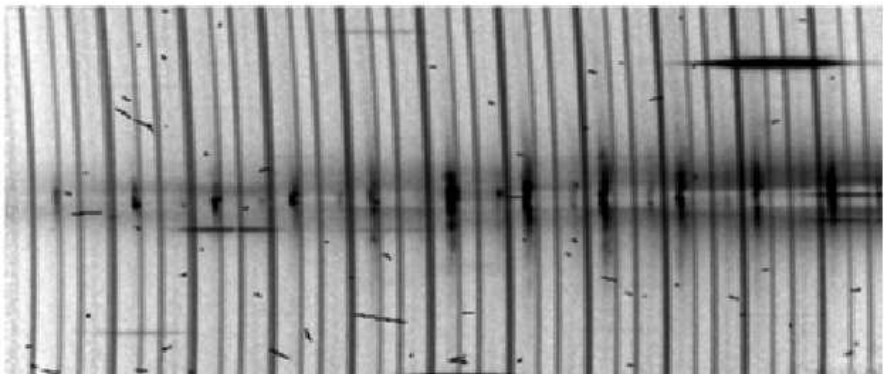

Fig. 3.3.— Multi-long-slit spectrum of NGC 891 before calibration. The north, approaching side is shown after bias subtraction and flat fielding. Wavelength is along the x-axis and inreases to the left, and the y-axis is the spatial direction. The vertical extent of the spectrum is 10.3 kpc (midplane ±5.15 kpc), assuming a distance of 9.5 Mpc. Spatially, north is up and east is to the left. The uniform, vertical lines are sky lines; the horizontal blobs are stars; and the vertical patches are Hα emission. The midplane of the galaxy runs horizontally, and a prominent dust lane can be seen. The spacing of the slits is 22.5″(∼1 kpc), and the center of the galaxy is 7.5″to the west of the spectrum.

and spectrograph dispersion. We measure the dispersion of the spectrograph each night using sky lines in a raw sky frame. Observations for both galaxies were done with the 6570 Å filter, which results in three sky lines per slit. The dispersion is measured at several points along each slit for all 11 slits, and we use the average value as the dispersion when calibrating that night's data. The variation in dispersion across the entire field is typically of order 10^{-2} Å pix^{-1}, which translates to an instrumental error of a few km s^{-1} when we calculate our velocities. The derived uncertainty in dispersion for each field is included in the total uncertainty of each velocity measurement.

After calibrating our target and sky frames, we smooth the sky frame by three pixels in the spatial direction and subtract it from our galaxy spectrum to remove sky lines. If the relative sky line intensities are different in the sky and galaxy frames (which can be caused by changing weather conditions or moonlight), we

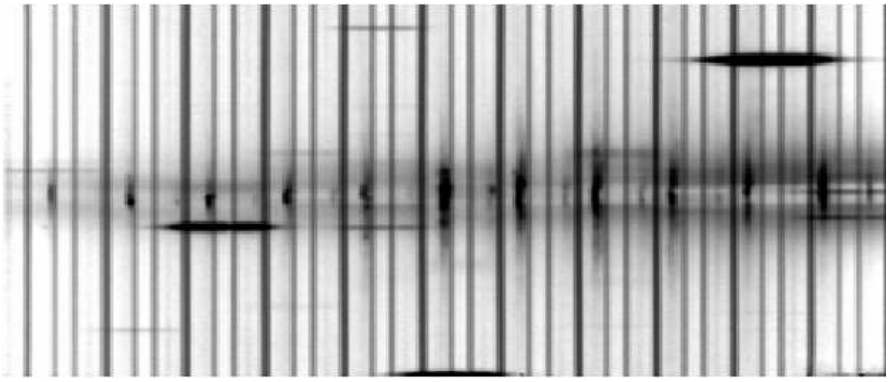

Fig. 3.4.— Wavelength calibrated multi-long-slit spectrum of NGC 891. Cosmic rays have also been removed. The orientation and extent of this spectrum are the same as in Figure 3.3.

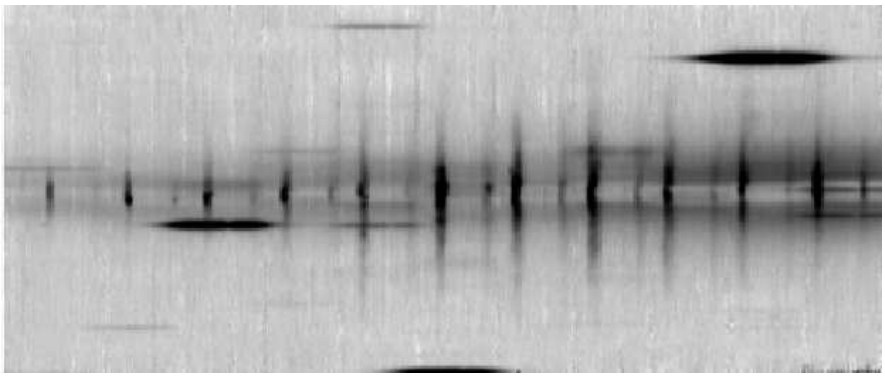

Fig. 3.5.— Multi-long-slit spectrum of NGC 891 after sky subtraction. Faint NII emission at 6583 Å can be seen between the Hα emission from each slit. The orientation and extent of this spectrum are the same as in Figure 3.3.

optimize sky line subtraction for the sky line closest to our observed Hα. For NGC 891, we further improved sky line subtraction by removing remaining sky line remnants with the IRAF task BACKGROUND, which fits a function along each column according to user-specified sections of the frame that are free of Hα emission. This is representative of the background level for that column and is subtracted from the spectrum. Our final spectrum for NGC 891 can be seen in Figure 3.5.

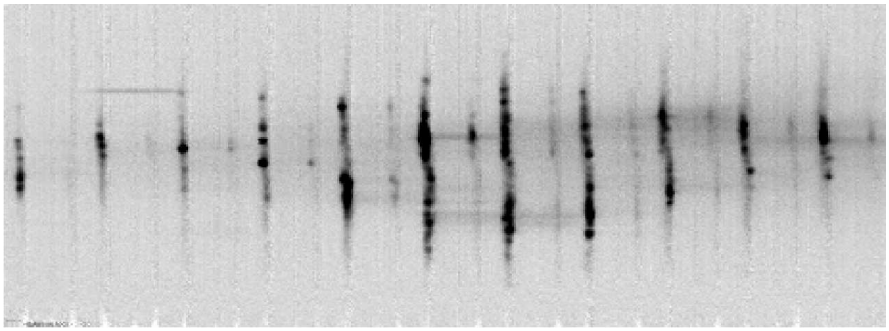

Fig. 3.6.— Multi-long-slit spectrum for NGC 4631 east. North is up, east is to the left, and the midplane of the galaxy runs horizontally. Wavelength is along the x-axis and increases to the left, and the y-axis is the spatial direction. The vertical extent of the spectrum is ± 3.7 kpc ($\pm 1.7'$) from the midplane, assuming a distance of 7.6 Mpc. Fainter [NII]6583 Å emission can be seen between the Hα emission from each slit.

For the central field of NGC 4631, subtracting the sky frame resulted in a very clean sky line subtraction, so we did not do further removal with the BACKGROUND task. For the east and west fields, which were observed on the same night, the sky lines in our sky frame did not match the sky lines in the target frames very well. This could have been caused by changing observing conditions or the fact that the sky and target frames were taken at very different times during the night. In the west field, the observed Hα emission is separated in wavelength space from the sky lines, so we are able to measure the Hα emission without subtracting the sky lines. The Hα emission in the east field of NGC 4631 falls very close to the sky line doublet at 6577.28 Å, so we use the BACKGROUND task to remove sky lines.

Observations of the central field of NGC 4631 spanned several nights, so we performed our reduction, calibration, and sky line subtraction procedures for each night of data. We then summed the final spectrum from each night to produce a final, combined spectrum for that field. The final spectra for the east, central,

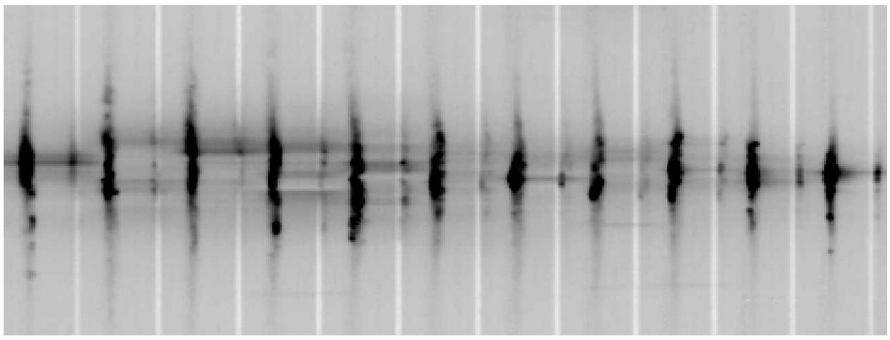

Fig. 3.7.— Multi-long-slit spectrum for the NGC 4631 central field. The spatial extent of this spectrum is ±3.9 kpc (±1.8′) from the midplane. The center of the galaxy is between the 3rd and 4th slits from the left. The white, vertical stripes are oversubtracted sky lines. The orientation of this spectrum is the same as in Figure 3.6.

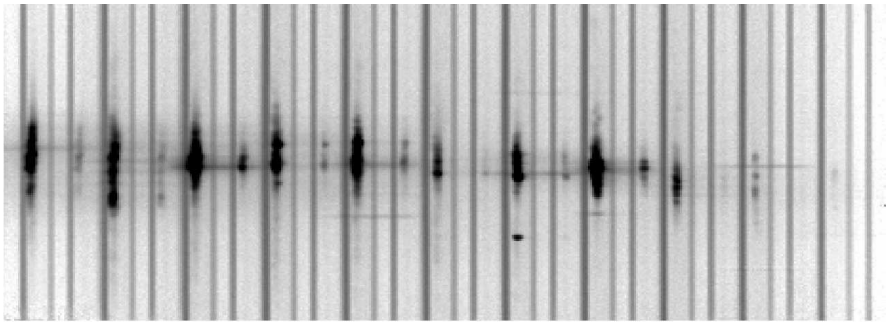

Fig. 3.8.— Multi-long-slit spectrum for NGC 4631 west. The spatial extent of this spectrum is ±3.5 kpc (±1.6′). We did not do sky line subtraction because the Hα emission is sufficiently separated in wavelength space from the sky lines. The sky lines appear as parallel, vertical stripes, and there are three sky lines per slit. The orientation of this spectrum is the same as in Figure 3.6.

and west fields are shown in Figures 3.6 – 3.8.

3.3.1. Velocity Measurements

Once we have our final spectrum for a given field, we measure the wavelength of the emission in each slit at a range of distances from the midplane. Where there is ample emission, such as near the midplane, we sum four rows, which corresponds to a spatial extent of 4.8″. We use the IRAF task SPLOT to fit a

Gaussian to the emission profile. At greater distances from the midplane or in places where the emission is fainter, we sum up to eight lines. We take the centroid of the Gaussian to be the wavelength of the observed Hα emission. We measure the centroid of the 6577.28 Å sky line doublet in a similar manner and take the difference between that and the Hα centroid to determine the true wavelength of the observed emission at that point, and we use that value to calculate the velocity of the Hα-emitting gas:

$$v = \frac{\lambda_{sky} + (\lambda_{H\alpha,obs} - \lambda_{sky,obs}) - 6562.82 \text{ Å}}{6562.82 \text{ Å}} \times c \tag{3.1}$$

where λ_{sky} is the wavelength of the sky line doublet (6577.28 Å), $\lambda_{H\alpha,obs}$ is the observed wavelength of the Hα emission, $\lambda_{sky,obs}$ is the observed wavelength of the sky line, 6562.82 Å is the rest-frame wavelength of Hα, and c is the speed of light. Based on the date and time of the observations, we then use the IRAF task RVCORRECT to determine a velocity offset to correct for the Earth's motion, which gives us heliocentric velocities for our data.

SPLOT calculates an uncertainty in wavelength for each Gaussian centroid based on the noise level in the data on either side of the profile. The uncertainties from the sky line and emission centroids are added in quadrature to the instrumental error from the dispersion measurement to obtain the total uncertainty for each velocity measurement. Our centroid velocities for NGC 891, overlaid with velocities from our models (solid and dotted black lines; see §3.5.1 for a more detailed discussion), are shown in Figure 3.9. Velocities near the midplane are obstructed by dust, so we cannot measure the actual rotational velocity. This results in a rapidly fluctuating, v-shaped peak in velocities near the midplane, which we do not try to fit with the models. If we ignore velocities near the midplane and

focus on the velocities 0.5 kpc and farther from the major axis, we see an increase in velocity as we move away from the midplane, especially in slits 4-10. This is indicative of a lagging thick disk.

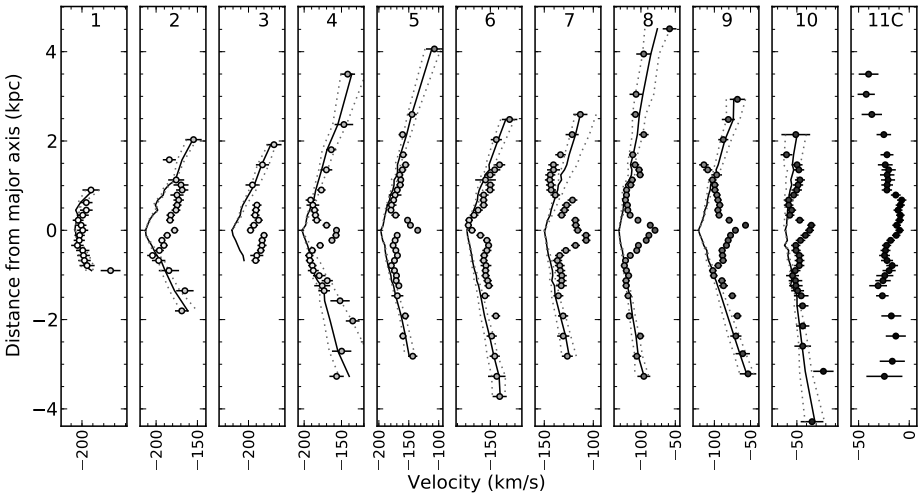

Fig. 3.9.— Centroid velocities for NGC 891 are plotted with circles, and the solid and dotted lines show the model centroids, which are discussed in §3.5.1. Velocity increases to the right, and the tickmarks are spaced by 10 km s^{-1}. Observed velocities show a sharp increase near the midplane in several slits because dust prevents us from seeing to the tangential point where we would observe the actual rotational velocity. Because this is the approaching side of the galaxy, increasing velocity with distance from the major axis is indicative of a lagging component. The systemic velocity (528 km s^{-1}) is shown in slit 11 as a dashed line.

3.4. Multi-long-slit Modeling

Because our target galaxies are almost edge-on, their emission line profiles will likely be non-Gaussian. Assuming a line of sight (LOS) that goes through the entire disk of an edge-on system, the maximum rotational velocity will be observed at the point where the LOS is perpendicular to the direction of the center

of the galaxy. At positions in front of and behind that point, the component of the rotational velocity that is along the LOS is smaller due to projection effects. If the gas density of the galaxy decreases with radius, this will produce an emission profile with a peak at the maximum, tangential velocity and an asymmetric, low velocity tail. Fitting a Gaussian to this type of emission profile and using the centroid to measure the velocity is an acceptable first-order approximation to study motions of the gas, but it may not be a true representation of the actual rotational velocity. Our spectral resolution is not sufficient to measure the tangential velocity directly, which is why we use Gaussian-fitting. To determine the best estimate of the tangential velocity from the fit, we model each galaxy specifically for our multi-slit setup. We measure centroids of our observed and model profiles to account for any bias that centroid-fitting might have on asymmetrical emission profiles.

Our models are specifically meant to focus on the shape of the emission line, and we do not include effects of extinction due to dust. These effects play an important role in and near the midplane, and we take this into consideration in our analysis of each galaxy. We omit velocity measurements from emission profiles that show effects of dust, since dust extinction prevents us from measuring the true rotational velocity at those points.

3.4.1. Model Inputs

The basic inputs for our models include an edge-on galaxy's systemic velocity, distance, optical radius, inclination, and rotation curve along the midplane. We generally use a rotation curve taken from HI data. Since HI is likely optically

thin, it is easier to measure rotational velocities within the midplane with HI than with optical data, which are often affected by dust and extinction. It is also possible that bright HII regions along our LOS prevent us from observing gas at the tangential point near the midplane of the target galaxy.

Our models also incorporate observed scale length and scale height of the ionized gas disk. For NGC 891, these two quantities are measured directly from our multi-slit observations. To measure scale height, we take cuts along slits with measurable emission at larger distances from the midplane. Since Hα intensity scales with the square of the gas number density, we take the square root of the number of counts we observe to determine the number density of the ionized gas as a function of height along each slit. We average the counts from several slits and fit an exponential to the data to determine the scale height (Figure 3.10). We measure an observed exponential electron scale height of 1.27 kpc for NGC 891. This is similar to what Heald et al. (2007) and Dahlem et al. (1994) measured (1.4 kpc and 1.15 kpc, respectively), both of whom assumed the same distance that we did (9.5 Mpc).

We repeat the process with cuts parallel to the midplane just above and below the dusty region in the disk's midplane to measure the observed electron scale length. The top plot in Figure 3.11 shows the average of the two cuts. Each tall peak is the Hα emission from that slit. Smaller peaks between the Hα peaks are residual sky lines that were not completely subtracted from the data. The left side of the plot is toward the center of NGC 891, which is why it has a higher continuum level. Since we want to measure scale length of the Hα itself, and not the sum of the Hα and background emission, we fit a line to the background level and subtract it from the data. The result is shown in the bottom plot.

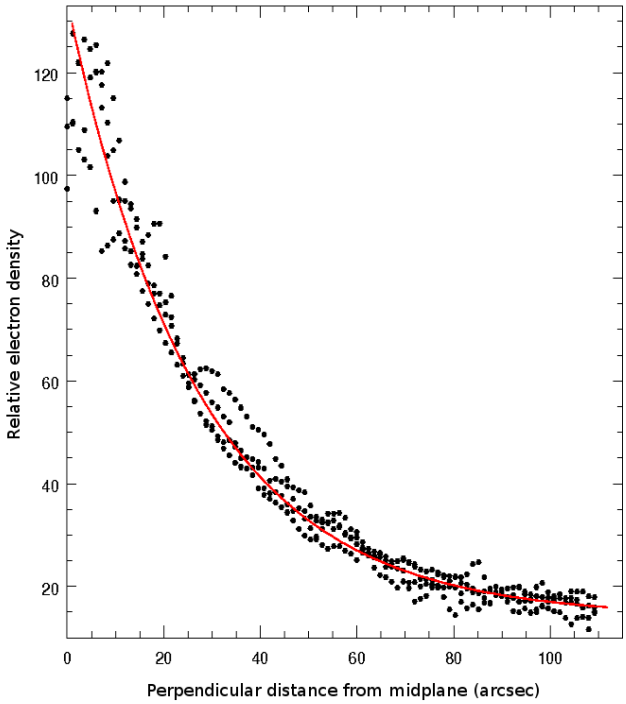

Fig. 3.10.— Scale height for NGC 891. The points are data from the four central slits, starting at the midplane and moving outward from the disk. The solid line is the exponential fit used to determine the scale height, which we measured to be 1.27 kpc. The x-axis is distance above/below the midplane in the vertical direction. The y-axis is the relative electron density inferred from the observed intensity.

An exponential fit with a scale length of 1.44 kpc is overlaid on the background-subtracted data. The left-most six slits, which are closer to the galaxy's center, have similar Hα levels, so we assume a constant Hα density in the inner part of the galaxy. The outer five slits roughly follow an exponential decrease in Hα density.

NGC 4631 shows more patchy emission and dust attenuation, so we use a KPNO Hα image (Patterson 2013) to more accurately measure a scale height and length. We measure a scale height of 0.85 kpc (assuming a distance of 7.6 Mpc). Hα emission is roughly constant in the radial direction out to 6.6 kpc. Beyond

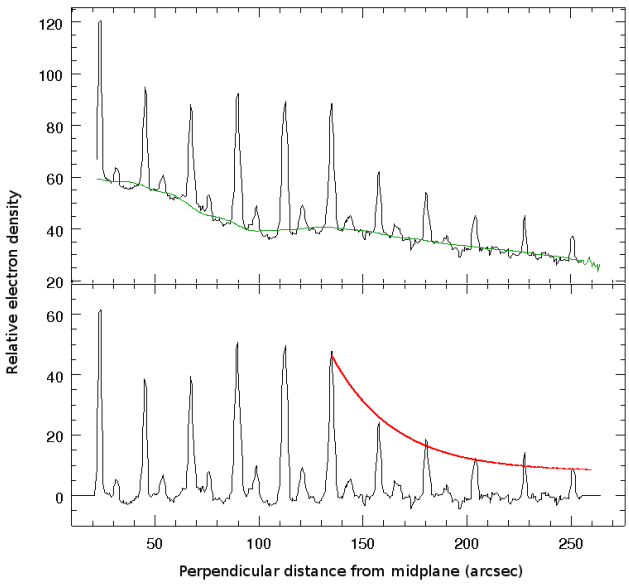

Fig. 3.11.— Scale length for NGC 891. The black line in the top plot is a horizontal cut through the multi-slit data. The y-axis is the electron number density. High peaks are Hα emission from the 11 slits. Lower peaks are sky lines. The smooth line is an empirical fit to the continuum emission level. The slits on the left side of the plot are toward the galaxy center, where continuum emission is higher. The bottom plot is the same cut through the multislit data after subtracting the continuum fit, and the line starting at the middle slit is an exponential fit to the Hα peaks. We assume a constant Hα surface brightness for the inner 6 slits and an exponential drop off with a scale length of 1.44 kpc for the outer 5 slits.

that, the emission drops exponentially with a scale length of 12.9 kpc. For both measurements, we used a section of the Hα image that overlaps with our multi-slit field.

The scale height and length that we measure are the observed values of the Hα emission and not the intrinsic values of the ionized gas itself. NGC 891 and NGC 4631 show a lot of attenuation of Hα emission due to dust. The data we use to measure the scale height and length are restricted to locations away from the midplane that show less dust extinction, but the effects of dust are not completely absent from our measurements. The distribution of emission that we observe is

a combination of the Hα-emitting gas and the absorbing dust. Howk & Savage (2000) studied NGC 891 and determined that these two components are physically distinct phases of the thick disk and have different spatial extents and distributions. Kamphuis et al. (2007) modeled the Hα-emitting gas and a dust disk for NGC 891 and found that they have very different scale lengths ($\sim$5 kpc and 8.1 kpc, respectively). Using our observed scale lengths and heights result in models with the appropriate overall intensity for the Hα emission. We note that the exact values are not critical for our purpose. We mostly want to obtain similar S/N ratios in our models and data.

The parameters described above produce a basic model of a circularly rotating disk with a smooth, exponential density distribution in both the radial and z-height directions. To reproduce our multi-slit observations, we take into account the position of each slit relative to the galaxy's center and the pixel scale and dispersion of our spectrograph. This allows us to extract model profiles at the same radii and distances from the midplane as our observed emission profiles. A vertical rotational velocity gradient of the ionized gas is also included as input for the models, and this is the parameter that we vary for each model.

3.4.2. Model Computations

To generate a model for each position along each slit, we start at the tangential point in the midplane of the galaxy. Stepping through the disk in small increments, we calculate the rotational velocity based on the distance of each increment to the galaxy's center, a linear interpolation of the rotation curve, and the inclination of the galaxy. A specified optical radius acts as a cutoff, outside of

which no Hα emission is observed. We assume circular rotation for all points in the galaxy, and the observed velocity along the LOS is computed from the viewing geometry for each increment.

We calculate the gas density for each increment based on the radial distance within the plane and scale length. The observed intensity, or emission measure, of Hα emission scales as the square of the gas density. After calculating the emission measure and the observed velocity for every increment for the LOS through the disk for a given slit, we sum the emission as a function of velocity, binning the measurements by 5 km s^{-1}. This gives our models a dispersion of 0.1077 Å pix^{-1} and produces a high resolution emission profile.

We repeat this process of calculating density and observed velocity for all points along each of the slits. Each vertical increment along each slit is 1.2″, which is the binned DIS pixel scale. The specified distance to our target lets us calculate the physical z-height above the disk that each vertical slit increment corresponds to. For models with a lagging component, which is given in km s^{-1} kpc^{-1} to be consistent with the literature, the midplane rotational velocity is scaled by the vertical velocity gradient, and then the observed velocity along the LOS is calculated. The gas density for each increment is calculated from the midplane gas density (which depends on the radial distance and scale length), scale height, and perpendicular z-height above the disk.

The initial output for each model is a multi-slit spectrum with the spatial direction along the y-axis to match our observed spectra. The observed velocities are converted to wavelength with the Doppler equation using the assigned Hα wavelength (from our data reduction process; see §3.3) for each slit as the

rest-frame wavelength. This results in wavelength being along the x-axis of the spectrum.

Once we have our initial high-resolution model spectrum for our observed field, we convolve it with the telescope response function. We use a calibration arc frame from our observations, which consists of a series of 11 Gaussian-type profiles (one from each slit), to obtain the response function. We take the average of the 11 profiles, which has $\sigma \sim 65$ km s^{-1}, and we convolve this with the multi-slit model spectrum. The last step to match our models to the technical specifications of our observing setup is to re-bin the spectrum in wavelength space so the model dispersion matches that of our data.

3.4.3. Signal-to-noise Scaling

Next we scale our model spectrum to a proper intensity level. Because an arbitary central density, which affects the amplitude but not the shape of the model emission profiles, is used to calculate the gas density at each increment, the model spectrum must be scaled so that each slit matches the observed intensity of the multi-slit data. We determine a scaling factor for each model slit to account for the fact that our observations sometimes show patchy Hα emission. The global scale length and scale height that we measure from our data provide a starting point for matching the model emission to the observed emission, but the smooth density distribution of our models does not always reflect the actual density distrubution of the galaxy. Our data are often characterized by an underlying smooth distribution overlaid with bright clumps of Hα emission. To reproduce this in the models, we measure the emission from the data as a function along the

slit and subtract the background continuum level to get the intensity of the Hα emission only along the slit. The resulting profile is used as a scaler for that slit for all models of that galaxy.

To add an appropriate level of noise to our models, we identify five consecutive columns in each slit that are free of Hα emission and sky lines. We refer to those columns as the background pixels for that slit. 'Background' refers to continuum emission from the galaxy, which is prevalent near the midplane, and sky emission. For a given point along a slit, the background we incorporate into the models is dependent upon the average and standard deviation of a 5x5 block of background pixels that is centered spatially on that point. Using Python's numpy.random.normal routine, we generate a random value from a Gaussian distribution with our desired average and standard deviation. We do this for each column of a given point along a slit. This results in the background and noise levels of each profile we extract from the model spectrum having a similar mean and standard deviation as the data.

Fig. 3.12.— Final model spectrum for NGC 891. Each slit in our model spectrum has been scaled so the emission levels are similar to that of our observations. Background and noise levels have been added so the model signal-to-noise level is similar to that of our data. The model shown here has a lag of 17 km s^{-1} kpc^{-1}. The spatial direction is along the y-axis, and wavelength increases to the left along the x-axis.

Background and noise levels are added after we scale our models so the Hα emission levels remain similar to our observed levels, and our final version of the model has a similar signal-to-noise ratio as our data. One of our final model spectra for NGC 891 is shown in Figure 3.12.

3.4.4. Determination of Best-fit Model

After scaling our models and adding noise, we use the same routines on our models as we do on our data to measure velocities. The same rows are summed for a given slit, and we use the IRAF task SPLOT to fit a Gaussian to the model emission profile, measure the centroid, and calculate the velocity. We run models with a range of values for the vertical velocity gradient to determine which value of a lag, if any, best matches the observations.

When comparing the models to the data, we restrict our measurements to those that do not show the effects of dust near the midplane. In the case of NGC 891, this means we exclude data points that are within 1 kpc of the midplane. For the remaining points, we calculate the average of the residuals between the data and each model for each slit and subtract that value from each of the model measurements. This accounts for any velocity shift between the data and models that might arise from differences between our input rotation curve and the actual one. We then calculate a reduced χ^2 for each model.

Our input rotation curve has a slight effect on the shape of our model spectral lines, but it has a much greater effect on the measured midplane velocities of our models. To reduce computing time, we do not fit the rotation curve of the galaxy; instead, we use a rotation curve previously derived from HI or Hα data.

Differences between our input rotation curve and the actual rotation curve of the Hα-emitting gas produce a zero-point shift in velocity between the data and the models, but the slope of the velocity profile is unaffected. Since the slope is indicative of the lagging component, we want to compare the slope of the velocity profile of the data to the slope of the model velocity profile. Calculating a reduced χ^2 from the residual-subtracted models accomplishes this.

Depending on the shape of the velocity profiles from different slits, we can calculate the reduced χ^2 for a specific range of slits or for specific range of distances from the midplane. This allows us to measure a vertical velocity gradient for a certain quadrant of a galaxy or to determine if the value of the lag changes with distance from the galaxy center.

Because the data points are more closely spaced closer to the midplane (but still excluding the points that are affected by dust), our reduced χ^2 calculation could be more sensitive to these points. However, when determining whether we detect a lagging component, velocity measurements farther from the midplane are more important than velocities that are closer to the midplane. To account for this, we use the best-fit model indicated by our reduced χ^2 calculation as a starting point to determine which model best fits the data. We then do comparisons by eye between models with different lags centered on this starting lag and the data to more accurately determine what value of a lag best fits the data for individual slits or for a group of slits.

3.5. Results and Analysis

3.5.1. NGC 891 Velocity Profiles

We detect ionized EP gas at least 2 kpc from the midplane in every slit except slit 1, which is the farthest slit (10.9 kpc, or 3.875′) from the galaxy center. In several slits, we see EP gas up to 4 kpc from the midplane. The emission in the 6 inner slits is fairly constant, which reflects the boxy nature that has been observed in the ionized gas distribution of NGC 891 with Hα imaging (Rand et al. 1990; Dettmar 1990).

Velocity profiles for each slit for NGC 891 are shown in Figure 3.9. The profiles for slits 1-10 show an overall curved pattern, similar to a 'less than' sign, and most of those slits show a peak in velocity near the midplane. Since NGC 891 is close to edge-on and we are looking at the approaching half of the galaxy, the increase in observed velocity with distance from the major axis is due to the fact that the extraplanar gas is lagging the midplane in rotation. Slower rotational velocities toward the observer result in greater recessional velocities.

The localized peak in velocity near the midplane that is apparent in the observed profiles of slits 4-10 is due to dust obscuring our view of the Hα-emitting gas. The abundance of dust near the midplane of NGC 891, as well as the fact that dust is more prominent in the inner part of the galaxy, can be seen in our gray-scale spectrum (Figure 3.5). Instead of observing gas that is at the tangential point along our line of sight, dust limits our observations to gas that is in front of the tangential point. Only a component of the velocity of this gas is along our line of sight, so we measure a velocity that is less than the actual rotational velocity of the gas. Similar to the effect described above, this decreased rotational velocity

translates to an increase in observed recessional velocity.

At distances greater than ±0.5 kpc from the midplane in slits 4-6 and distances greater than ±1 kpc in slits 7-10, the velocities become less stochastic. This is where the effects of dust become less prominent, so we are likely measuring the actual rotational velocity of the gas.

3.5.2. NGC 891 Model Profiles

We did not fit a lag to the inner-most slit (slit 11) because at that slit location, 0.125′ from the center, most of the velocity along our line of sight is the systemic velocity of the galaxy, and it does not show the rotational velocity of the gas. Models with lags of 0 and 30 km s^{-1} kpc^{-1} show only a small difference for that slit, and they are essentially the same to within the errorbars of the data. Slit 11 seems to show the opposite of a lagging component on the upper half, but this is likely due to dust extinction. The dotted line for that slit in Figure 3.9 shows our best estimate of the rotational velocity at that radius. We chose our estimated rotational velocity as the velocity which passes through most of the data points (within the error bars) that are 2 kpc and farther from the midplane, with the condition that any data point that does not fall on the dotted line must have a greater velocity than our estimated one. Dust or bright HII regions would cause us to observe higher velocities than the rotational velocity (because we are observing the approaching side of the galaxy), and observing lower velocities is not likely for this field because we see no evidence of outflows or counter-rotating features. We therefore chose our estimated velocity to be the highest minimum velocity that the data support. Figure 3.14, which is described in more detail below, shows that

our estimated rotational velocity for this slit is in strong agreement with Rand (1998).

Slits 1-10 have centroid velocities from our best-fit models overlaid on the data as solid black lines. Our models assume a transparent disk, so there may be a large discrepancy between the observed and model velocities in places where dust or bright HII regions prevent us from sampling the entire line of sight. The dotted lines show the centroid velocities for the models with the highest and lowest values of a lag that fit the data within the errobars. Some slits, such as slit 4, have a wide range of possible values for a lagging component because the data points show an amibiguous pattern. Our model gradients are constant with distance from the midplane, so the model velocity profiles are relatively smooth. Any wiggles in the profiles are from a lower signal to noise ratio in the models at those particular pixels and are not a feature of the model. As we described in §3.4.4, we allow the model profiles to have a constant velocity shift when finding the best match to the data. Each slit has its own shift, and that shift is the same for all models. We fit the data in the upper and lower halves of each slit independently, but we require that both halves have the same midplane rotational velocity.

Figure 3.13 shows our best-fit vertical velocity gradient as a function of radius for the upper and lower halves of slits 1-10. We do not include the lag we fit to the upper half of slit 2 (31 km s^{-1} kpc^{-1}) because a lack of data points makes that value unreliable. The same is true for the lower half of slit 3, where a foreground star prevents us from making any measurements. Slit 1 does not show any extraplanar emission more than 1 kpc from the midplane, but the majority of the data points between -1 and 1 kpc show a very regular pattern free of dust absorption, so we include our model lag value for that slit. The lowest data point

for that slit appears as a faint but distinct feature in our gray scale spectrum and is likely an Hα-emitting region along our line of sight. If this is the case, then we may not be measuring the tangential rotational velocity, so we exclude this point from our model fits.

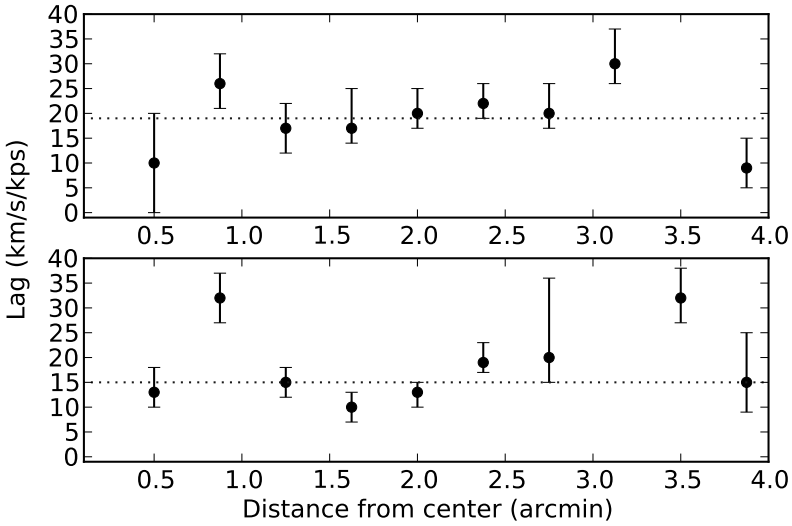

Fig. 3.13.— Lag as a function of radius for NGC 891. The upper and lower panels show lag values for above and below the disk, respectively. Slit 10 (at 0.5′) is the inner-most slit shown. The dotted lines show the best-fit global value for the lag for all 10 slits: 19^{+7}_{-4} km s^{-1} kpc^{-1} above the disk and 15^{+12}_{-2} km s^{-1} kpc^{-1} below the disk.

The lags above and below the disk of NGC 891 show a similar pattern of lag as a function of radius. The values for the outer-most slits are less reliable because, even though the models provide a good fit, the observable emission is limited to close to the midplane. The lag in the inner part of the galaxy jumps around for the inner-most three points (slits 8 – 10) and then becomes fairly constant with radius after that. The point at a radius of 0.875′ corresponds to slit 9. This slit

has the faintest emission of the inner slits and significant absorption from dust, so the lag measured for that slit could be anomalous.

The dotted lines in Figure 3.13 show our best fits for a global value for the vertical velocity gradient for the upper and lower halves of NGC 891. The upper half corresponds to the northwest quadrant of the galaxy and is best fit by a lag of 19^{+7}_{-4} km s^{-1} kpc^{-1}. The northeast quadrant is best fit by a lag of 15^{+12}_{-2} km s^{-1} kpc^{-1}.

Figure 3.14 shows a comparison of the rotation curve derived from our models with centroid velocities from Rand (1998). Our rotation curve is taken from the midplane velocity of each slit's model profile (as shown in Figure 3.9), with the exception of slit 11 (the inner-most slit), which we estimated to have a rotational velocity of 495 km s^{-1}. Our estimate is in excellent agreement with the data from Rand (1998). Our models assume that the lagging component has a constant velocity gradient with height from the midplane. If the gas velocity as a function of height is actually constant near the midplane and only begins to decrease at, e.g., 0.5 kpc from the midplane, then our rotation curve is an over-estimate. Based on the data in Figure 3.9, this would have the largest effect on slits 2-4. If the velocity gradient is higher near the midplane, then our rotation curve is an under-estimate. However, the dotted line in Figure 3.14 shows heliocentric centroid velocities of the ionized gas from Rand (1998) at a distance of 0.7 kpc from the midplane on the eastern side of NGC 891. A comparison between their data set and ours shows an average decrease of $\sim$15 km s^{-1} between the midplane rotation curve and the rotational velocities at 0.7 kpc from the midplane. This corresponds to a lag of 21.4 km s^{-1} kpc^{-1}, which is in agreement with what we measure at distances of 1.0 kpc and greater from the midplane. This indicates

that the magnitude of the lag is relatively constant with height from the midplane.

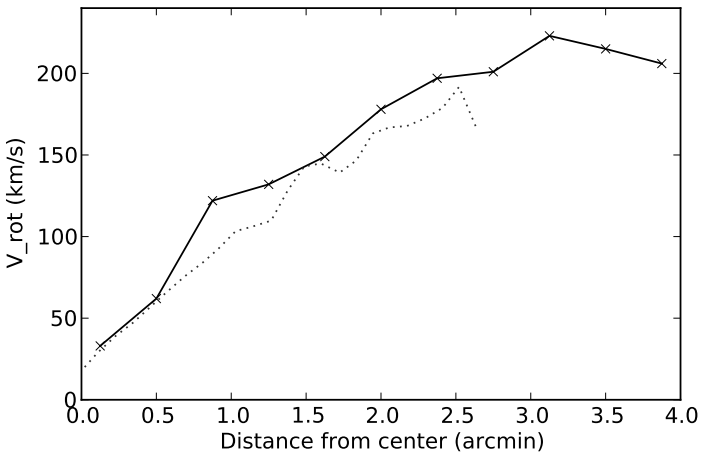

Fig. 3.14.— The rotation curve for NGC 891 derived from our models is shown as a solid line, with x's marking the individual points. The velocity uncertainty is 5 km s^{-1} for each point. Centroid velocities from the ionized gas 0.7 kpc below the midplane, taken from Rand (1998), are shown as a dotted line and have uncertainties of 1-2 km s^{-1}. Our midplane velocity for each slit was determined by allowing the velocity profile to shift slightly so that the model velocities match the observed velocities at distances of 1 kpc and greater from the midplane. These velocities assume a constant velocity gradient with height from the midplane. Based on the shape of the profiles in Figure 3.9, our midplane velocities for the outer-most slits could be overestimates. Comparing our velocities to the velocities from Rand (1998), the velocity gradient starts very close to the midplane.

Our results for the vertical velocity graident are in agreement with previously reported values from Hα studies of 18.8 $\pm$ 6.3 km s^{-1} kpc^{-1} (Kamphuis et al. (2007)) and 15-18 km s^{-1} kpc^{-1} (Heald et al. (2006)). These studies used envelope tracing and modeling to determine the value of the lag. Rand (1997) found a value of 8.6 km s^{-1} kpc^{-1}, but his results are strictly from centroid fitting, which we found (at least for our observing setup) underestimates the actual vertical velocity gradient (see §3.5.4 for a detailed discussion).

Swaters et al. (1997) measured a vertical velocity gradient of 20 km s^{-1} kpc^{-1}, and Fraternali et al. (2005) and Oosterloo et al. (2007) both measured gradients of 15 km s^{-1} kpc^{-1}. These three studies used HI observations and modeling. It is interesting to note that the gradients measured from HI and Hα data are consistent with each other. This indicates that the ionized and neutral hydrogen gas could share a similar origin or that they respond similarly to processes that control lag.

3.5.3. NGC 4631 Velocity Profiles

The velocity profiles of the east field of NGC 4631 are shown in Figure 3.15. We see no lagging component in the extra planar gas in the upper or lower halves, but there is a significant difference in velocity between the two halves. The velocities in the north half ($\sim$740 km s^{-1}) are expected, based on the systemic (606 km s^{-1}) and rotational ($\sim$140 km s^{-1}) velocities of the galaxy.

The velocities on the south side of the field are as much as 100 km s^{-1} lower than the north side in several of the slits, and these are the slits that cover large, extended circular feature that is prominent in optical imaging on the east side of the galaxy (see Figure 3.2). Golla et al. (1996) first observed that the southern half of this feature had significantly lower velocities than the northern half. Rand & Stone (1996) modeled this region of NGC 4631 as the result of an impact from a high velocity cloud.

Alternatively, the drastic decrease in velocity can be explained by the southern half being a spiral arm segment along our line of sight that is warped downward, below the midplane. The average velocity of the gas in the northern half of

the field in slits 6-10, which show this velocity discrepancy between the north and south sides, at distances of 0.5 kpc or greater from the midplane is 730.0 km s^{-1}. Allowing for projection effects of a disk that has an inclination of 85°, the average intrinsic rotational velocity of this gas is 732.8 km s^{-1}. If we assume the gas on the south side has the same intrinsic rotation velocity, then we can calculate the angle at which the southern half of the extended circular feater is warped out of our line of sight. The average velocity in slits 6-10 for gas that is 0.5 kpc or greater from the midplane on the south side of the field is 666.3 km s^{-1}. The southern, near side of the feature would need to have an inclination of 65.4°, compared to the 85° inclination of the northern, far side, to explain the difference in velocities. NGC 4631 is known to be an interacting galaxy, and a heavily warped disk on the east side could be the result of interactions with smaller companion galaxies.

In slit 9 in the east field, we see line line-splitting near the midplane, and we see line broadening at the points just above and below that. These measurements are at the transition between the main part of the disk and the warped spiral arm, and the line-splitting is most likely the result of measuring gas from each of these components of the disk along the same line of sight.

The velocity profiles for the central field of NGC 4631, which are shown in Figures 3.16 – 3.18 with two sets of model profiles overlaid, show emission at least 2-3 kpc from the midplane across the entire field. Slits 1-3 are on the receding half of the galaxy, and none of their velocity profiles shows an obvious lagging component, which would appear as a 'greater than' sign. The emission in the lower half of slit 1 is dominated by four Hα patches, the lower three of which are easily seen in the gray scale spectrum (Figure 3.7) and the Hα image with the slit positions overlaid (Figure 3.2). The fourth Hα patch is close to the midplane

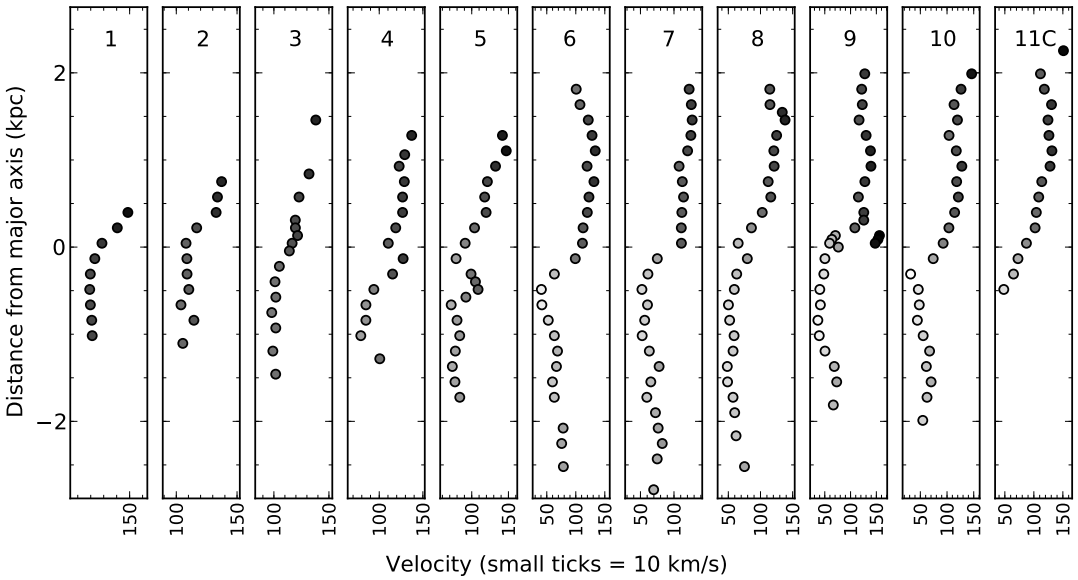

Fig. 3.15.— Velocity profiles for the east (receding) field of NGC 4631. We do not observe a lagging component in the EP gas, but our profiles show that the northern and southern halves of the galaxy are kinematically distinct. Slits 6-10 show a significant decrease in velocity at negative distances from the midplane. This can be explained by a warped disk with an inclination of 65.4°on the near side and an inclination of 85.0°on the far side. Line splitting near the midplane of slit 9 is likely due to gas from the near and far sides of the disk (at their respective inclinations) being superposed along the line of sight.

and blends with the brighter emission, and it has a velocity of ∼645 km s^{-1}. The other three Hα patches have velocities close to systemic, which is ∼90 km s^{-1} lower than the velocities of the emission in the upper half of the slit. These patches appear to be isolated, but it is hard to determine if this is the case based on their kinematics because of their proximity in velocity space to the sky line doublet at 6577.28 Å. Remnants of that line after sky line subtraction might be mistaken for Hα emission connecting the patches and would have a velocity of 662.1 km s^{-1}, which would explain the sawtooth pattern in the velocity profile. It is also possible there is faint Hα emission with similar velocities to the gas in the upper part of the slit, and this could also explain the sawtooth pattern. This slit

lies right next to our east field, which is extremely warped in the lower half and was likely interacting with companion galaxies in the recent past, so it is possible that there could be isolated pockets of Hα-emitting gas.

The upper half of slit 2 and the upper and lower halves of slit 3 show a slight increase in velocity with distance from the midplane. Since these slits are on the receding half of the galaxy, increasing velocities signify EP gas that is rotating faster than the disk. The profile of slit 3 is very similar to that of slit 4, which is on the approaching half of the galaxy, and slits 4 and 5 show a strong decrease in velocity with distance from the midplane in addition to gas that goes past systemic. The behavior of the gas in these four slits can be explained by gas that is flowing outward from the galaxy, away from the observer. In the receding half, this outflow would add to the observed rotational velocity, resulting in velocity profiles that mimic an accelerating EP component. On the approaching half, an outflow would be in the opposite direction to the rotational velocity, producing an extreme lag, possibly to the point of showing gas that has velocities that are greater than systemic velocity. Slits 6, 7, and possibly 8 also show very strong lags, which could be due to the outflowing gas.

Slits 9-11 show the signature of an EP lagging component, but it is less drastic than slits 5-8. There could be a small amount of outflow at these slit locations, but these profiles could also be explained by lagging gas from fountain flows instead of a massive outflow event.

All the slits on the approaching half of this field show localized peaks near the midplane, similar to NGC 891. This can be attributed to dust in most of the slits, but slits 9-11 show increased velocities over a wider area around the midplane.

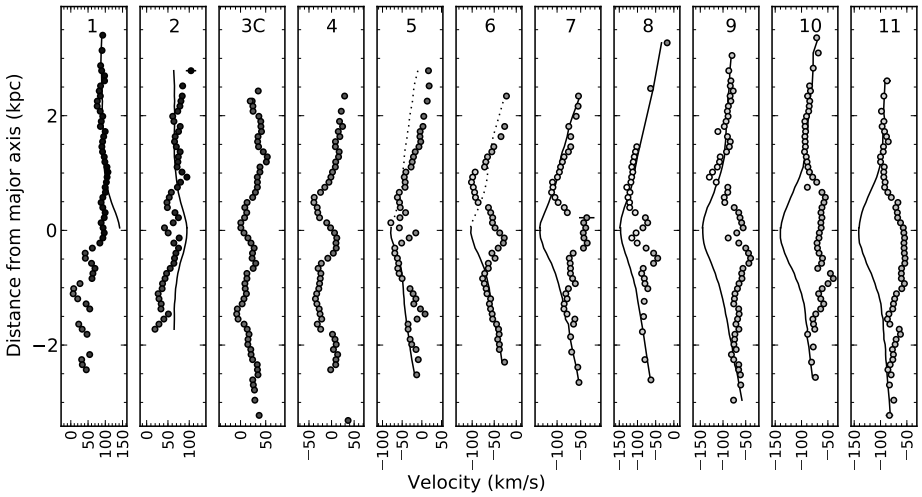

Fig. 3.16.— 85° model profiles for the NGC 4631 central field. Velocities from the data (circles) are overlaid with model profiles (solid lines) from a disk inclined at 85°. The lower half of slit 1 appears to be isolated patches of Hα emission, which we cannot fit with our models. We also do not model the profiles of slit 3, which is close to the galaxy's center, or slit 4, which has a lot of dust attenuation in the lower half and bright HII regions in the upper half. The dotted lines in the top panel on the upper halves of slits 5 and 6 show model profiles with lags of 200 km s^{-1} kpc^{-1}. This is still not a sufficient lag to fit the data, so we could be seeing an outflow region. The values of the best-fit lag for the upper and lower halves of the slits that we can model are shown in Figure 3.17.

The emission from these slits is very bright, and Figure 3.2 shows that those three slits cross large clumps of emission. It could be that these bright clumps are in a spiral arm which is preventing us from observing gas at the maximum tangential velocity. If so, we are only measuring a fraction of their circular velocity. On the approaching side of a galaxy, this would result in less blue-shifted velocities, which can explain the velocity profiles we see in slits 9-11. We discuss this more in §3.5.5.

The west field of NGC 4631 (see Figures 3.16 and 3.18) shows emission up to 2 kpc in several of the slits on the eastern side of the field, but the extent of the

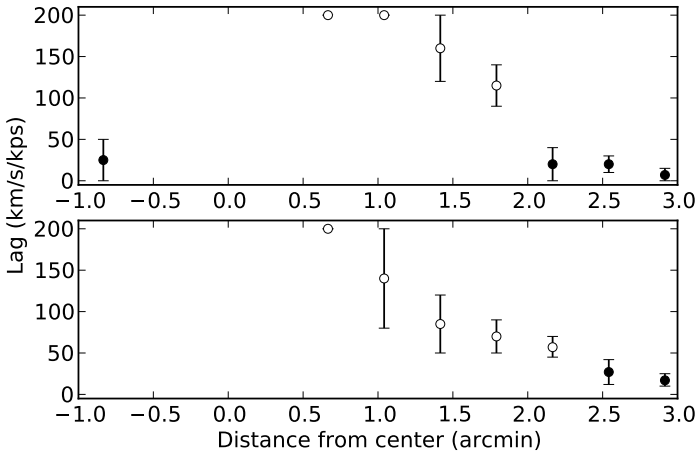

Fig. 3.17.— Lag for the 85° models of the central field of NGC 4631. The upper and lower panels show lag values as a function of radius for above and below the midplane, respectively. Open circles indicate values that constitute an extreme lag. These models show a constant or decreasing lag in the outer slits.

observed emission drops toward the western side of the field, which is at the edge of the optical radius of the disk. The velocity profiles for all of the slits have a similar pattern. They show a slight lagging component, and the magnitude of the lag appears fairly constant across the field. A few of the profiles have a peak near the midplane, which we attribute to dust obscuration preventing us from seeing to the tangential point, as was discussed for the central field.

3.5.4. NGC 4631 Model Profiles

Since a disk that is close to but not exactly edge-on can produce velocity profiles that mimic a lagging component even when there is no lagging gas, we modeled the central and west fields of NGC 4631 with inclinations of 85° and 90°. For each inclination, we generated models with a wide range of lags, and we fit the upper and lower half of each slit separately. This allows for a radially varying lag

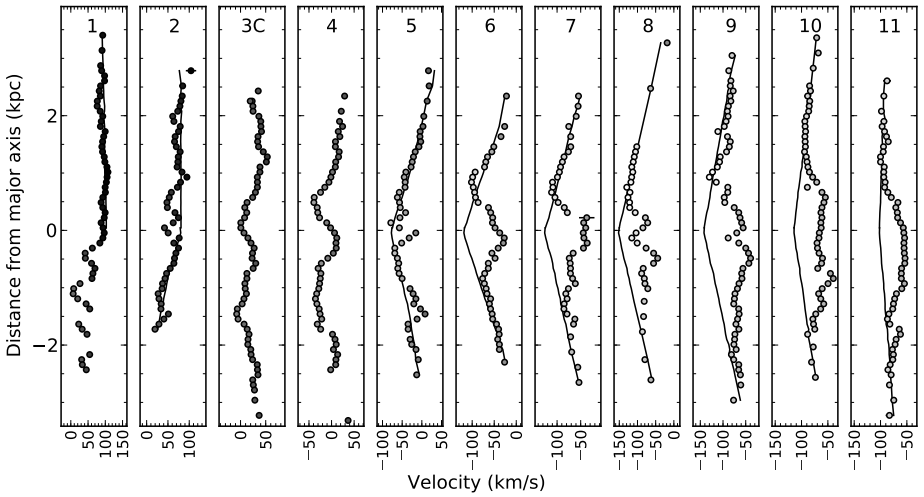

Fig. 3.18.— 90° model profiles for the NGC 4631 central field. Velocities from the data (circles) are overlaid with model profiles (solid lines) from a disk inclined at 90°. The values of the best-fit lag for the upper and lower halves of the slits that we can model are shown in Figure 3.19.

which can be different for the upper and lower halves of the field. Similar to NGC 891, we allowed the model profiles to shift horizontally in wavelength space when matching them to the data. The only requirement was that the midplane velocities from the upper and lower half of each slit were consistent with each other. Since the east field shows very disturbed kinematics that cannot be modeled by a simple rotating disk with lagging gas, we did not model that field.

The modeling results for the central field are shown in Figures 3.16 and 3.18. The data are overplotted with model velocities for models at both inclinations. We did not include model profiles for slits 3 or 4 at either inclination. The proximity of slit 3 to the center of the galaxy means most of the gas is moving perpendicular to our line of sight, so a disk with no lagging gas and a disk with highly lagging gas both produce profiles with almost constant velocity.

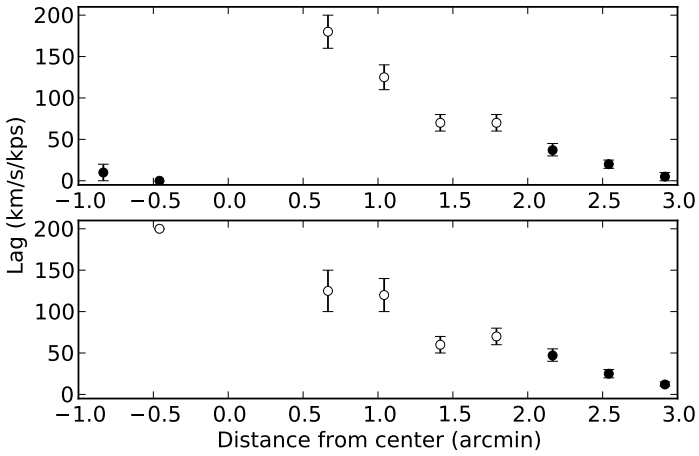

Fig. 3.19.— Lag for the 90° models of the central field of NGC 4631. The upper and lower panels show lag values as a function of radius for above and below the midplane, respectively. Open circles indicate values that constitute an extreme lag. These models show a radially decreasing lag in the outer three slits.

Slit 4 shows an irregular, assymetrical profile that could not be fit by any of our models. The gray scale spectrum and the Hα image with the slits overlaid both indicate that slit 4 crosses a bright HII region just above the midplane and has severe dust absorption below the midplane. Both of these prevent us from seeing the actual rotational velocity of the gas, and our simple models are unable to fit the data.

The dotted lines shown with the data in slits 5 and 6 are for models with lags of 200 km s^{-1} kpc^{-1}, and this is not sufficient to match the steepness of the data profile. Extreme lags are not likely scenarios for EP gas that is rotating within a thick disk, so we do not consider models with lags greater than 200 km s^{-1} kpc^{-1} to be realistic. With such high lags, the gas would slow to systemic velocity at a distance of less than 1 kpc from the midplane. As we mentioned earlier, a more plausible explanation is a central area of outflowing gas.

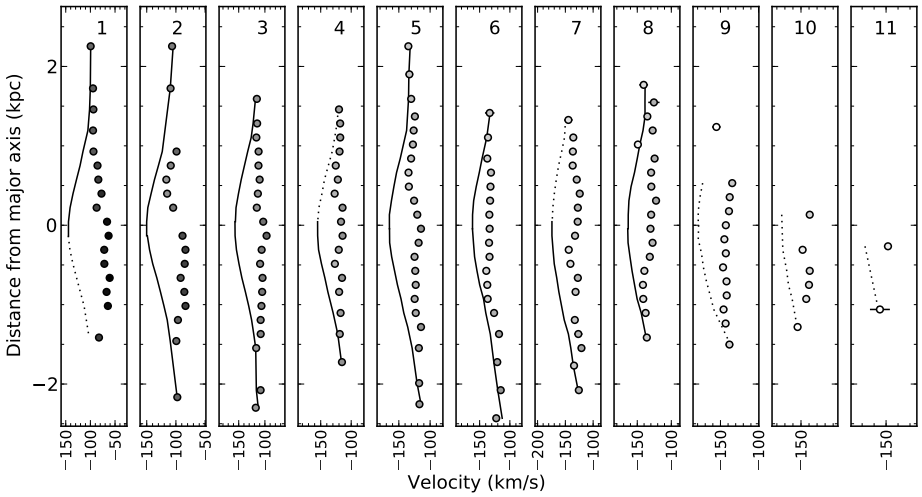

Fig. 3.20.— 85° model profiles for NGC 4631 west. The data are shown as open circles, and the solid lines are the model profiles. The dotted lines are profiles from models with no lag, and we do not try to fit the data because there is a lack of data points sufficiently far from the midplane. The values of the best-fit lag for the upper and lower halves are shown in Figure 3.21.

For the remaining slits, the models with inclinations of 85° and 90° appear to fit the data equally well, and it is possible that the inclination of the disk fluctuates within that 5° range across the field. The values of the model lags for each slit are shown in Figures 3.17 – 3.19. Both sets of models show a similar pattern.

The upper half of the 85° models shows a lag of 25 km s^{-1} kpc^{-1} for slit 1. We have no measured lags for the lower half of slit 1 or slits 2-4. Slits 5-8 and the bottom of slit 9 show extremely high lags, but given the rotation curve of NGC 4631 and the extent to which we see emission, this would result in gas at forbidden velocities. This is not possible solely with the galactic fountain scenario. There must be another process which is causing the gas to move away from the observer, either in addition to or instead of a lagging component from the galactic fountain.

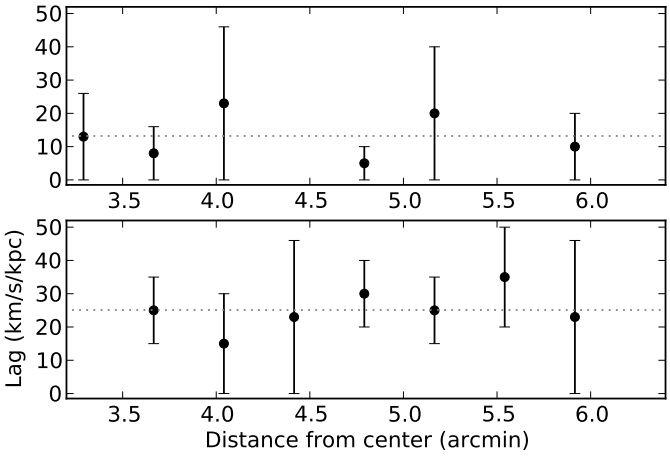

Fig. 3.21.— Lag for the 85° models of NGC 4631 west. The upper and lower panels show lag values as a function of radius for above and below the disk, respectively. The upper half of the field can be fit by a lag of 13.2 ± 7 km s^{-1} kpc^{-1}, and the lower half can be fit by a lag of 25.1 ± 6.2 km s^{-1} kpc^{-1}.

There could be accretion of low angular momentum material, but outflows are more likely because of the active star formation in this region. Slits 9 – 11 show a moderate lag that decreases with radius, but with the large error bars, a constant value of 10-15 km s^{-1} kpc^{-1} for the upper half and 12-15 km s^{-1} kpc^{-1} for the lower half also fit the data.

Model lags for the 90° models show a similar trend to the 85° models. The upper half of slit 1 has a lag of 10^{+10}_{-10} km s^{-1} kpc^{-1}, and the upper half of slit 2 shows either no lag or gas that increases with distance from the major axis. The lower half of slit 2 and slits 5 – 8 show extreme lags. Similar to the 85° models, this indicates that there are outflows in this region. Slits 9-11 show a decrease in lag with radius in the upper and lower halves.

Both sets of models show a large discrepancy between the model profiles and the observed profiles near the midplane in slits 9-11. We see less dust extinction in

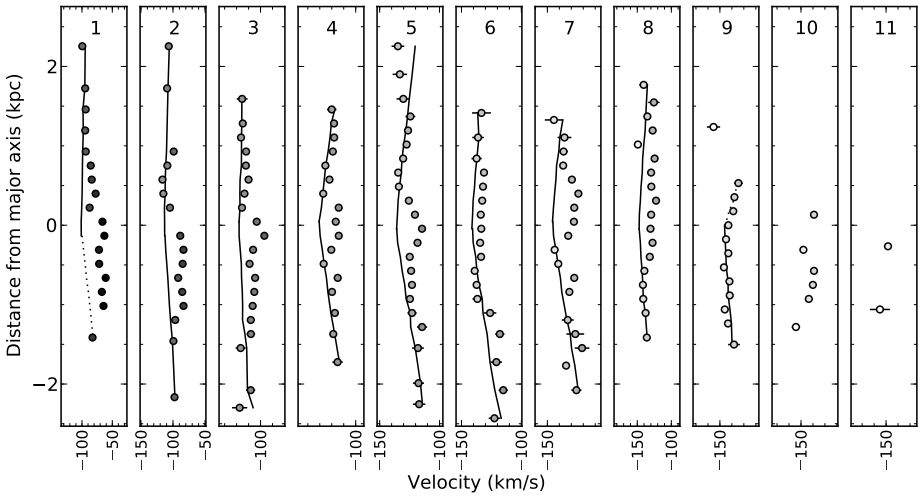

Fig. 3.22.— 90° model profiles for NGC 4631 west. The data are shown as open circles, and the solid lines are the model profiles. The dotted lines are profiles from models with no lag, and we do not try to fit the data because there is a lack of data points sufficiently far from the midplane. The dashed lines in slits 10 and 11 show the average velocities of the data in those slits. We do not model those data, but we adopt the average velocity as the midplane velocity for those slits. The values of the best-fit lag for the upper and lower halves are shown in Figure 3.23.

those slits than in the slits closer to the galaxy center, so the pattern we see in the data is likely from bright HII regions that prevent us from seeing emission along the entire line of sight. Our models assume a transparent disk with a smooth density distribution, so they reach maximum velocities near the midplane.

It is important to note that the model profiles for slits 5-8 at both inclinations could only be matched to the data when the gas in the models was allowed to decrease in velocity to the point of rotating in the opposite direction of the disk. Allowing gas to rotate at forbidden velocities in this way is not a physical solution from a pure fountain flow, but outflows or accretion could cause this.

Modeling results for the west field of NGC 4631 are shown in Figures 3.20

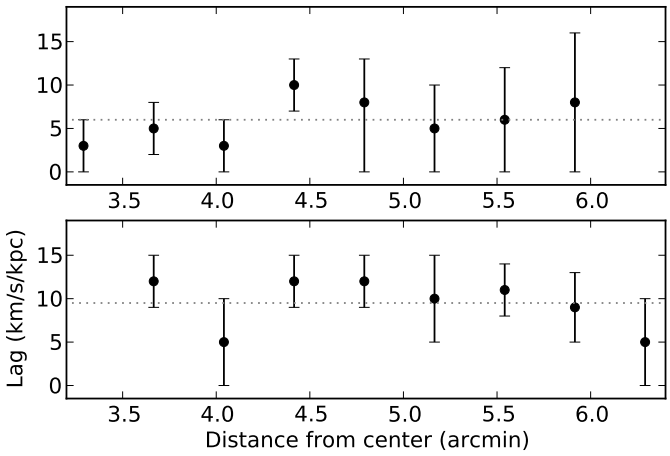

Fig. 3.23.— Lag for the 90° models of NGC 4631 west. The upper and lower panels show lag values as a function of radius for above and below the disk, respectively. The upper half of the field can be fit by a lag of 6.0 ± 2.5 km s^{-1} kpc^{-1}, and the lower half can be fit by a lag of 9.5 ± 3.0 km s^{-1} kpc^{-1}.

and 3.22. Most of the slits for the 85° models show the same spatially extended discrepancy between observed and model velocities near the midplane. Similar to slits 9-11 in the central field, the data do not show significant exinction due to dust, and most slits in this field cross bright regions of patchy Hα emission near the midplane.

The dotted lines for the 85° models in Figure 3.20 show results for models with no lag, but we do not detect emission far enough from the midplane to determine if the gas is lagging. At distances of ∼1.5 kpc and less from the midplane, models with no lag and models with a large lag produce very similar velocity profiles. For the 90° models, there is only one data point in the lower half of slit 1 that we can assume is not severely affected by dust extinction, so our best fit model is unreliable. In the upper half of slit 9, we can only fit models to the data points that are within 0.5 kpc from the midplane. Since the points are so close to the

midplane, we exclude that lag value from our results.

The values of the lag for the slits that we can model are shown as a function of radius in Figures 3.21 – 3.23. The lags for both models are fairly constant. The 85° models indicate lags of 13.2 ± 7 km s^{-1} kpc^{-1} in the upper half and 25.1 ± 6.2 km s^{-1} kpc^{-1} in the lower half. The 90° models indicate lags of 6.0 ± 2.5 km s^{-1} kpc^{-1} and 9.5 ± 3.0 km s^{-1} kpc^{-1} in the upper and lower halves, respectively.

In general, the lag values for the 90° models have smaller error bars than the 85° models. This is because a non-edge on disk produces velocity profiles that mimic a lag, and the inclination effects are more dominant than the lagging gas in determining the shape of the velocity profiles. A highly inclined, but not quite edge-on, disk causes bright midplane gas to be superposed over fainter EP gas, so the lagging gas has a small effect on the observed velocities. This results in a wide range of lags producing similar velocity profiles. This is not the case for the 90° models, so they have a smaller range of possible lags that are acceptable fits to the data.

Another result from our models, which is more readily seen in the NGC 4631 models because of the large lags than in the NGC 891 models, is that our centroid velocities underestimate the value of a lagging component. A line of sight through an edge-on disk crosses a large range of galactocentric radii. At the tangential point along that line of sight, we measure the full component of the rotational velocity. At all points in front of and behind the tangential point, only a portion of the rotational velocity is along our line of sight. If we use the receding side of a galaxy as an example, this produces an intrinsic emission profile with a peak at the rotational velocity and a low velocity tail (see Kregel & van der Kruit

(2004) and Matthews & Wood (2001) for further discussion of observed velocities and rotation curves in edge-on galaxies). When this profile is convolved with the telescope response function, the result is an emission profile with a peak at a lower velocity than the actual rotational velocity. Fitting a gaussian to the convolved profile exaggerates this, so the velocity is underestimated even more.

In edge-on systems with a lag, the amount by which the velocity is underestimated decreases as you move above the disk. This is due to a change in the range of velocities that the line of sight passes through. Starting in the midplane of a disk with, e.g., a flat rotation curve of 100 km s^{-1}, the maximum velocity observed is 100 km s^{-1} at the tangential point of the line of sight. The minimum observed velocity occurs at the points where the line of sight crosses the optical edge of the disk. If our line of sight is at some distance from the center of the galaxy so that the minimum observed velocity is 50% of the rotational velocity (i.e., the direction of the rotation forms a 60° angle with our line of sight), then the minimum observed velocity is 50 km s^{-1}, and the velocity range of the intrinsic profile is 50 km s^{-1}. If we assume a lag of 30 km s^{-1} and a distance of 2 kpc above the midplane, then the rotational velocity drops to 40 km s^{-1}. This means the maximum observed velocity is 40 km s^{-1}, the minimum is 20 km s^{-1}, and the range of observed velocities is 20 km s^{-1}. Because the width of the low velocity tail decreases with distance above the midplane, the velocity is understimated less as we move above the plane. Since there is a large underestimate in the midplane and a smaller underestimate above the midplane, the lag indicated by our centroid measurements is less than the intrinsic lag of the EP gas.

The EP gas in the models of the central field of NGC 4631 is required in the models to decrease in velocity with distance from the midplane to the extent that it

appears to be counter-rotating with respect to the plane. On the approaching side of this field, the velocity profiles have a high velocity tail which biases the centroid measurements. At the point at which the model gas decreases to systemic velocity and begins to rotate backward, the high velocity tail becomes a low velocity tail. The centroid velocities at that point and farther from the midplane are lower than the intrinsic rotational velocity, so the velocities of the gas at the edges of slits 5-9 are closer to the systemic velocity than indicated by the centroid velocities.

The fact that our model centroids underestimate the lag is partly a result of the fact that our models assume a transparent disk. This effect is different from the observational effect described by Kamphuis et al. (2007), which produces the same result of underestimating the vertical velocity gradient. In the midplane, the observer often cannot see through the disk to the tangential point of the disk, so the rotational velocity is underestimated. As distance from the midplane increases, optical depth decreases (assuming a given scale height), which means the observer can see further into the galaxy and is most likely able to see the tangential point. The rotational velocity is underestimated less than it is in the disk, if at all.

3.5.5. NGC 4631 Midplane Velocities

Hα midplane model velocities for the central and west fields of NGC 4631 are overplotted on an HI position-velocity (PV) diagram in Figure 3.24. For the east field, we plotted velocities from from the northern half of the field at distances of +0.5 kpc and +1.0 kpc from the midplane as an approximation of model velocities close to the midplane. The gas at those distances is in the 85°-inclined disk instead

of the warped near side of the disk. For this diagram of NGC 4631, we expect the midplane velocities to follow the 3rd or 4th contour line at offsets of $\pm 1'$ and farther from the minor axis. From $-1'$ to $+1'$, the rotation curve is likely rising steeply in an almost linear fashion.

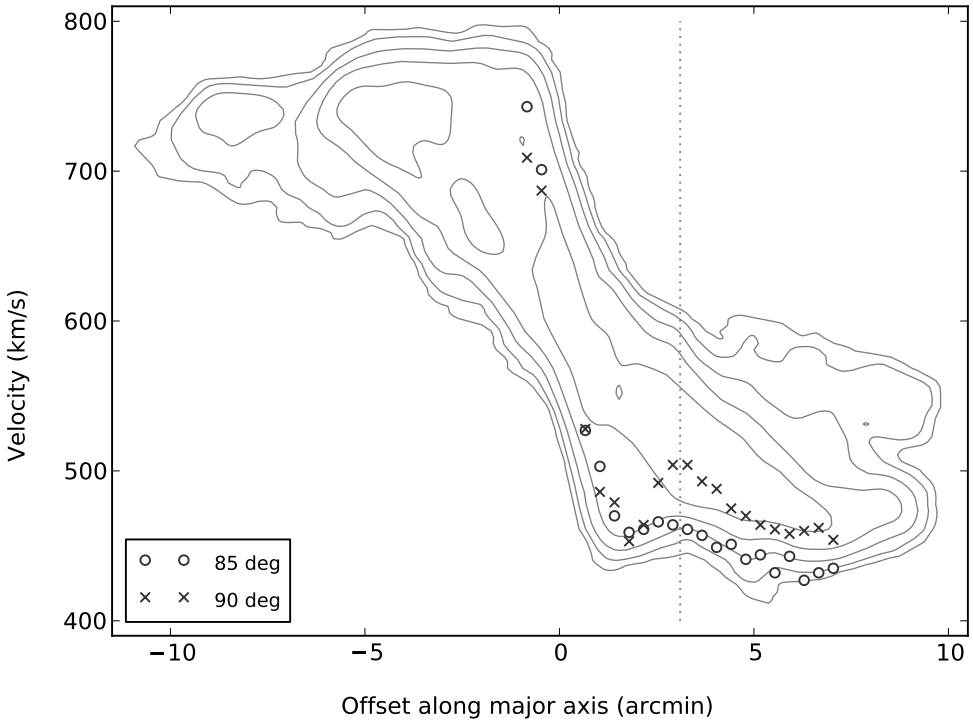

Fig. 3.24.— Hα and HI midplane velocity comparison for NGC 4631. Model midplane Hα velocities are overlaid on an HI PV diagram. The HI data is from a 10x12 hr exposure with the Westerbork Synthesis Radio Telescope, courtesy of the HALOGAS group (Heald et al. 2011), with a beam size of $45.0'' \times 39.1''$. Contours start at 2σ and increase by factors of 3. Model midplane velocities from the 85° and 90° models are shown for the central and west fields, which are separated by a dotted line.

The midplane velocities from the model profiles indicate that the 85° models produce better fits for most of the central field. Slits 10 and 11 in the central

field and slits 1-3 in the west field show a large discrepancy between the midplane velocities for the 85° and 90° models. An intermediate inclination between 85° and 90° is probably most likely for those slit locations. Midplane velocities indicate that an inclination close to 90° is a good fit for slits 4 – 11 in the west field.

Using our best-guess inclination for each slit based on midplane velocities and comparing the velocity profiles from the data and models, we can determine that the discrepancy between the observed velocity and the expected rotational velocity is fairly large in the central field at slit 9 ($\sim$90 km s^{-1}) and steadily decreases to the west field at slit 5 ($\sim$40 km s^{-1}). We mentioned previously that bright HII regions along our line of sight could cause this. The fact that the discrepency is very large at a radius of 2.166′ and decreases almost linearly to a radius of 4.791′means we could be observing HII regions along the leading edge of a spiral arm. If this spiral arm lies in front of the node of the galaxy that is prependicular to our line of sight, then we would observe decreased velocities. The point at which the curved arm is farthest from the tangential point is the point at which we would see the greatest discrepancy. Beyond 2.166′, if the spiral arm curves back toward the tangential node, then we would observe a larger and larger component of the full rotational velocity of the HII regions as radius increases. This would cause the discrepancy between the observed and expected rotational velocities to decrease, which explains the behavior of the profiles in the west field.

3.5.6. NGC 4631 Line Widths

In addition to the kinematics of the central field indicating possible outflows in slits 2-8, there is also evidence for outflows in the line widths of these profiles.

Figure 3.25 shows the ratio of observed line widths to model line widths. Line width ratios greater than 1 indicate line broadening in excess of broadening due to rotation. Ratios in the $\sim$1.0 – 1.5 range can be due to turbulence in the gas, deviations from circular rotation, or deviations from the rotation curve that is assumed as input for the models. Larger ratios than this are likely best explained by outflowing gas, because outflow would greatly increase the range of observed velocities along our edge-on line of sight and result in wider emission profiles.

If the outflowing gas is in the form of a cone, emission from the near and far sides of the expanding cone will cause profile splitting, assuming the velocity resolution is sufficient. Axon & Taylor (1978) were the first to realize that line splitting in their spectra of M82 was likely caused by an expanding bubble of gas. Heckman et al. (1990) also observed line splitting in M82, as well as in NGC 253 and NGC 4945. In all three galaxies, the line splitting occured over an area several kiloparsecs wide near the galaxy's nucleus. Episodes of nuclear starburst can create large associations of OB stars, which result in stellar winds and supernovae that drive gas outflows. We do not see line splitting in our profiles, but NGC 4631 appears to be a very active galaxy. It is possible that there are mutliple outflow cones interacting with each other, and this would further complicate the kinematics.

Figure 3.25 highlights the points where the ratios of observed to model line widths are 2.0 or greater, indicating possible areas of strong outflows. Most of these points have intrinsic line widths of $\sim$140 km s^{-1} or greater. Golla et al. (1996) took a long-slit spectrum perpendicular to major axis very close to the location of our slit 2. They found intrinsic widths of $\sim$100-140 km s^{-1} along the slit, which agree well with our line widths.

Slits 2 – 7 show significant broadening at the tops and bottoms of the slits (with the exception of the bottom of slit 5). Slits 8 and 9 also show some broadening. The spatial extent of slits 2-7 ranges from 1.01 kpc east of the galaxy's center to 3.13 kpc west of the galaxy's center. The location of this possible outflow is consistent with previous studies by Rand et al. (1992) and Strickland et al. (2004a), who found evidence for nuclear outflows in the form of vertical Hα filaments extending upward from the nucleus. These filaments are likely from a central starburst that created a large bubble of hot gas. As the bubble expanded, it swept up surrounding material into a thin shell. This shell then broke through the gas layer, becoming a double-walled chimney of ionized gas (Tomisaka & Ikeuchi 1988, Heckman et al. 1990). Strickland et al. (2004b) also observed bright, extended diffuse x-ray emission above the central $\sim$4 kpc of NGC 4631. This type of emission is often generated by hot gas from SNe, so the fact that there is extensive diffuse x-ray emission implies a large number of SNe, which supports an outflow scenario.

Irwin et al. (2011) identified five anomalous velocity CO features, which are marked by small circles in Figure 3.2. These features show characteristics that are consistent with expanding shells of molecular gas. One of the features overlaps with a previously identified area of molecular outflow by Rand (2000a), and four of the features overlap with the section of our central multi-slit field whose kinematics and line widths indicate outflowing Hα gas.

Line width ratios for the west field are shown in Figure 3.26. Slits 1 and 2 show slightly more broadening than the rest of the field. The average intrinsic width of points in those slits is 65.3 km s^{-1}, whereas the average for slits 3-11 is 45.8 km s^{-1}. Golla et al. (1996) had data from a long slit spectrum of the EP gas

in N4631 at a distance of $\sim$4.4$'$ west of center, which is between slits 4 and 5 in our field. They found intrinsic line widths of $\sim$50 km s^{-1}, and our widths are in agreement.

In the west and central fields, points with line width ratios less than 1.0 are likely areas of patchy emission or areas with bright HII regions along the line of sight. Both of these scenarios result in emission observed at a smaller range of velocities than is seen in the models, which assume a smooth density distribution and a transparent disk. Slits 6-11 in the central field have very small line width ratios near the midplane, and they also show a large discrepancy between the observed and expected velocities near the midplane in Figures 3.16 – 3.18. The small line width ratios are additional indicators that dust or bright HII regions along the line of sight are obscuring our view through the disk.

Our east field line widths are shown in Figure 3.27. We did not model this field, so instead of taking the ratio of observed to model line widths, we divided each east field line width by the average of the observed west field line widths. The east and west fields both lie on the non-rapidly rising part of the rotation curve, so the profiles will have similar amounts of line broadening from rotation. Dividing by the average west field width also approximates a deconvolution of the profiles so we can remove the broadening effects from the telescope response function and compare the line width ratios to that of the central and west fields.

We see excess broadening in slits 10 and 11, which lie on either side of one of the molecular outflow features identified by Irwin et al. (2011). Slit 9 shows line splitting near the midplane but not much broadening elsewhere along the slit. As mentioned earlier, we believe that this line splitting occurs because our line of

sight near the midplane goes through the warped near side of the galaxy and the almost edge-on far side of the galaxy. We do not believe it is from an outflow. There are a few points just below the midplane in slit 7 with wider profiles, but the rest of the field shows little excess broadening.

3.6. Conclusions

We have presented multi-long-slit observations and modeling of the EP gas in edge-on galaxies NGC 891 and NGC 4631. Our observing setup allows us to study the kinematics of the ionized gas, and our models help us interpret our spectral profiles, which are affected by the fact that we are observing edge-on disks.

NGC 891 shows extensive Hα emission up to 4 kpc from the midplane. We measured a vertical velocity gradient of 19^{+7}_{-4} km s^{-1} kpc^{-1} in the northwest quadrant and a gradient of 15^{+12}_{-2} km s^{-1} kpc^{-1} in the northeast quadrant. These values are in agreement with previous studies of the lagging gas in NGC 891 (Kamphuis et al. 2007; Heald et al. 2006; Swaters et al. 1997; Fraternali et al. 2005; Oosterloo et al. 2007), and we used this galaxy as a test galaxy for our observing setup and models.

We observed three fields in NGC 4631. The east field appears to contain a large, extended circular feature with a diameter of $\sim$5 kpc. The gas in the northern half of this feature has velocities that are consistent with the rotational velocities of the rest of the galaxy. The gas in the southern half, however, is rotating up to 100 km s^{-1}slower. Based on the kinematics, we conclude that the lower part of the disk is a spiral arm that is warped downward out of our line of sight, with an inclination of $\sim$65°. NGC 4631 shows signs of interacting and has

several companion galaxies, and a close interaction with one of those companions could have caused a sharp bend in the disk.

The central field of NGC 4631 shows an apparent extreme velocity lag near the inner part of the galaxy. The line profiles are also broadened significantly, and we see gas at forbidden velocities in some of the slits. All of these indicate a large gas outflow, with a spatial extent of $\sim$1 kpc east of the galaxy's center to $\sim$4 kpc west of the center. The proximity to the minor axis is consistent with a central disk starburst creating a large assocation of OB stars, which can cause outflows via stellar winds and supernovae. We detect a smaller-magnitude lag in the outer part of this field, ranging from 10 to $\sim$50 km s^{-1} kpc^{-1}. There is a small likelihood that the value of the lag decreases with radius, but the lag could also be constant within our errorbars.

We measure a constant lag in western field of NGC 4631. This field is best modeled with a lag of 6.0 $\pm$ 2.5 km s^{-1} kpc^{-1} in the northwest quadrant and a lag of 9.5 $\pm$ 3.0 km s^{-1} kpc^{-1}in the southwest.

Based on our models, the inclination of NGC 4631 appears to be $\sim$85° in the central part of the galaxy and smoothly transitions to 90° at a distance of 4.4′ (9.8 kpc) on the western side. A comparison between the observed and model velocity profiles for both of these fields indicate that near the midplane, we may be observing bright HII regions along the leading edge of a spiral arm.

Table 3.1. Observing Parameters: NGC 891 and NGC 4631

Parameter	NGC 891	NGC 4631
RA (J2000) [a]	$2^h22^m33.41^s$	$12^h42^m8.00^s$
Dec (J2000) [a]	$+42°20'56.9''$	$+32°32'29.0''$
PA (°)	22	86
v_{sys} (km s^{-1}) [a]	528	606
Hα wavelength at v_{sys} (Å)	6574.6	6576.3
Observing dates (UT)	16-17 Nov. 2009	25 Feb., 26-27 Apr. 2009 (central) 29 Apr. 2011 (east, west)
Grating (lines mm^{-1})	1200	1200
Dispersion (Å pix^{-1})	0.58	0.58
Total integration time (hrs)	12.9	0.75, 6.75, 3.0[b]
Field location[c] ($'$)	−2.00	−3.08, 1.04, 5.17[b]

[a]From NED.
[b]For the east, central, and west fields, respectively.
[c]Offset from galaxy center to slit 6, the middle of our field. Negative values indicate east of the galaxy center.

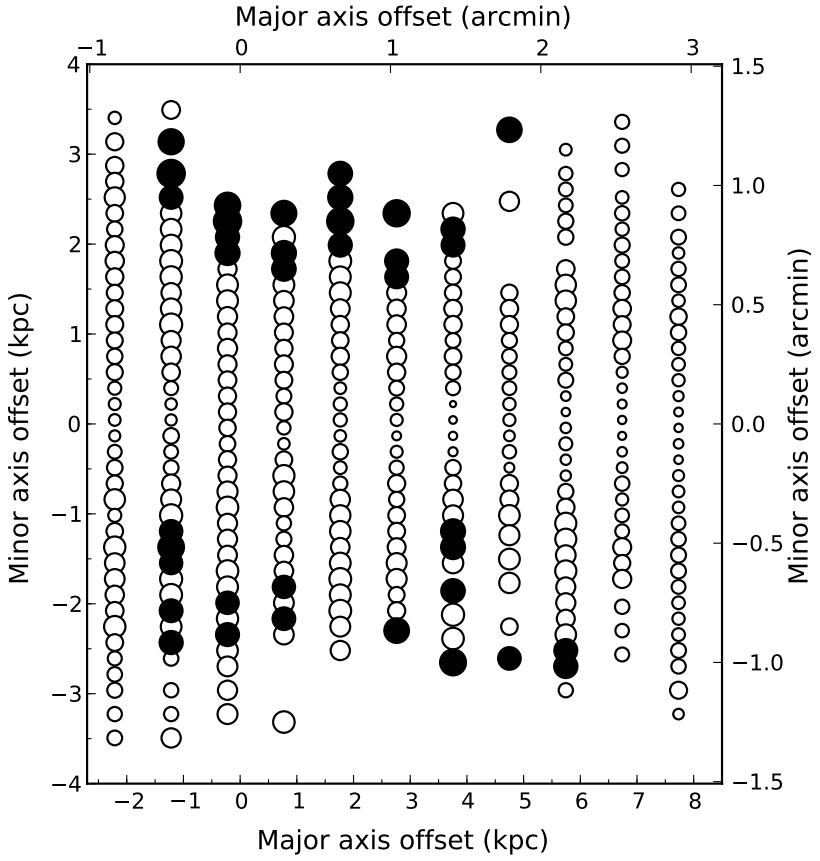

Fig. 3.25.— Ratio of observed to model line widths for the central field of NGC 4631. The model line widths are from a model inclined at 85° and with a lag of 50 km s^{-1} kpc^{-1}, which was chosen as an approximate model for the entire field. Models inclined at 90° and/or with lags of 0 or 100 km s^{-1} kpc^{-1} produce similar results. The size of each point is proportional to the ratio, and the ratios range from 0.5 to 2.5. Points with ratios of 2.0 or greater are plotted in black. These areas likely have significant outflows, which broadens the emission profiles.

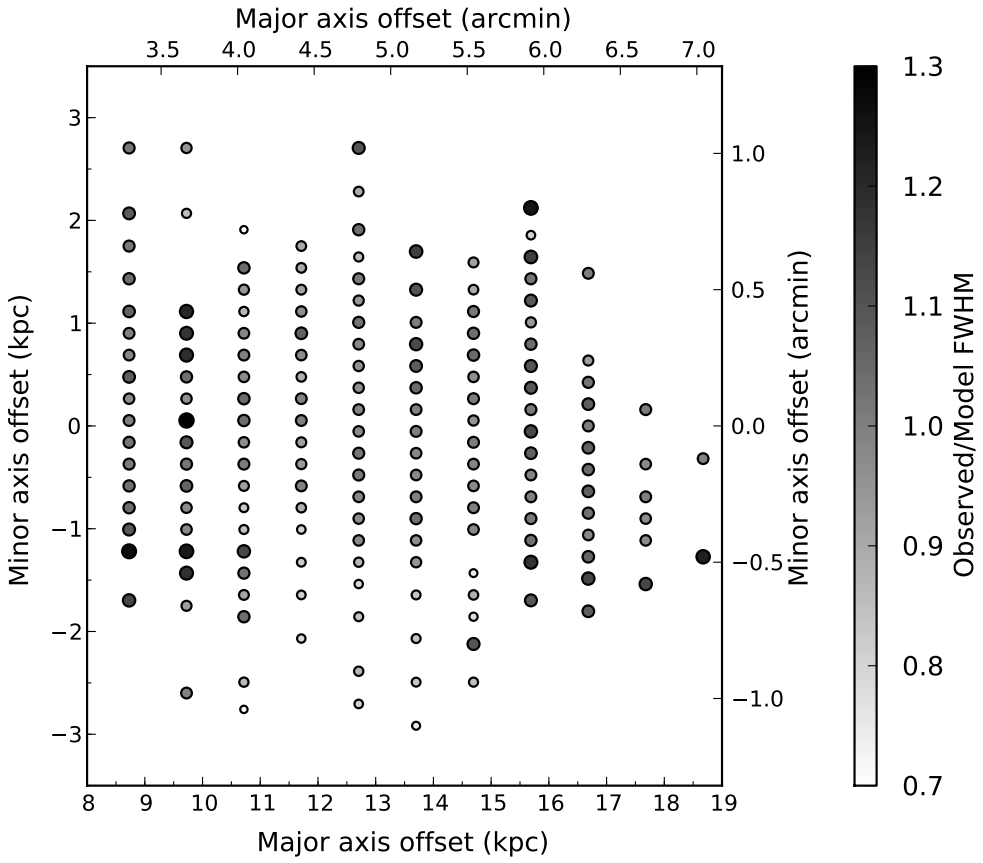

Fig. 3.26.— Ratio of observed to model line widths for the west field of NGC 4631. The model line widths are from a model inclined at 85° and with a lag of 10 km s^{-1} kpc^{-1}, which was chosen as an approximate model for the entire field. Models inclined at 90° and/or with lags of 0 or 50 km s^{-1} kpc^{-1} produce similar results. The gray scale color bar shows the value of the ratios, and the size of each point is also proportional to the ratio.

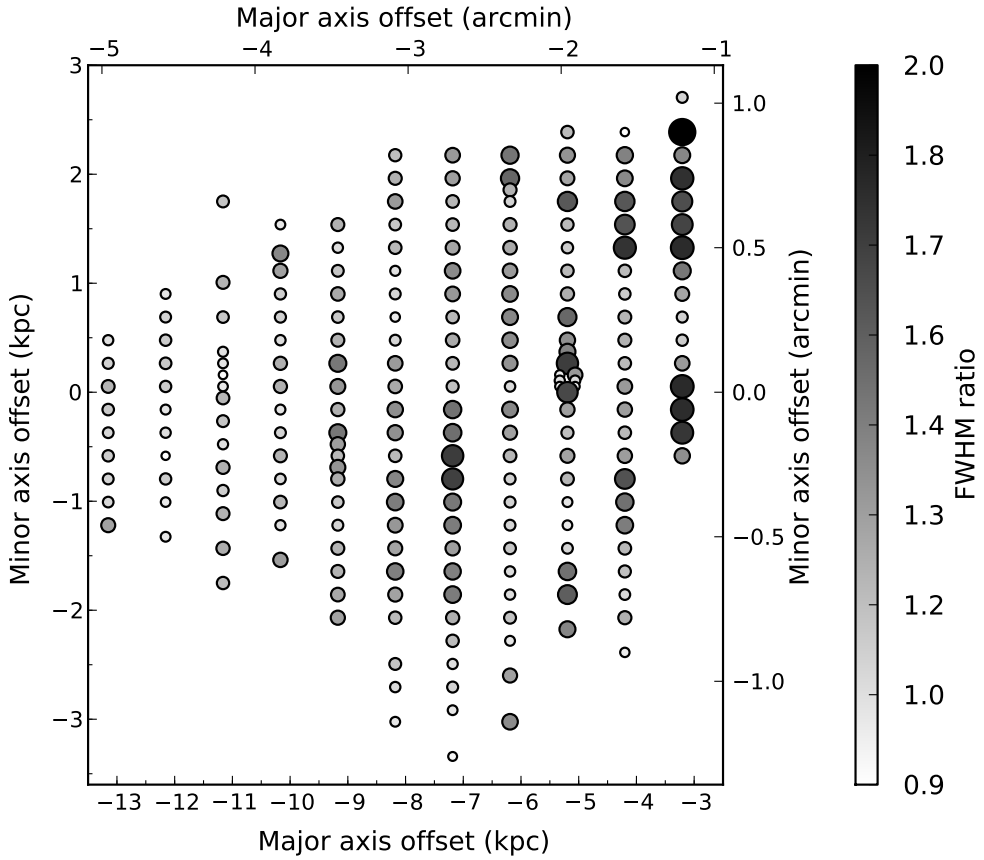

Fig. 3.27.— Line widths for the east field of NGC 4631. For each point, we divided the observed line width by the average observed line width for the west field, which shows no significant broadening. Taking this ratio is an approximation for deconvolving the observed line width. The gray scale color bar shows the width ratio, and the size of each point is also proportional to the ratio. There is some broadening in slits 10 and 11, which lie on either side of a molecular outflow feature identified by Irwin et al. (2011). Slit 9 shows line splitting, and we believe this is due to a warp in the disk rather than outflowing gas. None of the remaining slits show much excess broadening.

4. MULTI-LONG-SLIT OBSERVATIONS AND MODELING OF NGC 4517, NGC 4565, AND NGC 5907

4.1. Introduction

We present multi-long-slit spectra and modeling for NGC 4517, NGC 4565, and NGC 5907. All three galaxies have inclinations that are close to, but not exactly, edge on. Because of their inclinations and the fact that their ionized gas disks have small scale heights, their velocity profiles show inclination effects, which can mimic the pattern of a lagging component. We use our models to disentangle these effects from the kinematics of the extraplanar gas.

NGC 4517 is a large Sc spiral (de Vaucouleurs et al. 1995) with a D_{25} of $9.5'$ and a systemic velocity of 1131 km s^{-1} (Tully et al. 2009). Goudfrooij et al. (2003) measured an inclination of 87.4°. NGC 4517 is a popular target for studies of globular cluster systems (e.g. Goudfrooij et al. 2003), and it is noted for its ultraluminous X-ray source, NGC 4517 ULX1, which is situated $43''$ northwest of the galaxy's center Walton et al. (2011). Walton et al. (2011) used results from Seth et al. (2008) and Kewley et al. (2006) to determine that NGC 4517 has a high rate of star formation. There are not many optical studies or studies of the extraplanar gas for this galaxy.

NGC 4565 is classified as an Sb galaxy (de Vaucouleurs et al. 1995) with a systemic velocity of 1230 km s^{-1} (NED) and an inclination between 86.5° and 87.5° (Goudfrooij et al. 2003; Zschaechner et al. 2012; Yim et al. 2014. It is a large galaxy with an optical diameter at 25^{th} magnitude of $16.2'$ (NED), and it has a thick radio continuum disk that extends 2-3 kpc from the midplane (Broeils & Sancisi 1985; Kodilkar et al. 2008). HI observations and modeling, however, have

shown no vertically extended HI emission (Zschaechner et al. 2012, and it has low Hα emission and a very thin DIG layer (Rand et al. 1992).

NGC 4565 appears to have a box-shaped bulge, but it has been determined to be a pure disk galaxy with a bar and a pseudo-bulge (Kormendy & Barentine 2010; Combes & Sanders 1981). It is a Seyfert galaxy (Ho et al. 1997; Laine et al. 2010) with a star formation rate of 0.67 $M_\odot$ yr^{-1} (Heald et al. 2012). It has a diffuse soft X-ray halo, which is unexpected given its relatively low (for an active galaxy) SFR and could be an indication of prior starburst activity(Vogler et al. 1996). NGC 4565 also has a nuclear molecular ring that has been observed in CO at a radius of $1' - 1.5'$ (Neininger et al. 1996; Yim et al. 2014), but this area of the galaxy is outside our field of view.

NGC 5907 is a large Sc galaxy with a D_{25} diameter of $12.6'$ and a distance of 11 Mpc (Laine et al. 2010). Its inclination is between 86° and 88° (Carozzi-Meyssonnier 1978; Sasaki 1987; Rand 1996; Garcia-Burillo et al. 1997; Alton et al. 2004; Yim et al. 2014), and we adopt a value of 87°. NGC 5907 has a significant warp in its HI disk (Sancisi 1976), and its optical and stellar disks are also warped (Sasaki 1987; Morrison et al. 1994), but these warps are beyond the field of view of our observations. Because of a lack of obvious companions, NGC 5907 was thought to be a non-interacting warped galaxy until Shang et al. (1998) observed a faint ring centered around NGC 5907 that is likely a tidally disrupted dwarf companion. They also found an intact dwarf companion near the HI warp with 21 cm imaging. Martínez-Delgado et al. (2008) took deep, multi-band optical images around the area of the ring and found several arcing loops, which confirm the likelihood that this is an extended stellar tidal stream from a satellite galaxy.

Rand (1996) performed Hα-imaging of NGC 5907, but because of its inclination, they could not determine if there is diffuse Hα emission. Morrison et al. (1994) performed deep surface photometry and did not detect a thick stellar disk. Vogler et al. (1996) found no diffuse x-ray continuum halo.

4.2. Observations and Data Reduction

All of our observations were taken with the Dual Imaging Spectrograph (DIS) on the 3.5m ARC telescope at Apache Point Observatory (APO) near Sunspot, NM. Details of our instrument setup, data reduction process, and velocity measurements are described in Chapter 2. We observed one field in NGC 4517 and two fields each in NGC 4565 and NGC 5907, and we outline our observing parameters for the five fields in Table 4.1. We also observed one field in NGC 4517 with our slits parallel to the major axis to measure the rotation curve.

Our field in NGC 4517 is centered on the galaxy. We had two nights of observations for this galaxy, and sky subtraction for both nights was done by subtracting a blank sky frame. To calibrate our data, we used APO's published DIS dispersion of 0.580 Å pix^{-1} instead of measuring it from sky lines because there is only one sky line in the 658 filter that is not near the edge of the filter bandpass.

From empirical measurements of DIS's dispersion from previous oberving runs, we know that the dispersion can change from 0.58 Å pix^{-1} by as much as 0.01 Å pix^{-1} from night to night. Based on the pixel separation between the observed Hα emission from NGC 4517 and the 6577.285 Å sky line doublet (which we use to measure the velocity of the Hα-emitting gas), this uncertainty in the dispersion

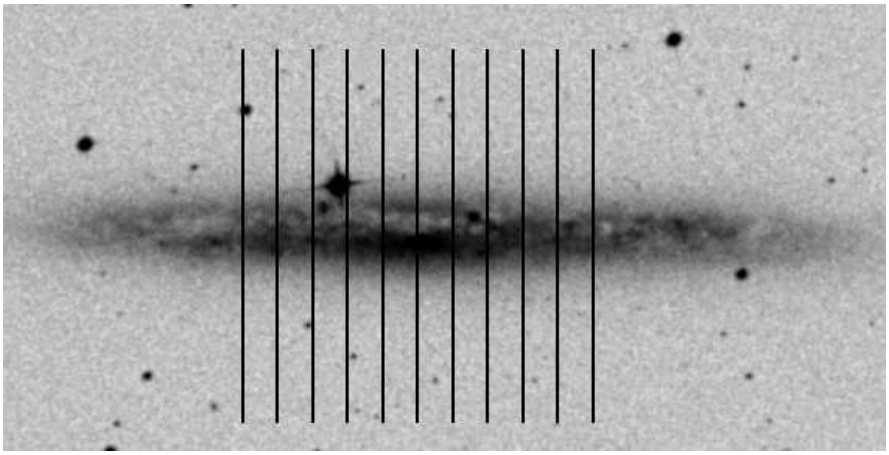

Fig. 4.1.— Slit positions for NGC 4517 overlaid on a Digital Sky Survey image. North is up, and east is to the left. The slits are $4'$ long, which corresponds to 12.9 kpc at a distance of 11.1 Mpc. The central slit (slit 6) lies on the center of the galaxy, and the slits are spaced by $22.5''$.

value results in a systematic error of $\sim$9 km s^{-1} for all of our measurements. This error is roughly constant along a given slit, so it will not affect the shape of our measured velocity profile, and the shape is the key factor that allows us to determine if the extraplanar gas is lagging. Our slit positions for NGC 4517 are overlaid on an optical image from the Digitized Sky Survey in Figure 4.2.

In addition to our target field in NGC 4517, we also took a 15 minute exposure with our slits parallel to the major axis and slit 6 along the midplane to measure the rotation curve. We used this for our modeling of that galaxy.

We observed separate fields on the approaching and receding halves of NGC 4565. Our slit locations for both fields are shown in Figure 4.2, and our final spectra are shown in Figure 4.10. We subtracted a blank sky frame from our target frame each night to remove sky lines, and we removed sky line remnants with IRAF's BACKGROUND task, which we described in Chapter 2.

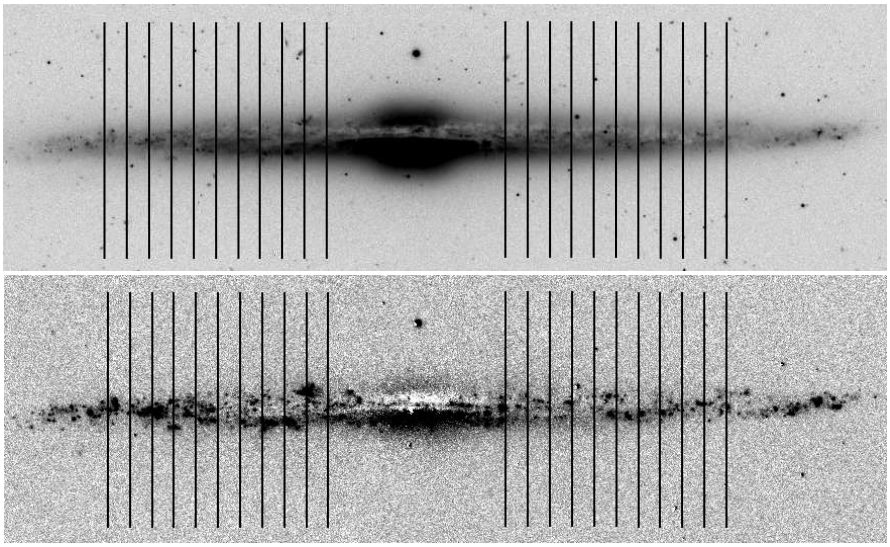

Fig. 4.2.— Slit positions for NGC 4565 overlaid on an Hα image (top) and a continuum-subtracted Hα image (bottom). North is up, and east is to the left. Both images are from KPNO (Patterson & Walterbos 2013; Patterson 2013). The inner-most slits for both fields are 1.5′ from the galaxy center. The eastern field is the approaching side of the galaxy, and the western field is receding. The slits are 4′ long, which is 12.6 kpc at a distance of 10.8 Mpc.

We used the 6590 Å filter for observing both fields and measured the dispersion for each night using sky lines at 6577.3 Å and 6596.6 Å. We measured the dispersion at several points along each slit on each night, and our average dispersion measurements were 0.585 Å for two nights on the east field and 0.586 Å for one night on the west field. We also measured the standard deviation of the dispersion across the field of view for each night. Similar to our NGC 4517 data, we calculated the velocity error that the uncertainty in dispersion adds to our measurements, which was 5.9 km s^{-1} for the east field and 3.1 km s^{-1} for the west field.

We observed the west, receding half of NGC 5907 over six nights. The first three nights had an average dispersion of 0.584 Å pix^{-1}, which we measured from three sky lines in the 6570 Å filter (6562.82 Å, 6568.78 Å, and 6577.28 Å). The

second three nights had an average dispersion of 0.579 Å. We had one night of observing on the east, approaching side of the galaxy, and our measured dispersion was 0.566 Å pix^{-1}. Our eastern field also covered the galaxy's center. Our slit locations for both fields are shown in Figure 4.3, and our multi-long-slit sepctra are shown in Figure 4.19. After subtracting a blank sky frame from our west field, we used the BACKGROUND task to remove sky line remnants. This additional step was not done for the east field.

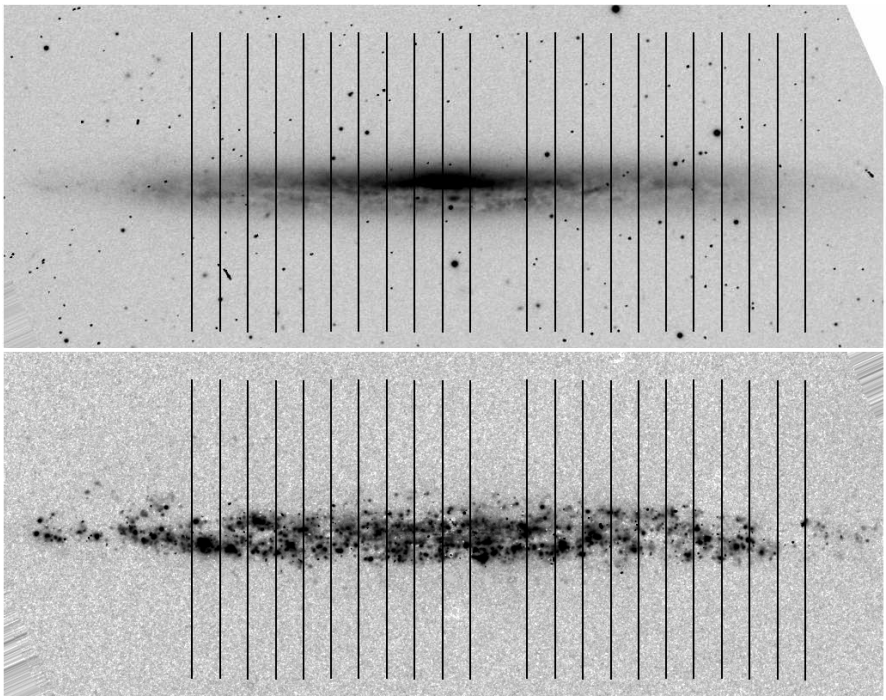

Fig. 4.3.— Slit positions for NGC 5907 overlaid on a red continuum image (top) and a continuum-subtracted Hα image (bottom). North is up, and east is to the left. Both images are KPNO images from Rand (1996). In the east field, slit 10 (counting from the left) is on the galaxy center. Slit 1 of the west field is 67.5″ west of the galaxy center. The slits are 4′ long, which is 12.8 kpc at a distance of 11.0 Mpc.

4.3. Modeling and Results

4.3.1. NGC 4517

The multi-long-slit spectrum of NGC 4517, shown in Figure 4.5, shows what appears to be an extreme lag close to the midplane of the galaxy, which is indicative of a highly inclined (but not edge-on) disk with a small scale height. Since this galaxy shows these inclination effects, we cannot easily measure an observed scale height from our observations. Instead, we tested models with a single disk with a scale height that ranges from 100 pc to 500 pc. Our models use an optical diameter at 25$^{\text{th}}$ magnitude of 9.5′ (Tully et al. 2009) as a cutoff for Hα emission in the disk, and they are inclined at 87.4° (Goudfrooij et al. 2003). Our input rotation curve (Figure 4.4) is taken from a multi-long-slit exposure of NGC 4517 with the central slit along the major axis of the galaxy.

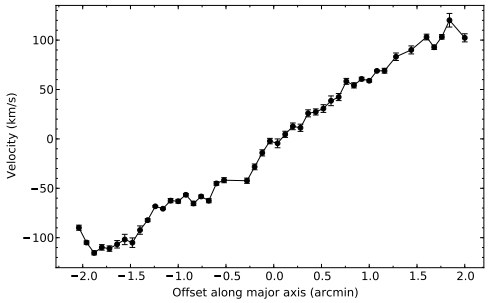

Fig. 4.4.— Rotation curve for NGC 4517, taken from a multi-long-slit exposure with the central slit along the major axis.

A single disk with a scale height of 300 pc provides a good match to the data, and the scale height is sufficient to get emission high enough above the midplane in all but two of the slits. Models with a scale height of 100 – 200 pc also fit the

data well, but only within 1 – 2 kpc of the midplane. These disks are too thin to produce emission at greater distances from the midplane like we see in the data. Models with a scale height greater than 300 pc cannot produce the sharply curved velocity profile (so-called 'inclination effects') that we see near the midplane, so we can rule out a disk thicker than this for a single-component model.

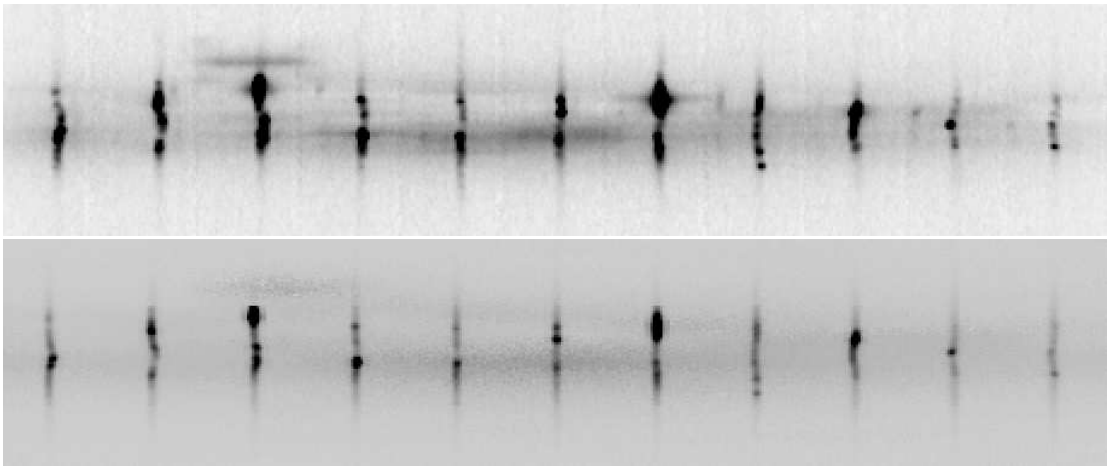

Fig. 4.5.— NGC 4517 data (top) and model (bottom) spectra. The model shown here has a thin disk with a scale height of 150 pc and a thick disk with a scale height of 1.0 kpc. Neither disk has a lagging component. North is up, east is to the left, and wavelength increases to the left. The vertical (spatial) extent of each spectrum is 1.9′ (6.3 kpc).

Adding a lag to the 300 pc disk only adds a small improvement to the models. Model profiles for slit 6, which lies exactly on the galaxy center, are all the same, regardless of the value of the lag because all of the emission we measure from the slit is at systemic velocity. Slit 9 is the only profile that sees significant improvement with a lag. Our model velocities overlaid with the data are shown in Figure 4.6, and the lag values are shown in Figure 4.8. Lag values for slits close to the galaxy center tend to have large error bars because most of the emission

we see at those slits has a velocity perpendicular to our line of sight, and we are only measuring a small component of the rotational velocity. The slits near the edge of the galaxy on the western side have large error bars because we do not see emission very far from the midplane. Gas that is close to the midplane, even if it has a large lagging value, does not have a velocity that is very different from gas with no lag because its distance from the midplane is so small.

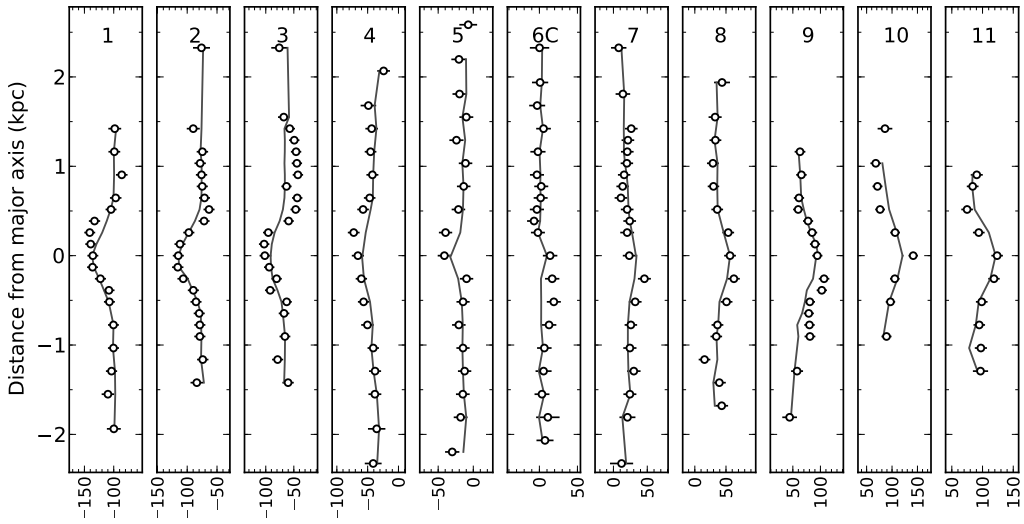

Fig. 4.6.— NGC 4517 single-component model velocities. Model velocities are shown as a solid line, and the data are plotted as open circles. This model has a scale height of 300 pc and a radially varying lag, the values of which are shown in Figure 4.8.

We also modeled NGC 4517 with a two-component disk. A thin disk with a scale height of 150 pc produces inclination effects that are very similar to that seen in the data. This disk does not have a lag, and its emission is scaled to match the clumpiness we see in the data near the midplane. We add a thicker, fainter disk, the density of which is constant within 1 kpc of the midplane and decreases exponentially with a scale height of 1.0 kpc above that. We tested lags ranging

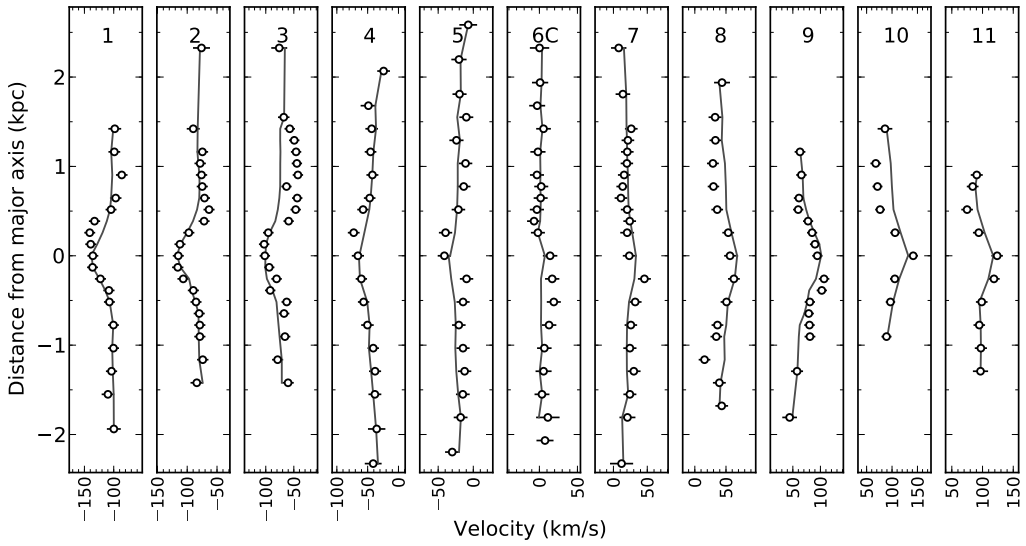

Fig. 4.7.— NGC 4517 two-component model velocities. Model velocities are shown as a solid line, and the data are plotted as open circles. This model consists of a thin disk with a scale height of 150 pc and a thick disk with a scale height of 1.0 kpc. The thick disk has a lag which varies with radius, and the values for the lag are shown in Figure 4.9.

from 0 – 70 km s^{-1} kpc^{-1} for the thick disk, and we kept the vertical density distribution smooth.

With the addition of the thicker disk, we can get emission high enough above the midplane to match the data in all the slits. Our model velocities are shown with the data in Figure 4.7, and the values of the lag for the thick disk are shown in Figure 4.9. The thin disk dominates the emission close to the midplane, where we see inclination effects mimicking a strong lag. The thick disk dominates the emission farther from the midplane, and a thick disk that lags the thin disk in rotation in slits 4-10 provides a better match to the data.

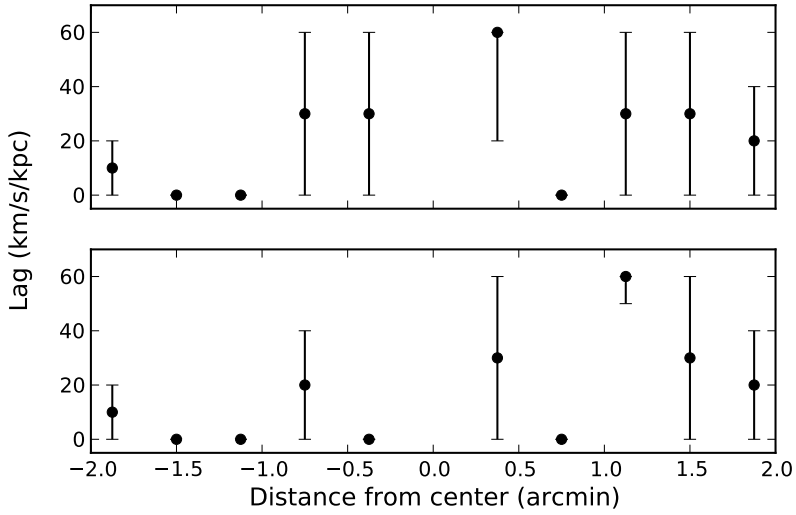

Fig. 4.8.— NGC 4517 thin disk model lag values. The value of the lag is plotted as a function of radius for the above (top) and below (bottom) the midplane of the galaxy. Negative values for the radius indicate the east side of the galaxy. We did not run models with lags greater than 60 km s^{-1} kpc^{-1}, so points at that value are not upper limits for models that would fit the data. We cannot constrain the value of the lag close to the galaxy center.

4.3.2. NGC 4565

Our mulit-long-slit spectra for both fields in NGC 4565 are shown in Figure 4.10. This galaxy shows inclination effects near the midplane, which indicates a small scale height and an inclination slightly less than 90°.

Our models for the approaching and receding sides of NGC 4565 assume a disk diameter of 16.2′ and an inclination of 87.5°. For an infinitely thin disk, we would see disk emission out to projected distances of 0.4′, or 1.2 kpc, from the midplane. Most of the emission we see in the west field is contained within these distances, which means we detect very little EP emission, and this field can likely be fit with a single, thin disk. HI models by Zschaechner et al. (2012) show a

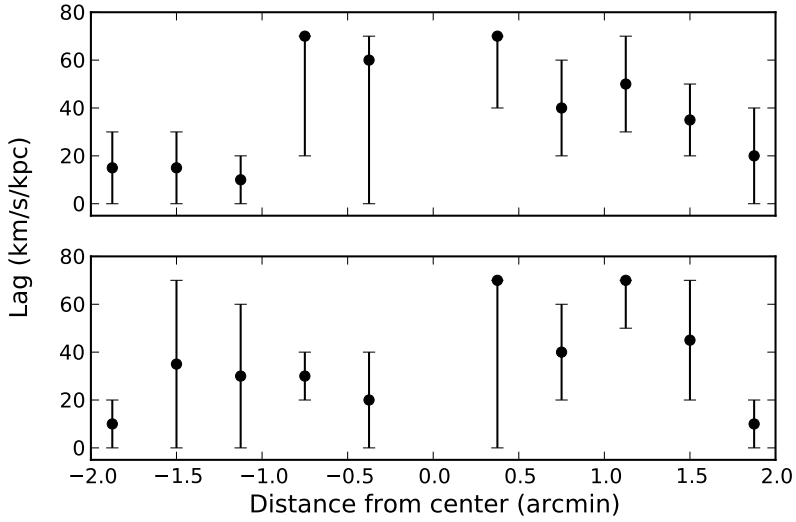

Fig. 4.9.— NGC 4517 thick disk model lag values. The value of the lag is plotted as a function of radius for the above (top) and below (bottom) the midplane of the galaxy. Negative values for the radius indicate the east side of the galaxy. We did not run models with lags greater than 70 km s^{-1} kpc^{-1}, so points at that value are not upper limits for models that would fit the data. We cannot constrain the value of the lag close to the galaxy center.

scale height of 0.2 – 0.4 kpc in the inner region where our slitmask lies. Because this galaxy is not edge-on, we cannot easily measure a scale height from our data, so we use an adopted value from the HI models. We also use the rotation curve derived from the HI modeling.

For a fixed inclination of 87.5°, letting the scale height vary between 100 pc and 500 pc from slit to slit provides good fits for most of the data in the west field. A comparison between these models and the data is shown in Figure 4.11, and the scale height at each slit radius is shown in Figure 4.12.

We also tested models with constant scale heights of 200 pc and 400 pc and let the inclination vary between 86° and 88°. Our results for these models are shown in Figure 4.13 and 4.14, and the inclination for each slit for each of the

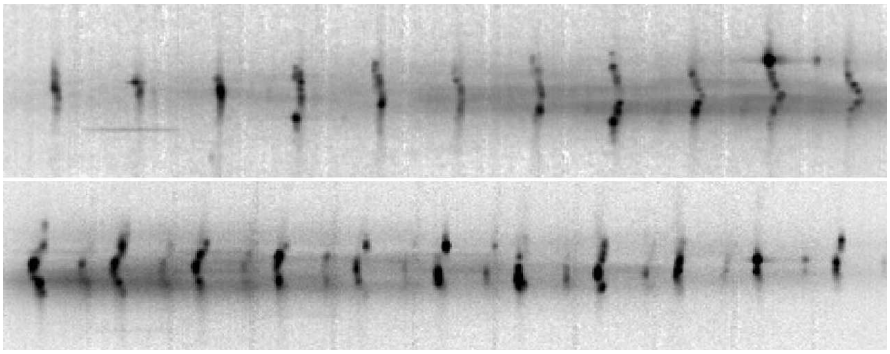

Fig. 4.10.— Multi-long-slit spectra of NGC 4565. Top: East field. Bottom: West field. In both spectra, north is up and east is to the left, and wavelength increases to the left. The vertical (spatial) extent of each spectrum is 1.8′ (5.66 kpc).

models is shown in Figure 4.15. The models with a constant scale height of 200 pc provide a better fit than the models with a scale height of 400 pc. In general, keeping the scale height or inclination constant and allowing the other variable to vary produces similar results. Both approaches indicate a small scale height, litle to no extraplanar gas, and a disk that is close to edge-on.

Adding a lagging component to any of these models or the models inclined at 87.5° does not improve the fits. However, because most of the emission we see is close to the midplane, a lagging component has a small effect on the velocity profiles. Figure 4.16 shows the velocity profiles for models with and without a lag of 20 km s^{-1} kpc^{-1} and a constant scale height of 400 pc. The profiles are too similar to reliably distinguish the two, so we cannot determine whether there is lagging gas in this field. Additionally, if our observations are dominated by a bright, thin disk, we might be unable to detect fainter, lagging gas.

We added a second disk with a larger scale height to our models of the west field, but there was no improvement. The east field, however, has much more extended Hα emission, and a two-component model is required to match the data.

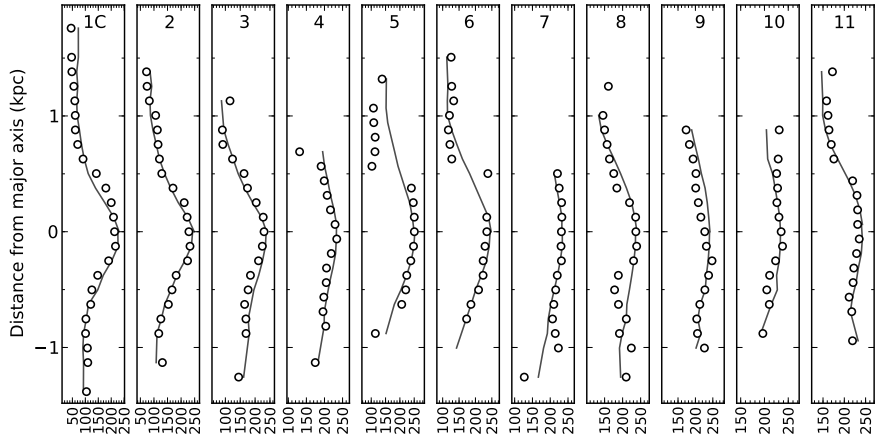

Fig. 4.11.— NGC 4565 west models and data. These models are inclined at 87.5°, and the scale height varies between 100 pc and 500 pc for each slit. The open circles are the data, and the solid lines are the model velocities.

The velocity profiles of the east and west fields show very similar patterns within 1 kpc of the midplane, so we omit a discussion of our single-component models for the east field.

Figure 4.17 shows our two-component model profiles compared to the data for the east field of NGC 4565. The thinner disk has a scale height that varies between 100 pc and 500 pc as a function of radius, and the emission is scaled to match any clumpiness we see in the data. The thicker disk has an exponential scale height of 1.0 kpc, and its emission is smooth instead of being scaled to match specific features. Both disks are inclined at 87.5°, and a lag is necessary in the thick disk to match the data. Scale height and lag as a function of radius are shown in Figure 4.18.

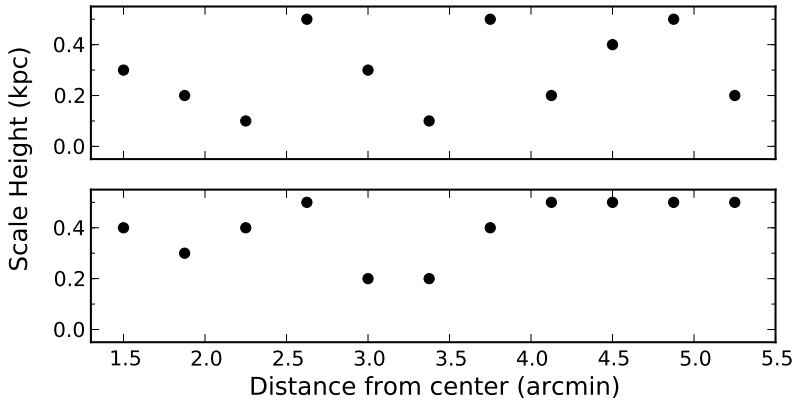

Fig. 4.12.— Scale Height for NGC 4565 West Models Inclined at 87.5°. The top panel shows model scale heights above the midplane, and the bottom panel shows model scale heights below the midplane.

4.3.3. NGC 5907

Our spectra for two fields in NGC 5907 are shown in Figure4.19. Similar to NGC 4565, this galaxy shows inclination effects.

We adopt an inclination of 87° and a disk diameter of 12.6′ for our models of NGC 5907. Our Hα data show that NGC 5907 displays inclination effets arising from its high inclination and small scale height, so we test a range of scale heights between 100 pc and 500 pc. As discussed for our NGC 4565 models, keeping the inclination constant and varying the scale height within a small range or keeping the scale height constant and varying the inclination within a small range produces similar modeling results, so we do not test different inclinations.

The rotation curve we use for our models is from a combination of Sancisi & van Albada (1987), from HI observations, and Barnaby & Thronson (1994), from modeling of near-IR observations. Because the observed velocity profiles for our east and west fields (shown in Figures 4.20 and 4.21) of this galaxy show the same

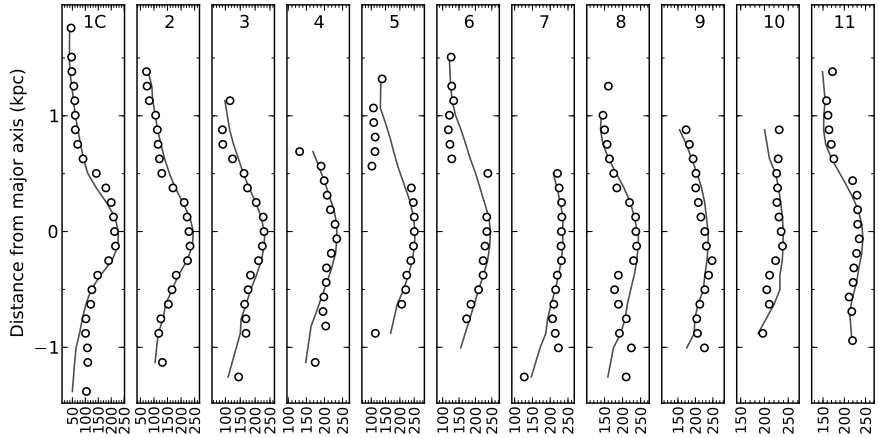

Fig. 4.13.— NGC 4565 west models with a scale height of 200 pc. The open circles are the data, and the solid lines are the model velocities. The inclination for these models was allowed to vary between 86° and 88° , and the inclination values are shown in Figure 4.15.

pattern, we only model the east field.

In the slits near the center of the galaxy, we see emission up to 1.5 kpc. Assuming an infinitely thin disk with an inclination of 87°, we would see disk emission at a projected distance of 1.5 kpc from the midplane if the radius of the disk were 29 kpc, or 9.1′. This is much larger than the 6.3′ radius we use for our models, so we can rule out a single, thin disk. A single disk with a scale height in the range of 300 pc – 500 pc, however, produces very good fits to our data. Velocities for our 1-component model are shown in Figure 4.20, and the values of our model scale heights for each slit are shown in Figure 4.22.

Our multi-long-slit observations show that the Hα emission is very clumpy from 1 kpc below the midplane to 0.5 kpc above it. The Hα image from Rand (1996) also shows very clumpy Hα emission close to the midplane. To reproduce this in the models, we scale the model emission in the −1.0 to +0.5 kpc vertical distance range to match discrete features in the observations. Outside of that

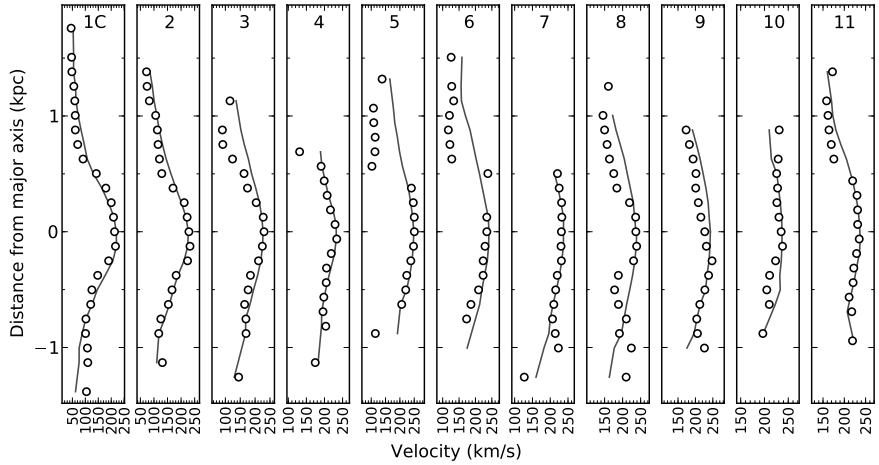

Fig. 4.14.— NGC 4565 west models with a scale height of 400 pc. The open circles are the data, and the solid lines are the model velocities. The inclination for these models was allowed to vary between 86° and 88° , and the inclination values are shown in Figure 4.15.

range, the model emission follows a smooth, exponential decrease. We are able to reproduce the vertical extent of the emission in this manner, and there is no need for a second, thicker component.

Because most of the observed Hα emission is within 1 – 1.5 kpc of the midplane, we cannot determine whether the gas velocities show a vertical gradient.

4.4. Conclusions

NGC 4517 data can be modeled by a single thin disk with a scale height of 300 pc, but we cannot definitely say whether there is lagging component. A lag of 0 – 20 km s^{-1} kpc^{-1} fits most slits on upper and lower halves of the galaxy. However, since we see emission up 2.5 kpc from the midplane, it is likely that this galaxy has a thicker disk as well. We also modeled NGC 4517 with a thin and thick disk with scale heights of 150 pc and 1.0 kpc, respectively. Our best models have a

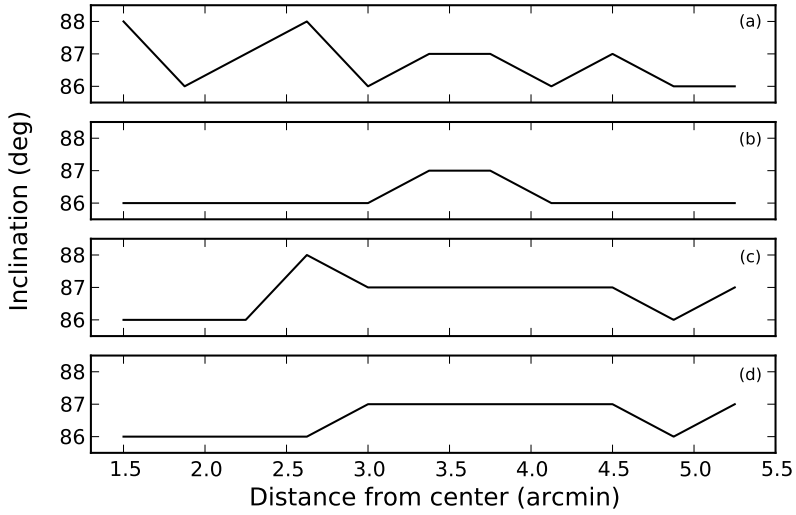

Fig. 4.15.— Inclination for NGC 4565 west models with constant scale height. Panels *a* and *b* show the inclination above and below the midplane, respectively, for models with a constant scale height of 0.2 kpc. Panels *c* and *d* show the same for models with a constant scale height of 0.4 kpc.

thick disk with lags of 40 – 60 km s^{-1} kpc^{-1} in the central slits (from a radius of $-1'$ to $+1.2'$) and lags of 0 – 20 km s^{-1} kpc^{-1} in the outer slits. The western side shows definitive evidence for a radially decreasing lag. The eastern side shows only a slight trend of lag decreasing with radius, but this half of the galaxy shows a lot of dust obscuration in the optical DSS image, which can affect our velocity measurements. To our knowledge, our observations are the first indication that NGC 4517 has a thick Hα disk.

The west (receding) field of NGC 4565 does not show a lot of extended Hα emission. We are dominated by inclination effects and a small scale height, and we cannot determine if the extraplanar gas is lagging. Modeling this field with a thin disk with a scale height of 200 pc produces good fits to the data. We also modeled this field with a disk with a scale height of 400 pc. That model produces

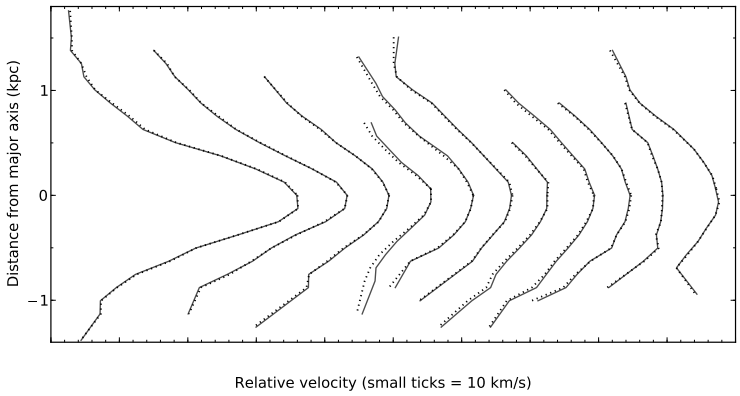

Fig. 4.16.— Comparison of models with and without a lag for the west field of NGC 4565. The solid lines show model velocities with a constant scale height of 0.4 kpc and no lagging component. Inclination varies between 86° and 88°. The dotted lines show the same models after adding a lag of 20 km s^{-1} kpc^{-1}. All of the profiles have been shifted an arbitrary amount for display purposes.

significantly worse results, so there does not appear to be an extended DIG layer on the west side.

The east (approaching) field of NGC 4565, however, shows more vertically extended Hα emission. This is in agreement with Rand et al. (1992), who detected ionized emission up to 2.0 kpc on the east side but only up to 1.5 kpc on the west side. A qualitative analysis of our continuum-subtracted Hα image from KPNO (Figure 4.2) shows the Hα emission is brighter on the east side. It is interesting to note that the brighter east side of this galaxy appears to be fairly quiescent, while the west side is interacting with a small companion $6'$ northwest of its center, IC 3571, and an HI bridge has been observed between the two (van der Hulst & Sancisi (2005); Heald et al. (2011)). NGC 4565 also has another companion located $15'$ southwest of the galaxy center (van der Hulst & Sancisi (2005) and references therein).

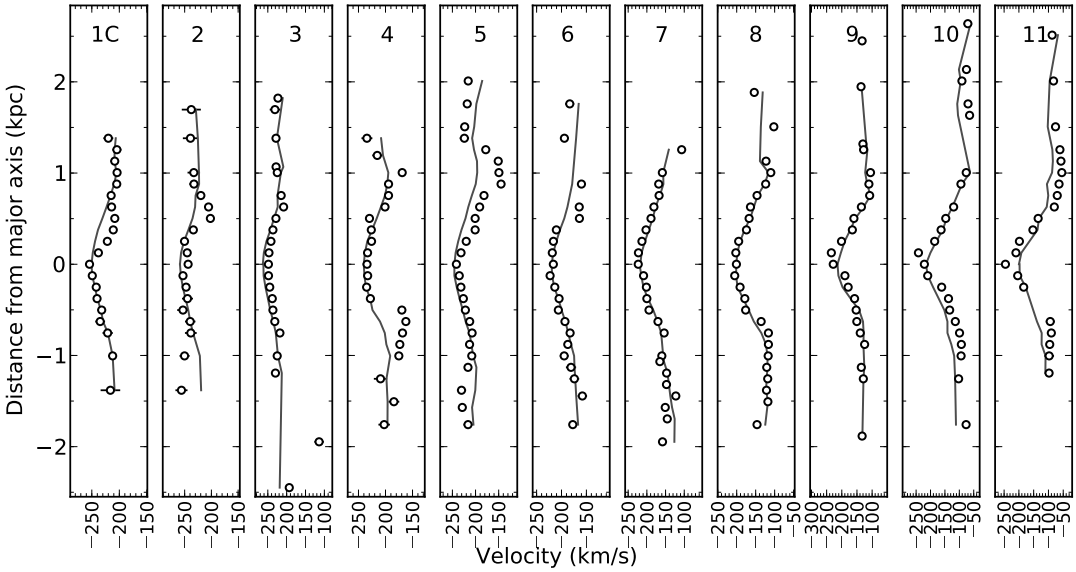

Fig. 4.17.— Two component model for NGC 4565 east. The solid lines show model velocities, and the data are open circles. The scale height of the thinner disk varies between 100 and 500 pc, and the thicker component has a radially varying lag. The values of the scale height and lag for each slit are shown in Figure 4.18.

We modeled the east field of NGC 4565 with a thinner disk with a radially varying scale height plus a thick disk with a scale height of 1.0 kpc. The thinner disk appears to have a flare, as the scale height is 100 pc at small radii and increases to 500 pc at larger radii. This is very similar to the models of Zschaechner et al. (2012), which found that the scale height of the HI gas is 200 pc near the galaxy center and increases to 400 pc over the same radial range as our multi-long-slit observations.

Similar to the west side of NGC 4517, the thick disk in the east field of NGC 4565 shows a strong trend of lag decreasing with radius. The lag is $\sim$70 km s^{-1} kpc^{-1} in the inner most slits, at a radius of $1.5' - 2.0'$. Beyond that, the lag goes from $\sim$40 km s^{-1} kpc^{-1} at $2.25'$ to no lag at $3.7'$. Zschaechner et al. (2012) found

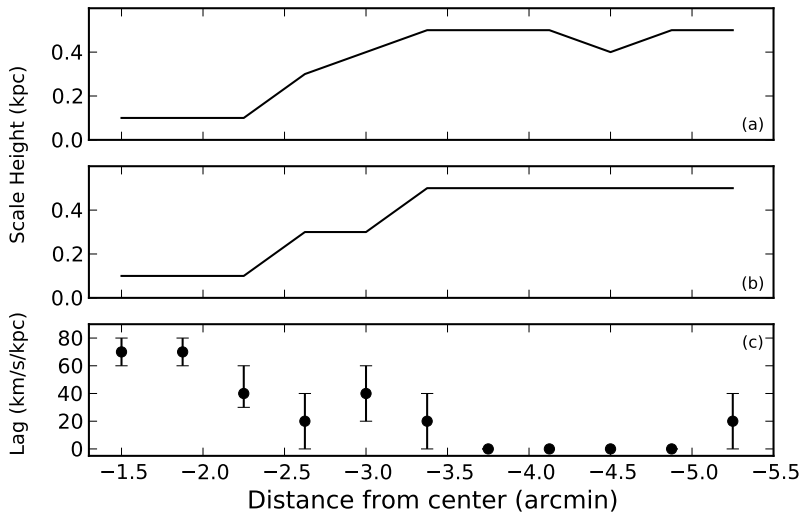

Fig. 4.18.— Model scale height and lag for NGC 4565 east. Scale height for the thinner disk as a function of radius is shown for the upper and lower halves of the galaxy in panels *a* and *b*, respectively. Panel *c* shows the lag of the thick disk, which is the same for the upper and lower halves.

that the HI gas shows a similar behavior. Their models of the east side of NGC 4565 indicate a lag of 40 km s^{-1} kpc^{-1} at a radius of 2.75′, and the lag drops to 0 at 4.75′.

Rand et al. (1992) found a thin ionized gas layer in NGC 4565 and no extended DIG with their Hα imaging. HI modeling by Zschaechner et al. (2012) found no extended HI layer. Our observations of the west side of NGC 4565 agree with their results, but our observations and modeling of the east side do indicate an extended ionized gas layer, with Hα emission detected up to 2.5 kpc from the midplane.

NGC 5907 can be modeled by a single disk with a scale height ranging from 300 pc – 500 pc. We cannot determine if there is a lag, and we find no indication of a thicker disk. Previous studies by Morrison et al. (1994) found a thin stellar disk

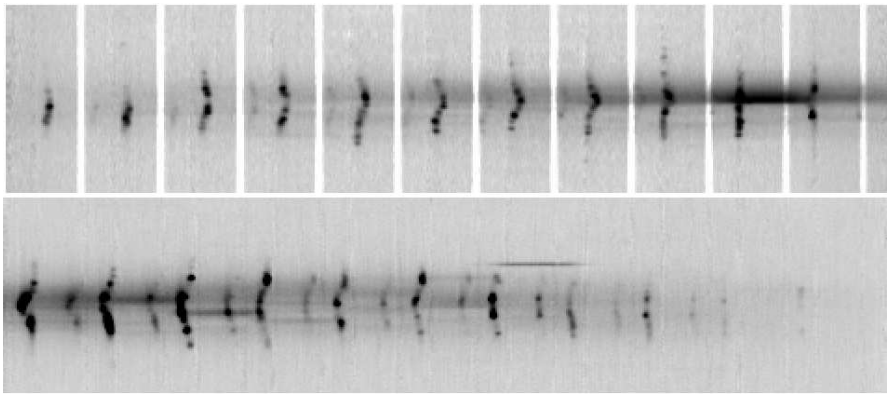

Fig. 4.19.— Multi-long-slit spectra of NGC 5907. Top: East field. Bottom: West field. In both spectra, north is up and east is to the left, and wavelength increases to the left. The vertical (spatial) extent of each spectrum is 2.0′ (6.46 kpc). We did not remove sky line remnants from the east field, and over-subtracted sky lines appear as white vertical lines. These lines are not near the observed Hα emission, so they did not affect our measurements.

with a scale height of 430 pc, and van der Kruit & Searle (1981a) modeled NGC 5907 with a single stellar disk and no thicker component. The fairly constant scale height and lack of extended EP gas point to a quiescent disk over our field of fiew (3.375′ east of center to 0.375′ west of center). NGC 5907 does show warps in its disk in optical and HI (Sancisi 1976; Sasaki 1987; Morrison et al. 1994), but the warps occur at radii of ±5.0′. HI imaging shows NGC 5907 is likely interacting with a dwarf companion (Shang et al. 1998), but that is toward the outskirts of its HI disk, and we see no signs of interactions in the ionized gas.

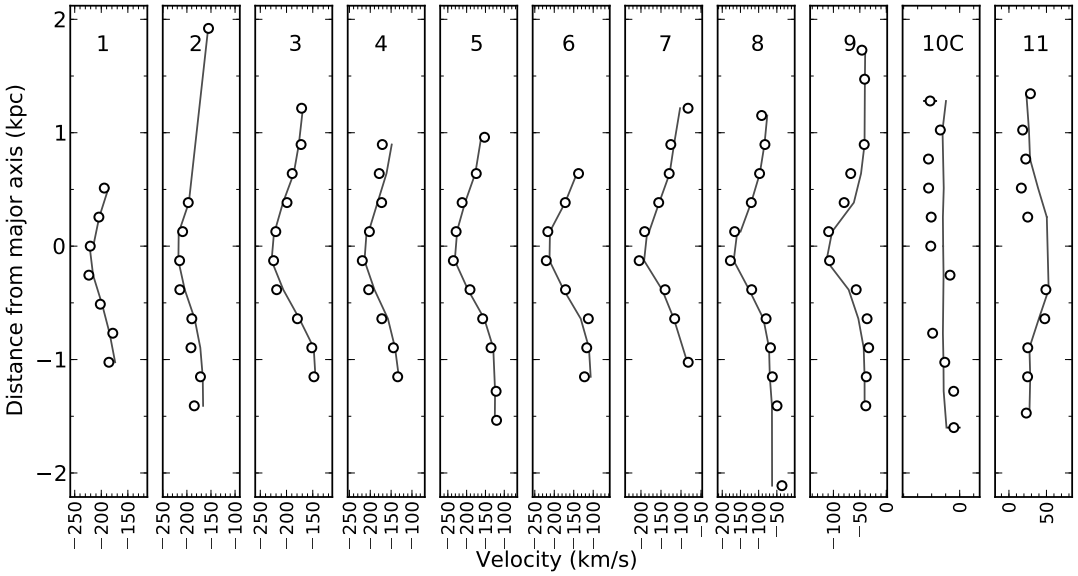

Fig. 4.20.— Model velocities for NGC 5907 east for a one-component model. The solid lines show model velocities, and the open circles are the data. The scale height of the disk ranges between 200 and 500 pc, and the exact values for each slit are shown in Figure 4.22. No lagging component is included in this model.

Table 4.1. Observing Parameters: NGC 4517, NGC 4565, and NGC 5907

Parameter	NGC 4517	NGC 4565	NGC 5907
RA (J2000) [a]	$12^h32^m45.6^s$	$12^h36^m21.0^s$	$15^h15^m53.8^s$
Dec (J2000) [a]	$+00°06'54.0''$	$+25°59'13.0''$	$+56°19'44.0''$
PA (°)	83	136	155
v_{sys} (km s^{-1}) [a]	1131	1230	666
Hα wavelength at v_{sys} (Å)	6587.7	6590.0	6577.6
Narrowband filter center (Å)	6580	6590	6570
Observing dates (UT)	25, 27 Mar. 2012 29 Mar. 2011[b]	20 Feb., 19 Mar. 2010[c] 17 May 2010[d]	30 Apr. 2011[c] 14-15 May, 15 June 2009[d] 24-26 July, 2009[d]
Grating (lines mm^{-1})	1200	1200	1200
Dispersion (Å pix^{-1})	0.580	0.585	0.566[c] , 0.582[d]
Total integration time (hrs)	4.3, 0.25[b]	5.0[c] , 5.0[d]	5.5[c] , 9.8[d]
Field location[d] ($'$)	0.00	−3.38[c] , 3.38[d]	−1.88[c] , 3.0[d]

[a]From NED.
[b]For the field with slit 6 along the major axis.
[c]For the east field
[d]For the west field.
[e]Offset from galaxy center to slit 6, the middle of our field. Negative values are east of the galaxy center.

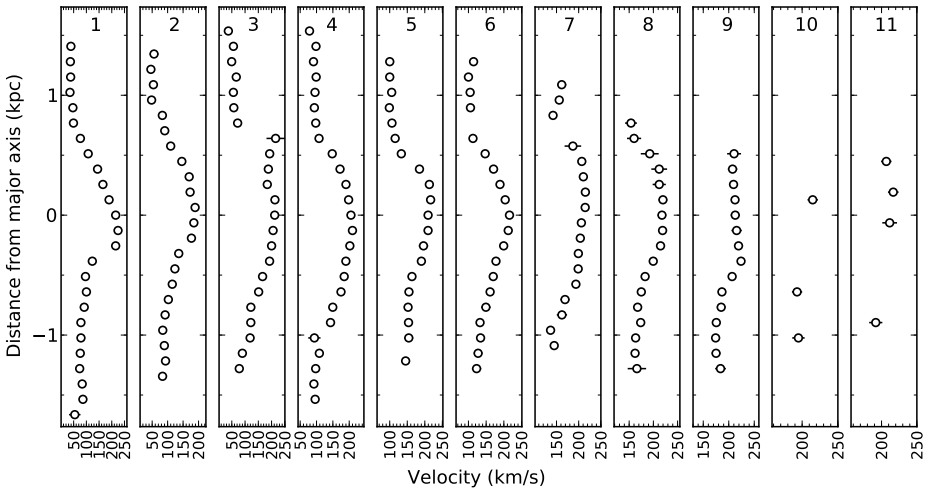

Fig. 4.21.— NGC 5907 West Velocity Field. These velocity profiles show the same shape as the NGC 5907 east field. This side of the galaxy has a small scale height and does not show extended Hα emission.

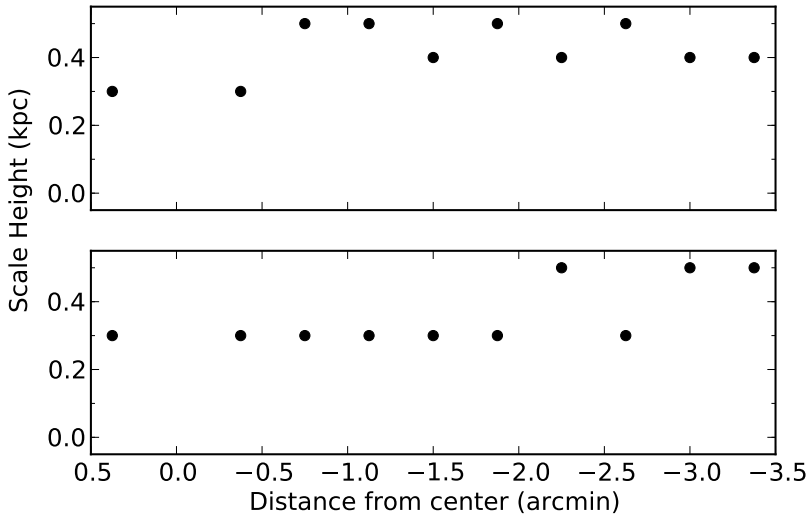

Fig. 4.22.— Model scale heights for NGC 5907 east.

5. MULTI-LONG-SLIT SPECTROSCOPIC OBSERVATIONS OF EIGHT EDGE-ON GALAXIES

5.1. Introduction

The remaining galaxies in our sample show very little extraplanar (EP) gas, no lagging component, or complicated profiles that cannot be fit by our simple models. We summarize our results for these galaxies in this chapter. Tables 5.1 and 5.2 show the observing parameters for these galaxies, which we split into two groups: those that show EP gas and those that do not. We use 2.0 kpc as a cutoff for the minimum height from the disk at which Hα emission must be detected to be considered a galaxy with EP gas.

Of the four galaxies in which we detect EP gas, two of them (NGC 3044 and NGC 3079) show inclination effects. We detect Hα emission 2 – 3 kpc from the midplane in both galaxies, and both galaxies may or may not having a lagging component. The other two galaxies in this group, NGC 3628 and NGC 4013, show emission up to 2 kpc from the midplane. They do not seem to have any lagging gas.

The last four galaxies in our sample have little or no EP ionized gas. We did not detect any Hα emission in one galaxy, NGC 4762. UGC 4278 shows emission 1 – 1.5 kpc from the midplane, and the gas velocities are constant with height above the disk. In NGC 5229 and UGC 7321, we only detect Hα emission within 0.3 kpc of the midplane.

The data reduction techniques and methods for measuring velocities are the same for these galaxies as for the rest of the sample. A detailed description of those processes can be found in Chapter 2.

Table 5.1. Galaxies with Extraplanar Gas

Parameter	NGC 3044	NGC 3079	NGC 3628	NGC 4013
RA (J2000) [a]	$9^h53^m41.0^s$	$10^h1^m57.8^s$	$11^h20^m17.0^s$	$11^h58^m31.4^s$
Dec (J2000) [a]	$+1°34'45.0''$	$+55°40'47.0''$	$+13°35'23.0''$	$+43°56'48.0''$
PA (°)	113	165	104	66
v_{sys} (km s^{-1}) [a]	1335	1125	843	831
Hα wavelength at v_{sys} (Å)	6591.2	6587.4	6581.5	6581.2
Narrowband filter center (Å)	6590	6580	6580	6580
Observing dates (UT)	17-18 Mar. 2010	25 Mar. 2012	30 Mar. 2011	29 Mar. 2011
Grating (lines mm^{-1})	1200	1200	1200	1200
Dispersion (Å pix^{-1})	0.58	0.58	0.58	0.58
Total integration time (hrs)	6.4	2.25	6.0	6.4
Field location[c] ($'$)	0.38	0.00	−1.88	0.00

[a]From NED.
[b]For the east and west fields, respectively.
[c]Offset from galaxy center to slit 6, the middle of our field. Negative values indicate east of the galaxy center.

Table 5.2. Galaxies with Little or No Extraplanar Gas

Parameter	UGC 4278	NGC 5229	UGC 7321	NGC 4762
RA (J2000) [a]	$8^h13^m58.9^s$	$13^h34^m02.8^s$	$12^h17^m34.0^s$	$12^h52^m56.0^s$
Dec (J2000) [a]	$+45°44'32.0''$	$+47°54'56.0''$	$+22°32'23.0''$	$+11°13'51.0''$
PA (°)	172	167	82	32
v_{sys} (km s^{-1}) [a]	565	365	403	942
Hα wavelength at v_{sys} (Å)	6574.6	6570.8	6571.9	6584.5
Narrowband filter center (Å)	6570	6570	6570	6580
Observing dates (UT)	8-9 Dec. 2010	28 Apr. 2011	12 May 2013	28 Mar. 2011
Grating (lines mm^{-1})	1200	1200	1200	1200
Dispersion (Å pix^{-1})	0.564	0.571	0.572	0.58
Total integration time (hrs)	7.2	5.0	2.5	7.5
Field location[b] ($'$)	0.00	0.00	0.00	1.88

[a]From NED.
[b]Offset from galaxy center to slit 6, the middle of our field. Positive values are west of the galaxy center.

5.2. NGC 3044

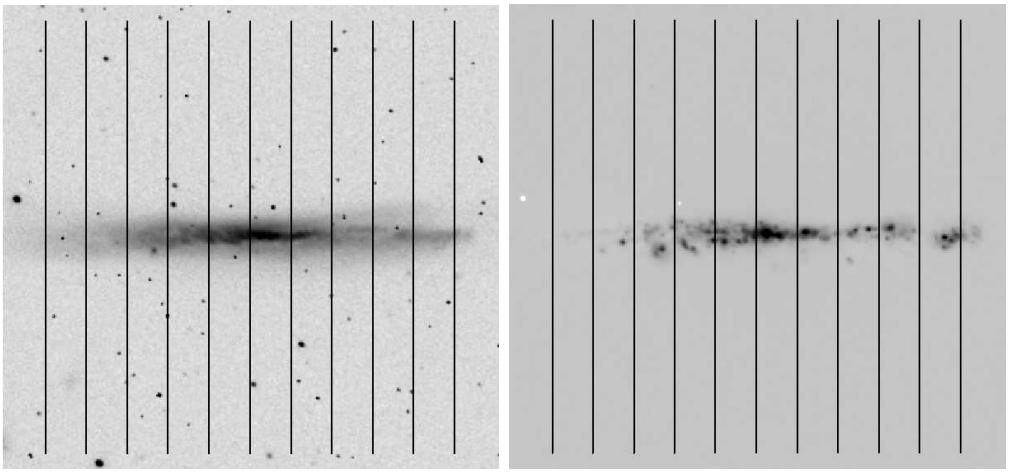

Fig. 5.1.— Slit positions for NGC 3044 overlaid on an R-band image (left) and an Hα continuum-subtracted image (right) from Collins et al. (2000). North is up, and east is to the left. The slits are $4'$ long, which corresponds to 25.2 kpc at a distance of 21.7 Mpc. The central slit (slit 6) lies on the center of the galaxy, and the slits are spaced by $22.5''$.

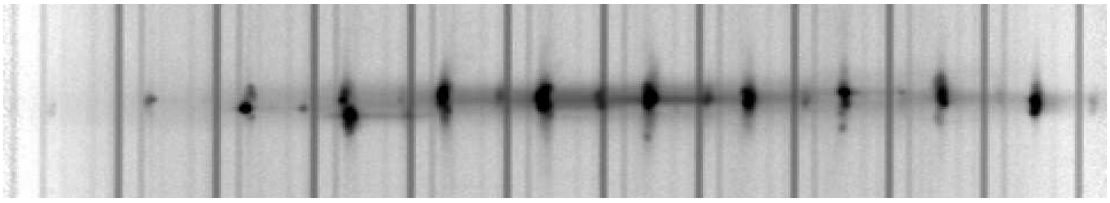

Fig. 5.2.— Multi-long-slit spectrum of NGC 3044. North is up, east is to the left, and wavelength increases to the left. The vertical extent of the spectrum is 10.7 kpc. The vertical lines are sky lines.

Figure 5.1 shows our slit locations for NGC 3044 overlaid on R-band and Hα images. The Hα emission is more extended on the west side of the galaxy, which is apparent in our multi-long-slit spectrum (Figure 5.2). Our slit mask is centered on the galaxy, but slit 1 has very little emission, while slit 11 has significant emission.

The radial distribution of Hα-emitting gas is obviously asymmetric. There is also a large jump in velocities between slits 6 and 7, which can be seen in Figure 5.3. We show our grayscale spectrum (Figure 5.2) before sky line subtraction to highlight this. In the central slit, the observed Hα emission is very close to a sky line, but in the neighboring slit, the observed Hα is significantly farther from that same sky line. This indicates a rotation curves that rises steeply in the inner 22.5″ of the galaxy on the approaching side, while the rotation curve on the receding side rises more gradually. NGC 3044 is not an interacting galaxy (Solomon & Sage 1988), so the highly irregular kinematics are unexpected.

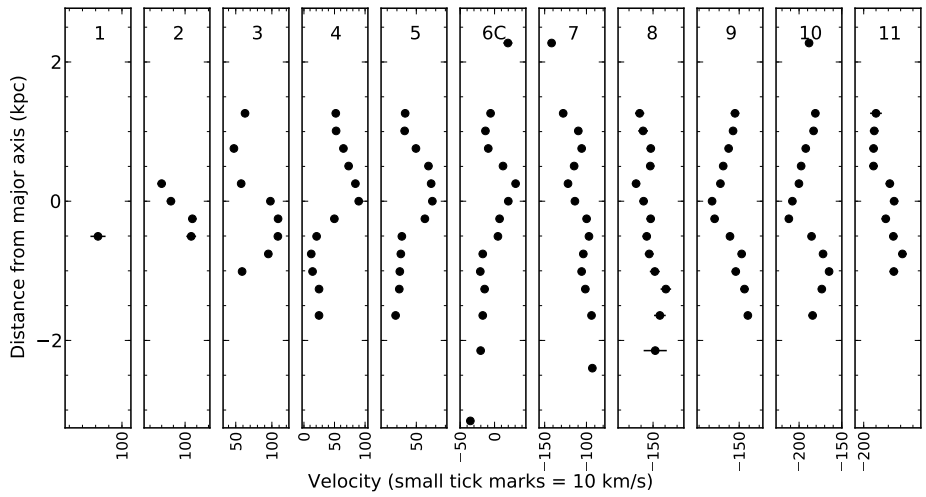

Fig. 5.3.— Multi-long-slit velocities for NGC 3044.

Hα imaging by Rossa & Dettmar (2000) shows extraplanar DIG up to 1 kpc from the midplane, along with plumes and Hα loops. They suggest NGC 3044 might be a starburst galaxy, or it might have a higher than normal star formation rate for a quiescent galaxy. Collins et al. (2000) also observed bright extraplanar

DIG and faint filaments above central part of the galaxy. Our DIG detections extend to 2 – 3 kpc from the midplane. The velocity profiles show disturbed motions in the gas and inclination effects from the disk not being fully edge-on. Modeling of this galaxy might shed light on whether the EP gas is lagging the disk, but the irregular kinematics complicate the analysis.

5.3. NGC 3079

NGC 3079 is a highly active galaxy. It has been classified as a LINER (Heckman 1980) or Seyfert (Ford et al. 1986) galaxy with large outflows. It has two companions: MCG 9-17-9 to its northeast and NGC 3073 to its southeast (de Mello et al. 2012). NGC 3073 is a dwarf galaxy with an elongated HI tail pointing toward NGC 3079. Optical imaging by Taylor et al. (2005) revealed radially extended, diffuse emission on the east side of the galaxy, which might be related to its companions. Veilleux et al. (1994) found high velocity gas motions and evidence of shocks.

The slit locations of our observations are shown in Figure 5.4, and our multi-long-slit spectrum is shown in Figure 5.5. Our data show a bowl-shaped warp perpendicular to our line of sight. There is bright, clumpy emission close to the midplane and diffuse emission above the disk. The nucleus is extremely bright in the upper half of the galaxy, but it is almost completely obscured by dust in the lower half of the midplane.

Our velocity profiles for NGC 3079 are shown in Figure 5.6. The profiles on the west side are very regular and show the pattern of a highly inclined thick disk or an edge-on disk with a lagging component. The east side velocities are much

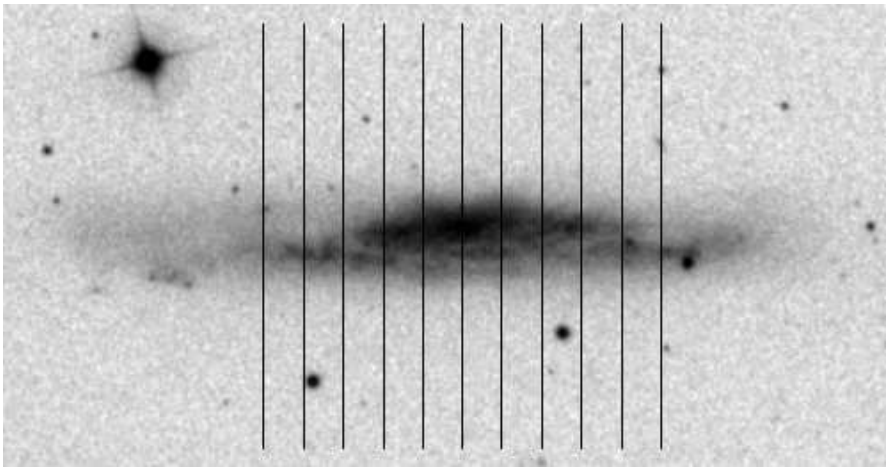

Fig. 5.4.— Slit positions for NGC 3079 overlaid on an image from the Digitized Sky Survey. North is up, and east is to the left. The slits are $4'$ long, which corresponds to 17.5 kpc at a distance of 15.0 Mpc. The central slit (slit 6) lies on the center of the galaxy, and the slits are spaced by $22.5''$.

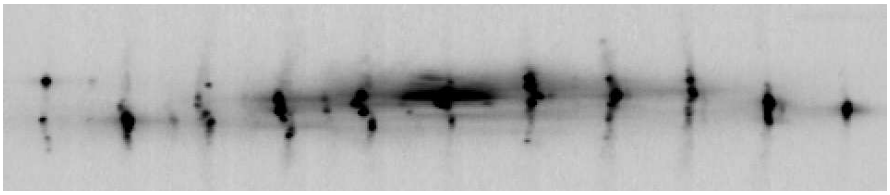

Fig. 5.5.— Multi-long-slit spectrum of NGC 3079. North is up, east is to the left, and wavelength increases to the left. The vertical extent of the spectrum is 8.7 kpc.

more irregular. The jumpiness of the profiles in the lower half of the east side is likely due to dust obscuration. The central slit shows a drastic increase in velocity near the midplane. This could be caused by radial motions associated with a bar.

5.4. NGC 3628

NGC 3628 is galaxy in the Leo Triplet (Arp 317) and shows signs of interacting with the other triplet members, NGC 3623 and NGC 3627. Chromey et al. (1998) detected a 100 kpc stellar plume extending from NGC 3628, and Burkhead

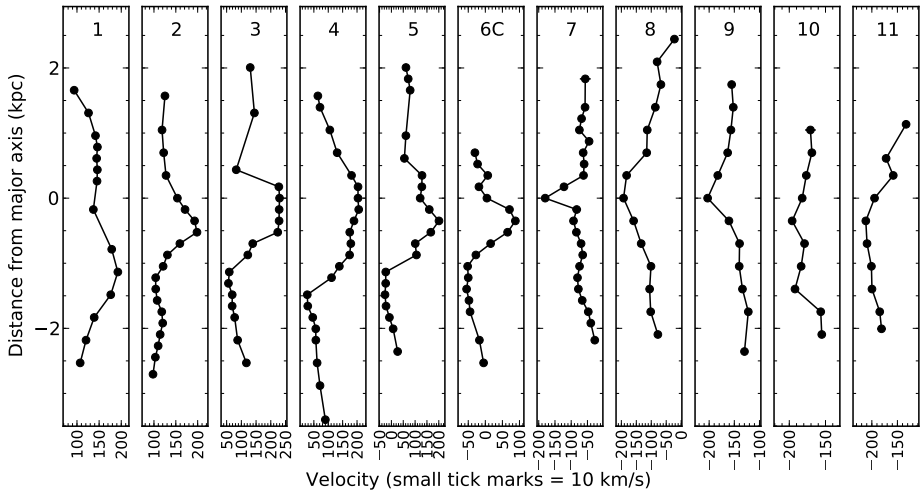

Fig. 5.6.— Multi-long-slit velocities for NGC 3079.

& Hutter (1981) found HI bridge between it and NGC 3627. Radio data indicate it is a starburst galaxy (Condon et al. 1982), and it shows large-scale X-ray outflows, likely driven by supernovae (Dahlem et al. 1996).

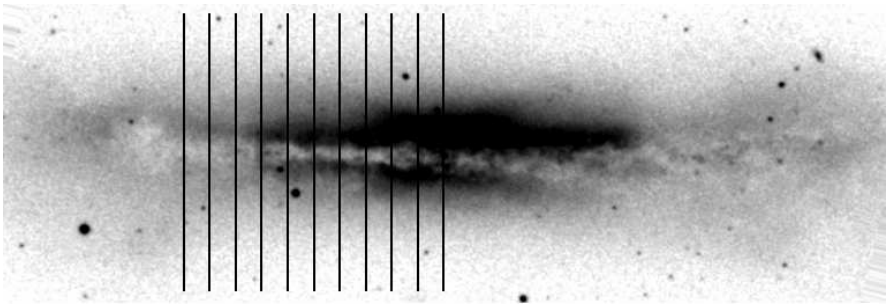

Fig. 5.7.— Slit positions for NGC 3628 overlaid on an image from the Digitized Sky Survey. North is up, and east is to the left. The slits are $4'$ long, which corresponds to 9.0 kpc at a distance of 7.7 Mpc. The west-most slit lies on the center of the galaxy, and the slits are spaced by $22.5''$.

We observed the east, receding side of this galaxy. Our field is shown in Figure 5.7, and our spectrum can be seen in Figure 5.8. We see very bright Hα

emission near the nucleus and strong dust obscuration in the lower half of the galaxy. We detect emission 1 – 2 kpc from the midplane, and our velocity profiles (Figure 5.9) show no lagging feature in the gas. The velocites near the midplane in the central slits show an extreme jump in velocity, and similar to NGC 3079, this can be explained by streaming motions associated with a bar.

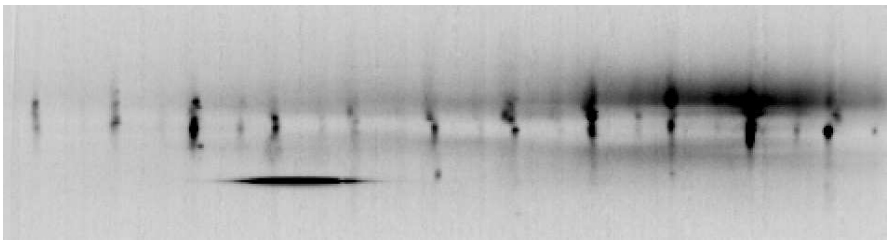

Fig. 5.8.— Multi-long-slit spectrum of NGC 3628. North is up, east is to the left, and wavelength increases to the left. The vertical extent of the spectrum is 5.6 kpc.

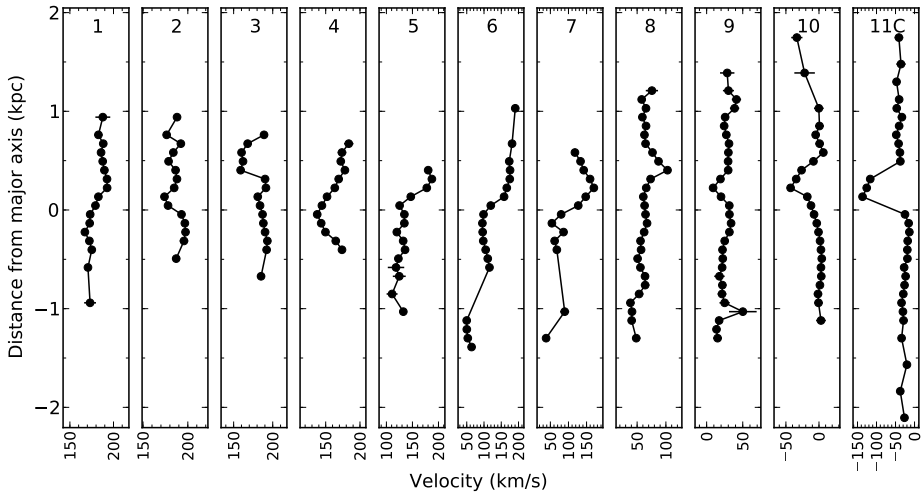

Fig. 5.9.— Multi-long-slit velocities for NGC 3628.

5.5. NGC 4013

Rueff et al. (2013) found large-scale dust features in NGC 4013 almost 2 kpc above the bulge, indicating a thick disk similar to NGC 891. They found no supershell features, so outflows are not likely. This galaxy is part of the Ursa Major group, which does not have a central concentration, and its membership in that group indicates it is relatively isolated. However, Martínez-Delgado et al. (2009) detected a stellar tidal stream around this galaxy, which is likely from a dwarf satellite. It also has a large warp in its HI disk.

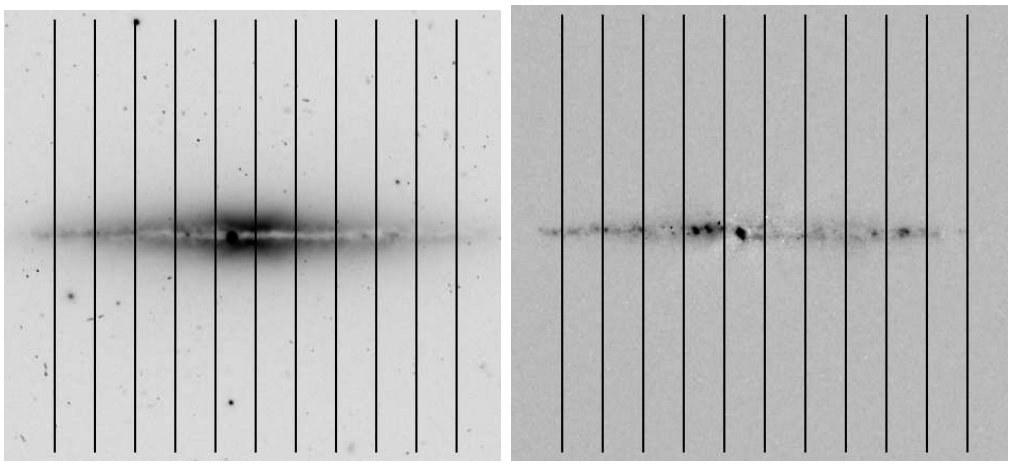

Fig. 5.10.— Slit positions for NGC 4013 overlaid on an R-band image (top) and an Hα image (bottom) from Rand (1996). North is up, and east is to the left. The slits are 4′ long, which corresponds to 19.9 kpc at a distance of 17.1 Mpc. The west-most slit lies on the center of the galaxy, and the slits are spaced by 22.5″.

Howk & Savage (1999b) observed knots of Hα emission in NGC 4013 up to 1 kpc from midplane. Our slit locations and gray scale spectrum are shown in Figures 5.10 and 5.11. Most of the emission we detect is concentrated very close to the midplane, with faint EP gas extending vertically to 1 – 2 kpc on the east side (Figure 5.12. We see no evidence of lagging gas in those slits. On the west

side, we do not see emission beyond 1 kpc from the midplane. Slits 8 and 9 show low velocity peaks in their profiles near the midplane, which are caused by dust obscuration in the disk.

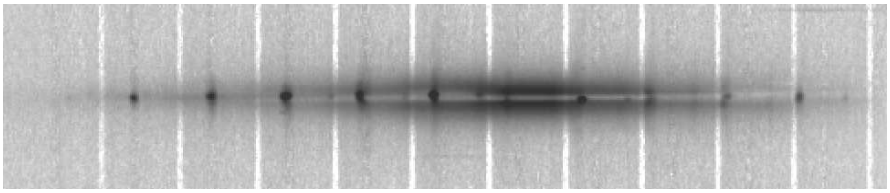

Fig. 5.11.— Multi-long-slit spectrum of NGC 4013. North is up, east is to the left, and wavelength increases to the left. The vertical extent of the spectrum is 10.0 kpc.

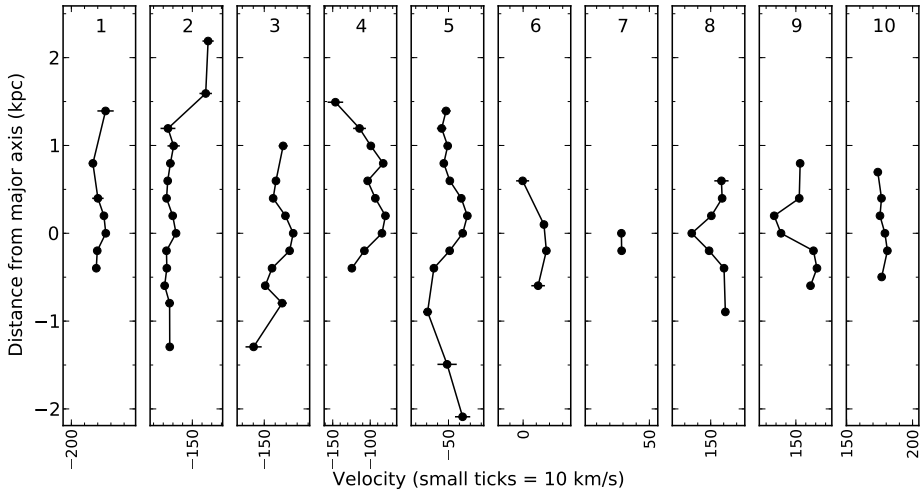

Fig. 5.12.— Multi-long-slit velocities for NGC 4013.

5.6. UGC 4278

UGC 4278 (IC 2233) is a quiescent galaxy with a low surface brightness and a low star formate rate. It has a neighboring galaxy, NGC 2537, but HI data show no evidence that they are connected or interacting (Matthews & Uson 2008), which means this is a fairly isolated galaxy. Our slit positions and mulit-long-slit spectrum are shown in Figures 5.13 and 5.14. We see bright Hα emission near the midplane across our entire field, and we detect emission up to (or beyond) 1 kpc consistently in most of the slits. Our velocity profiles are shown in Figure 5.15. The profiles are extremely regular. We see no signs of dust obscuration and no lagging component. The profiles indicate a slight asymmetry in the rotation curve, as the east side has a rotational velocity of $\sim$90 km s^{-1}, while on the west side it is only $\sim$70 km s^{-1}. The Hα emission extends beyond or field of view, however, especially on the western side, so we might not be observing the maximum rotational speed.

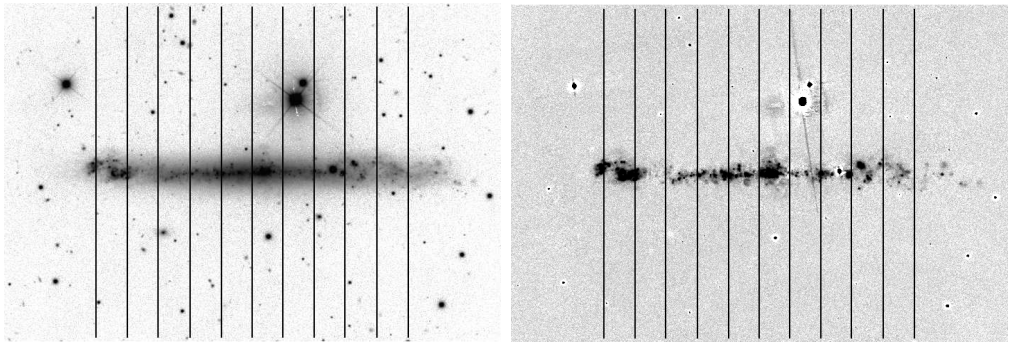

Fig. 5.13.— Slit positions for UGC 4278 overlaid on an Hα KPNO image (Patterson & Walterbos 2013; Patterson 2013) before (top) and after (bottom) continuum subtraction. North is up, and east is to the left. The slits are 4′ long, which corresponds to 15.8 kpc at a distance of 13.6 Mpc. Slit 6 lies on the center of the galaxy, and the slits are spaced by 22.5″.

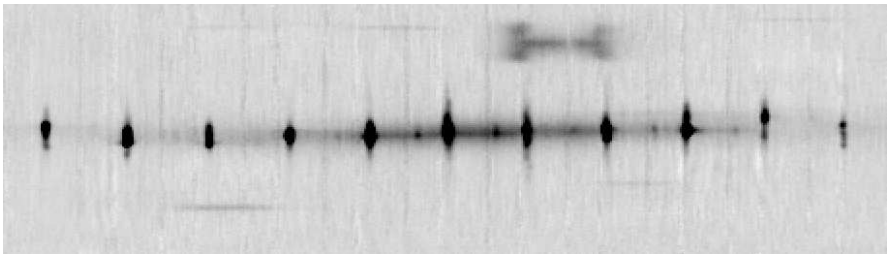

Fig. 5.14.— Multi-long-slit spectrum of UGC 4278. North is up, east is to the left, and wavelength increases to the left. The vertical extent of the spectrum is 10.1 kpc.

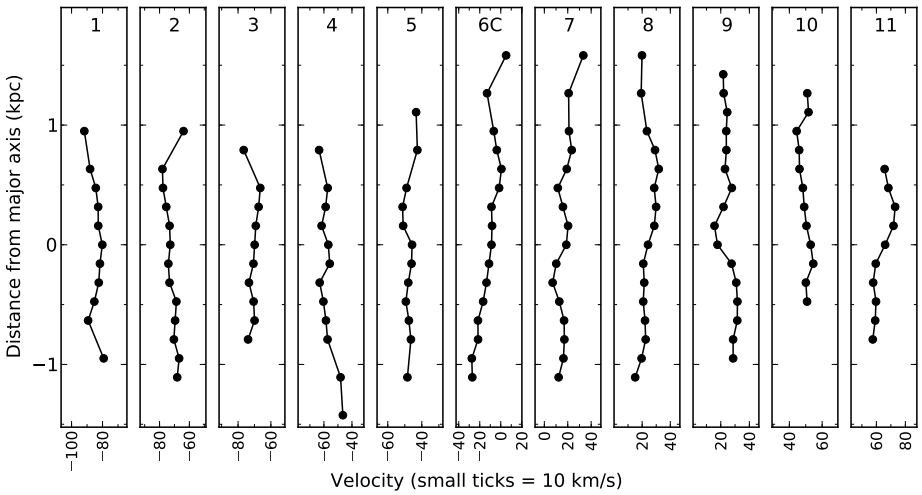

Fig. 5.15.— Multi-long-slit velocities for UGC 4278.

5.7. NGC 5229

NGC 5229 has received very little attention in the literature. Our observing field and gray scale spectrum are shown in Figures 5.16 and 5.17. We do not observe Hα emission in the outer most slits on both sides of the galaxy, and Hα imaging shows no emission outside of our field of view. This puts a radial limit on the extent of the ionized gas of $\pm 1.5'$ (2.2 kpc). The rotation curve indicated by our velocity profiles, which are shown in Figure 5.18, is one that rises to $\sim$50

km s^{-1} in the inner 45″ of the galaxy and remains flat beyond that. It appears fairly symmetric on the approaching and receding halves of the galaxy. Vertically, we see no extended DIG, and we only detect emission up to 0.2 kpc from the midplane.

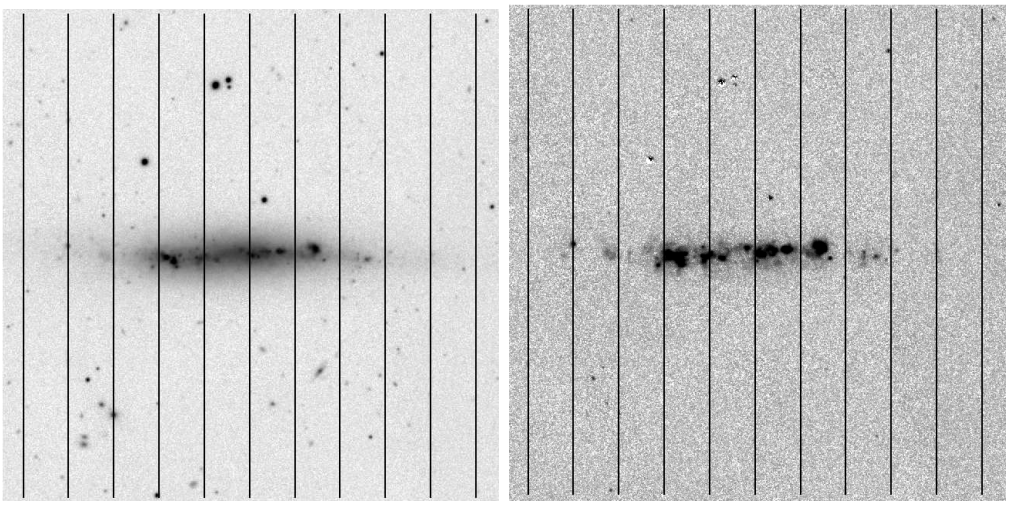

Fig. 5.16.— Slit positions for NGC 5229 overlaid on an Hα KPNO image (Patterson 2013) before (top) and after (bottom) continuum subtraction. North is up, and east is to the left. The slits are 4′ long, which corresponds to 5.9 kpc at a distance of 5.1 Mpc. Slit 6 lies on the center of the galaxy, and the slits are spaced by 22.5″.

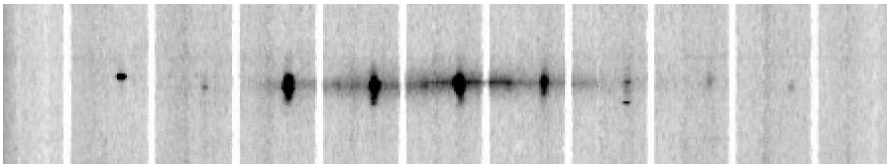

Fig. 5.17.— Multi-long-slit spectrum of NGC 5229. North is up, east is to the left, and wavelength increases to the left. The vertical extent of the spectrum is 2.4 kpc.

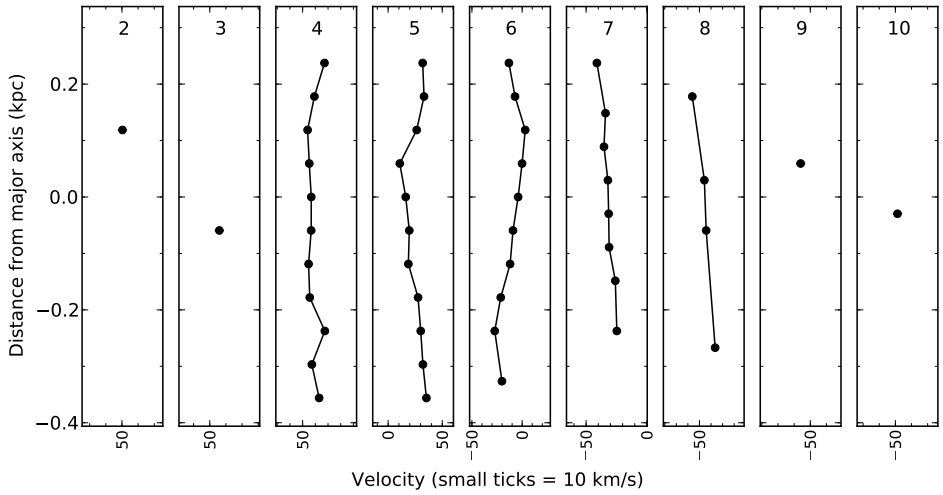

Fig. 5.18.— Multi-long-slit velocities for NGC 5229.

5.8. NGC 4762

NGC 4762 is classified as a lenticular galaxy, and it likely has a bar (Hamabe & Wakamatsu 1989; Wozniak 1995). We detected no Hα emission. Our slit positions are shown on an image from the Digitized Sky Survey in Figure 5.19. Our spectrum is shown in Figure 5.20. Because we did not detect Hα emission, we did not wavelength calibrate the data or perform sky line subtraction.

5.9. UGC 7321

UGC 7321 is classified as a 'superthin' galaxy due to its very flat optical disk. It has no bulge, and it has a low surface brightness. Because it is so thin, it is likely not a very evolved disk. It has a symmetric HI distribution, and its HI disk is warped (Uson & Matthews 2003). Matthews & Wood (2003) found that it is isolated and has a low star formation rate. They also detected a thick HI disk

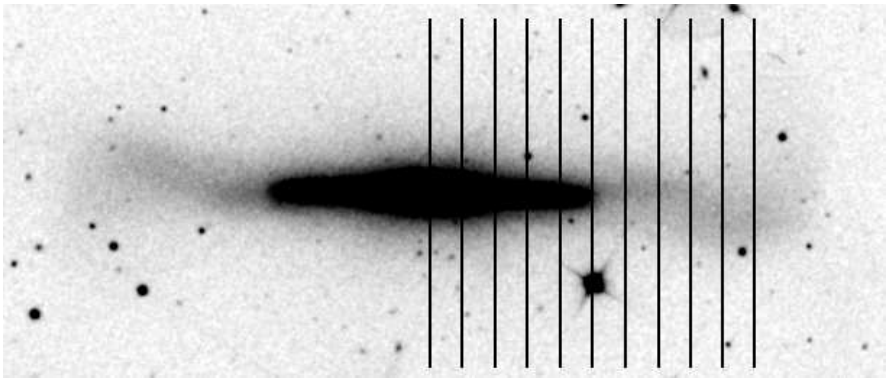

Fig. 5.19.— Slit positions for NGC 4762 overlaid on Digitized Sky Survey image. North is up, and east is to the left. The slits are $4'$ long, which corresponds to 19.5 kpc at a distance of 16.8 Mpc. The eastern most slit lies on the galaxy center, and the slits are spaced by $22.5''$.

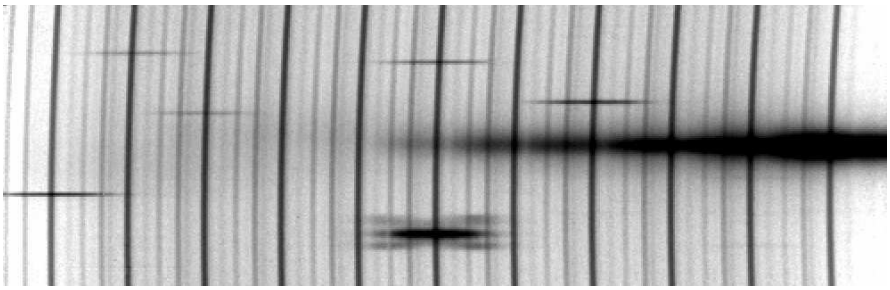

Fig. 5.20.— Multi-long-slit spectrum of NGC 4762. North is up, and east is to the left. Because we detected no Hα emission, we did not wavelength calibrate our data, and wavelength increases to the right in this spectrum. The vertical extent of the spectrum is 15.6 kpc.

that is warped and flared. Both of these studies adopted a distance of 10 Mpc for this galaxy.

Our spectrum and and velocities for UGC 7321 are shown in Figures 5.21 and 5.22. We see Hα in all 11 slits, and the brightness of the emission decreases with radial distance. Vertically, most of the emission we detect is confined to within 0.3 kpc of the midplane. The profiles on both halves of the galaxy show the curved shape that is characteristic of a lagging component. It is a very minor effect in these plots, but it is present in almost all of the slits. This pattern can also arise

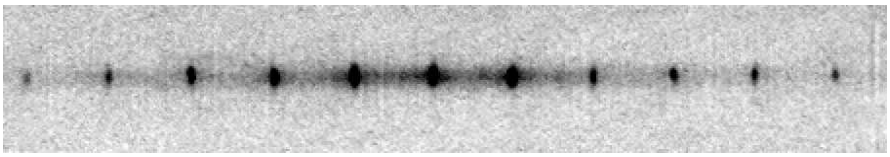

Fig. 5.21.— Multi-long-slit spectrum of UGC 7321. North is up, east is to the left, and wavelength increases to the left. The vertical extent of the spectrum is 4.3 kpc.

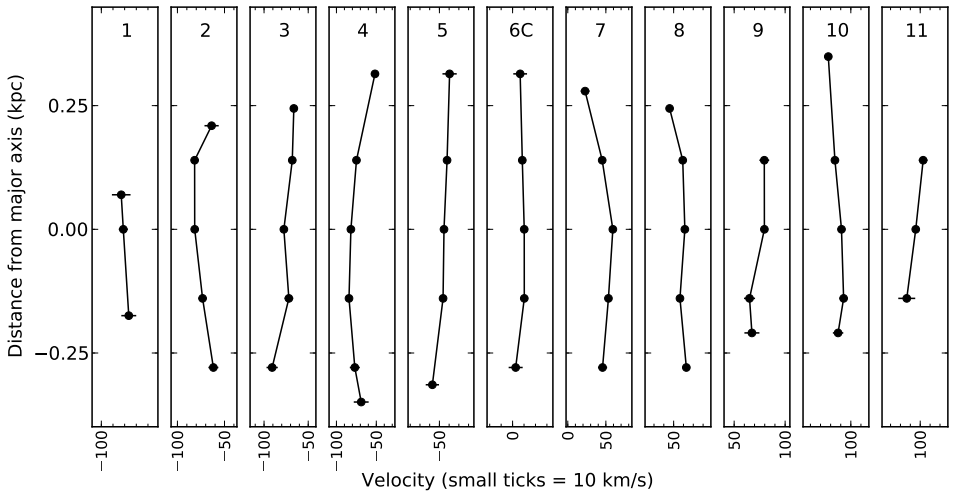

Fig. 5.22.— Multi-long-slit velocities for UGC 7321.

from a thick disk with an inclination slightly less than 90°. The EP gas in this galaxy is not very extended, but it is fairly bright near the midplane. A highly inclined, dense gas disk with a scale height that drops off steeply could explain these profiles.

6. SUMMARY AND CONCLUSIONS

6.1. Summary

We present results for our sample of 13 nearby, edge-on galaxies. The goal of this project was to characterize the kinematics of extraplanar (EP) Hα-emitting gas and determine how common it is for galaxies to have a thick, lagging component of ionized gas. Previous studies of lagging EP gas targeted galaxies with high rates of star formation or galaxies that were supsected to have a lag. Our sample covers a range of star formation rates (L_{FIR}/D_{25}^2 of $0.03 - 8.9 \times 10^{40}$ erg s^{-1} kpc^{-2}) and maximum rotational velocities (55.8 – 244.9 km s^{-1}) and includes active and quiescent galaxies. Previous studies also employed single-slit spectroscopy, a Fabry-Perot, or an Integrated Field Unit for observations. This work introduces another method that is ideal for studying the kinematics of extended objects: multi-long-slit spectroscopy.

Multi-slit spectroscopy has been used to study the kinematics of planetary nebulae and to do blind searches for Lyα emitters. This is the first time this technique has been used to study thick disks of edge-on galaxies. Our setup consists of a slit-mask with 11 uniform, parallel slits. This produces an image with 11 spectra side by side. We use a narrowband filter in series with the mask to isolate our desired Hα line and prevent neighboring spectra from overlapping. The multi-slit aspect of this approach allows us to efficiently measure velocities of the Hα line in a galaxy over a range of galactocentric radii in a single exposure. We can produce deep, 2D velocity maps of our targets in a much shorter time than would be required for a single-slit setup.

Because this is a new technique for this field, we chose two inclined galaxies,

NGC 4559 and NGC 5055, for which we have deep HI data as test galaxies for our observing setup and data reduction processes. We compared our multi-slit Hα velocities to the HI data to show that they are in close agreement.

We also developed our own software to model galaxies specifically for the multi-slit setup. Spectral lines through edge-on disks suffer from projection effects, which affect the shape of the line profiles. Inclination effects can also cause a galaxy to appear to have lagging EP gas when in reality it does not. Both of these effects complicate the analysis of the measured velocity field from our observations. Our models allow us to account for the shape of the profiles and disentangle inclination effects from actual lagging gas.

Additionally, we included NGC 891 in our sample of edge-on galaxies. The EP gas in this galaxy has been studied extensively by several groups in both HI and Hα (e.g. Swaters et al. 1997; Fraternali et al. 2005; Heald et al. 2006; Kamphuis et al. 2007; Oosterloo et al. 2007), and there is a close agreement across their studies concerning the magnitude of its lagging component. The value of the lag we derive from our modeling of this galaxy is in agreement with those studies. In addition to NGC 891, we detect a lag in three of our other target galaxies. Three of our galaxies show non-lagging EP gas, and two galaxies show EP gas with inclination effects and disturbed kinematics. We cannot determine if the gas in those two galaxies is lagging. Three of our galaxies show no EP gas beyond $\sim$1.5 kpc from the midplane, and we detected no Hα gas at all in one of our targets.

6.2. Sample Conclusions

Our sample results are outlined in Table 6.1. We use L_{FIR}/D_{25}^2 as a proxy for star formation rate and v_{rot} as an indication of how massive the galaxy is. We detect a lagging component in four of our galaxies: NGC 891, NGC 4631, NGC 4517, and NGC 4565. NGC 891 is a large galaxy with a relatively high star formation rate. It does not appear to be interacting. We find a lag of 19^{+7}_{-4} km s^{-1} kpc^{-1} in the northwest quadrant and a lag of 15^{+12}_{-2} km s^{-1} kpc^{-1} in the northeast quadrant. The lag appears to be constant with radius. This is consistent with previous studies of NGC 891, which measured lags of 15 – 18 km s^{-1} kpc^{-1} (Heald et al. 2006) and 18.8 km s^{-1} s.h.$^{-1}$ (Kamphuis et al. 2007) in Hα and 20 km s^{-1} kpc^{-1} (Swaters et al. 1997), 15 km s^{-1} kpc^{-1} (Oosterloo et al. 2007), and 15 km s^{-1} kpc^{-1} (Fraternali et al. 2005) in HI. According to Fraternali & Binney (2006), $\sim$80 – 90 % of the EP gas in this galaxy is from galactic fountain flows, and the remaining gas must be from lower angular momentum material in order to match these lag values.

NGC 4631 is a highly interacting galaxy on its east side. We find evidence for a warped spiral arm bent out of the plane of the galaxy in the southeast quadrant. Previous studies suggested that this disturbed area was a large outflow, but our data is the first 2D velocity field of this feature. Our velocities are not consistent with an outflow event. Instead, a warping of the disk is the most likely scenario. A bent disk with an inclination of $\sim$65° on the near side and an inclination of $\sim$85° on the far side would produce the velocity profiles that we see.

The central field of NGC 4631 is also a very active area. We measure an extreme lag in excess of 200 km s^{-1} kpc^{-1} near the center of the galaxy, and

this value decreases with radius toward the west side. The extreme lag can be explained by an outflow event or by the accretion of low angular momentum material, either in place of or in addition to galactic fountain flows. The west field has very regular kinematics and does not appear to be interacting. We measure a constant lag of 6.0 ± 2.5 km s^{-1} kpc^{-1} in the northwest quadrant and a lag of 9.5 ± 3.0 km s^{-1} kpc^{-1} in the southwest quadrant. The lags in the west field can likely be caused by fountain flows alone.

We detect radially shallowing lags in NGC 4517 and NGC 4565. These are both massive galaxies, but NGC 4517 has a high star formation rate, whereas NGC 4565 has a very low star formation rate. The lag we dectect in NGC 4517 is $\sim$50 km s^{-1} kpc^{-1} in the central part of the galaxy and decreases to 0 – 20 km s^{-1} kpc^{-1} in the outer parts. We detect a lag of $\sim$70 km s^{-1} kpc^{-1} in the central area of the east side of NGC 4565, and the value of the lag steadily decreases to 0 as radius increases. The vertical velocity gradients for both of these galaxies indicate that accretion of or interaction with lower angular momentum material in addition to galactic fountain flows is responsible for the origin of the EP gas.

All four galaxies in which we detect a lag are large, massive galaxies and are either interacting or have high star formation rates.

There are three galaxies in which we detect EP Hα emission but no lagging component. NGC 5907 is a fairly isolated galaxy, but its disk is warped and there is a stellar tidal stream surrounding the galaxy, so it has at some point in the past interacted with companion galaxies. NGC 3628, however, is currently an active galaxy. It is an interacting, starburst galaxy with large scale outflows. We detect ionized EP gas, but the gas is not lagging. NGC 4013 has a thick, dusty disk

that has been compared to NGC 891. Similar to NGC 5907, it appears to be a quiescent galaxy, but a stellar tidal stream has been observed around it, and its HI disk is warped.

Four galaxies in our sample show very little or no EP emission. NGC 4762 is a lenticular galaxy, and we detect no Hα emission. NGC 5229 and UGC 7321 have very similar velocity profiles. Neither shows extended DIG more than 0.3 kpc from the midplane. Both are very quiescent and have low star formation rates. We detect Hα emission in UGC 4278 up to 1.5 kpc from the midplane. The velocity profiles are completely straight, showing no signs of lagging, inclination effects, or dust obscuration.

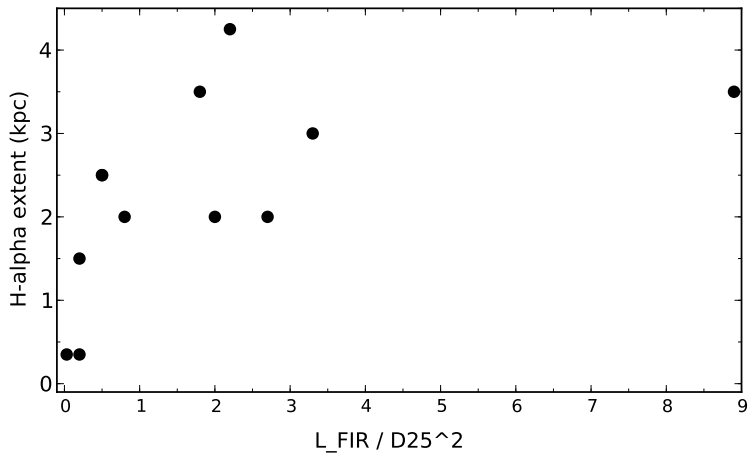

Fig. 6.1.— Hα-extent vs. star formation rate. The units on the x-axis are 10^{40} erg s^{-1} kpc^{-2}.

The remaining two galaxies, NGC 3044 and NGC 3079, have very similar velocity profiles. Both galaxies show inclination effects and Hα emission up to 3 kpc from the disk. NGC 3044 is not an interacting galaxy, but it does have

a relatively high star formation rate. NGC 3079 is highly active and has been classified as a LINER or Seyfert galaxy, and previous studies have shown evidence for outflows. Both galaxies show disturbed kinematics in their velocity profiles. Because our models are simple ones with regular kinematics, we did not model them, and we cannot determine whether there is a lag.

The more active galaxies in our sample, where 'active' means having either a high star formation rate or obvious signs of interactions, show more extended Hα emission. Specifically, we see a trend of increasing Hα extent with increasing star formation rate (Figure 6.1). We also see a similar trend with observed Hα extent increasing as rotational velocity increases (Figure 6.2). Both of these scenarios are consistent with larger, star-forming galaxies posessing strong stellar winds and supernova explosions within the disk, both of which can puff up the EP gas layer and provide an ionization source for the hydrogen gas.

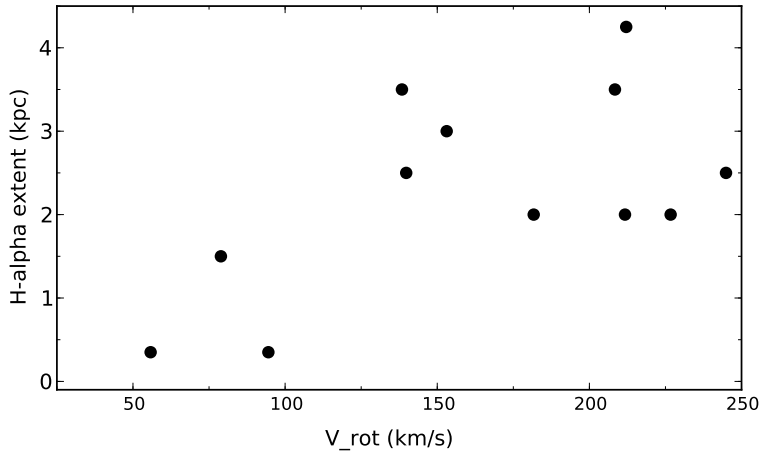

Fig. 6.2.— Hα-extent vs. rotational velocity.

We do not see a connection between galaxy interactions and lagging gas. We also do not see a connection between lagging gas and star formation rate or lagging gas and rotational velocity. The fact that we observe non-lagging EP gas up to 2 kpc from the midplane in three of our galaxies goes against the galactic fountain scenario, which predicts that any EP gas must be lagging the disk in rotation. One potential solution to this problem could be that the EP gas does not start lagging until it rises to greater than 2 kpc from the midplane. Another solution could be that our assumptions about galactic fountain flows are incorrect. Jałocha et al. (2011) modeled galactic fountain flows in four galaxies. They found that changing the mass distribution of the underlying disk affected the lag values their models predicted. Models with a large spheroidal mass component produced smaller lags, while models with a disk-dominated potential yielded larger lags. If our three galaxies with non-lagging EP gas are bulge-dominated, then their EP gas kinematics could potentially be explained by the models by Jałocha et al. (2011). It is possible their models would predict no lagging gas in these galaxies or gas that is lagging by such a small magnitude that it appears to be co-rotating with the disk within our errorbars.

6.3. General Conclusions

Our modeling shows that inclination effects can cause a galaxy to appear to have lagging EP gas even if the gas is not lagging. This is important for studies of edge-on galaxies that include galaxies with inclinations in the ∼85-89° range, especially if those studies have high enough spatial resolution to measure velocities near the midplane of the galaxies. A perfectly edge-on disk with lagging gas can produce observed velocity profiles that are very similar to a somewhat thin disk

inclined at ∼88° with an exponential scale height of ∼500 pc and no lagging gas. The same is true for an even thinner disk inclined at ∼86°.

Additionally, when galaxies have high inclinations but are not exactly edge-on, the velocity profiles from models with and without lagging gas look very similar because the bright midplane gas is dominant over the fainter EP gas. This means that it is very hard to determine whether there is any lagging EP gas, especially in galaxies with thinner EP gas disks.

Another outcome from our study is that we demonstrated the feasibility of using a multi-long-slit setup for studying the kinematics of edge-on and inclined galaxies. Our setup can also be used to measure velocities in other extended objects, such as nebulae. The multi-slit approach allows for deep exposures over a wide spatial area, and a 2D velocity field can be obtained in a much more efficient manner than traditional single-slit spectroscopy.

Table 6.1. Multi-slit Sample Summary

Field	L_{FIR}/D_{25}^2 10^{40} erg s^{-1} kpc^{-2}	v_{rot} km s^{-1}	Hα Extent kpc	Lag km s^{-1} kpc^{-1}	Constant (C) or Radially Decreasing (R)
NGC 891	2.2	212.1	4.25	15, 19	C
NGC 3044	3.3	153.1	3.00	Maybe	
NGC 3079	8.9	208.4	3.50	Maybe	
NGC 3628	2.0	211.7	2.00	0	
NGC 4013	2.7	181.7	2.00	0	
NGC 4517	0.5	139.8	2.50	70	R
NGC 4565 E	0.5	244.9	2.50	70	R
NGC 4565 W			1.75	0	
NGC 4631 E	1.8	138.4	2.75	0	
NGC 4631 C			3.50	150, 140	R
NGC 4631 W			2.25	6.5, 9.0	C
NGC 4762	>0.2	110.0	-	-	
NGC 5229	>0.1	55.8	0.35	-	
NGC 5907	0.8	226.7	2.00	0	
UGC 4278	0.2	78.9	1.50	-	
UGC 7321	0.03	94.5	0.35	-	

REFERENCES

Ajiki, M., et al. 2002, ApJ, 576, L25

Alton, P. B., Xilouris, E. M., Bianchi, S., Davies, J., & Kylafis, N. 2000, A&A, 356, 795

Alton, P. B., Xilouris, E. M., Misiriotis, A., Dasyra, K. M., & Dumke, M. 2004, A&A, 425, 109

Axon, D. J., & Taylor, K. 1978, Nature, 274, 37

Barbieri, C. V., Fraternali, F., Oosterloo, T., Bertin, G., Boomsma, R., & Sancisi, R. 2005, A&A, 439, 947

Barnaby, D., & Thronson, Jr., H. A. 1994, AJ, 107, 1717

Battaglia, G., Fraternali, F., Oosterloo, T., & Sancisi, R. 2006, A&A, 447, 49

Boomsma, R., Oosterloo, T. A., Fraternali, F., van der Hulst, J. M., & Sancisi, R. 2005, A&A, 431, 65

Bregman, J. N. 1980, ApJ, 236, 577

Broeils, A. H., & Sancisi, R. 1985, A&A, 153, 281

Bunker, A. J., Stanway, E. R., Ellis, R. S., McMahon, R. G., & McCarthy, P. J. 2003, MNRAS, 342, L47

Burkhead, M. S., & Hutter, D. J. 1981, AJ, 86, 523

Carozzi-Meyssonnier, N. 1978, A&AS, 33, 237

Chromey, F. R., Elmegreen, D. M., Mandell, A., & McDermott, J. 1998, AJ, 115, 2331

Collins, J. A., Benjamin, R. A., & Rand, R. J. 2002, ApJ, 578, 98

Collins, J. A., Rand, R. J., Duric, N., & Walterbos, R. A. M. 2000, ApJ, 536, 645

Combes, F., & Sanders, R. H. 1981, A&A, 96, 164

Condon, J. J., Condon, M. A., Gisler, G., & Puschell, J. J. 1982, ApJ, 252, 102

Crampton, D., & Lilly, S. 1999, in Astronomical Society of the Pacific Conference Series, Vol. 191, Photometric Redshifts and the Detection of High Redshift Galaxies, ed. R. Weymann, L. Storrie-Lombardi, M. Sawicki, & R. Brunner, 229

Dahlem, M., Dettmar, R.-J., & Hummel, E. 1994, A&A, 290, 384

Dahlem, M., Heckman, T. M., Fabbiano, G., Lehnert, M. D., & Gilmore, D. 1996, ApJ, 461, 724

Dahlem, M., Lisenfeld, U., & Rossa, J. 2006, A&A, 457, 121

de Mello, D. F., Urrutia-Viscarra, F., Mendes de Oliveira, C., Torres-Flores, S., Carrasco, E. R., & Cypriano, E. 2012, MNRAS, 426, 2441

de Vaucouleurs, G., de Vaucouleurs, A., Corwin, H. G., Buta, R. J., Paturel, G., & Fouque, P. 1995, VizieR Online Data Catalog, 7155, 0

de Vaucouleurs, G., de Vaucouleurs, A., & Corwin, Jr., H. G. 1976, Second reference catalogue of bright galaxies. Containing information on 4,364 galaxies with references to papers published between 1964 and 1975.

Dettmar, R.-J. 1990, A&A, 232, L15

Ekers, R. D., & Sancisi, R. 1977, A&A, 54, 973

Ford, H. C., Dahari, O., Jacoby, G. H., Crane, P. C., & Ciardullo, R. 1986, ApJ, 311, L7

Fraternali, F., Binney, J., Oosterloo, T., & Sancisi, R. 2007, New A Rev., 51, 95

Fraternali, F., & Binney, J. J. 2006, MNRAS, 366, 449

—. 2008, MNRAS, 386, 935

Fraternali, F., Oosterloo, T., Sancisi, R., & van Moorsel, G. 2001, ApJ, 562, L47

Fraternali, F., Oosterloo, T. A., Sancisi, R., & Swaters, R. 2005, in Astronomical Society of the Pacific Conference Series, Vol. 331, Extra-Planar Gas, ed. R. Braun, 239

Fraternali, F., van Moorsel, G., Sancisi, R., & Oosterloo, T. 2002, AJ, 123, 3124

Garcia-Burillo, S., Guelin, M., & Neininger, N. 1997, A&A, 319, 450

Gentile, G., et al. 2013, A&A, 554, A125

Golla, G., Dettmar, R.-J., & Domgoergen, H. 1996, A&A, 313, 439

Goudfrooij, P., Strader, J., Brenneman, L., Kissler-Patig, M., Minniti, D., & Edwin Huizinga, J. 2003, MNRAS, 343, 665

Grcevich, J., & Putman, M. E. 2009, ApJ, 696, 385

Haffner, L. M., Reynolds, R. J., Tufte, S. L., Madsen, G. J., Jaehnig, K. P., & Percival, J. W. 2003, ApJS, 149, 405

Haffner, L. M., et al. 2009, Reviews of Modern Physics, 81, 969

Hamabe, M., & Wakamatsu, K.-I. 1989, ApJ, 339, 783

Heald, G., et al. 2011, A&A, 526, A118

—. 2012, A&A, 544, C1

Heald, G. H., Rand, R. J., Benjamin, R. A., & Bershady, M. A. 2006, ApJ, 647, 1018

—. 2007, ApJ, 663, 933

Heckman, T. M. 1980, A&A, 87, 152

Heckman, T. M., Armus, L., & Miley, G. K. 1990, ApJS, 74, 833

Ho, L. C., Filippenko, A. V., Sargent, W. L. W., & Peng, C. Y. 1997, ApJS, 112, 391

Hoopes, C. G., Walterbos, R. A. M., & Rand, R. J. 1999, ApJ, 522, 669

Howk, J. C., & Savage, B. D. 1999a, AJ, 117, 2077

Howk, J. C., & Savage, B. D. 1999b, in The Physics and Chemistry of the Interstellar Medium, ed. V. Ossenkopf, J. Stutzki, & G. Winnewisser, 38

—. 2000, AJ, 119, 644

Hummel, E., & Dettmar, R.-J. 1990, A&A, 236, 33

Irwin, J., et al. 2012, AJ, 144, 44

Irwin, J. A., et al. 2011, MNRAS, 410, 1423

Israel, F. P. 2009, A&A, 506, 689

Jałocha, J., Bratek, Ł., Kutschera, M., & Skindzier, P. 2011, MNRAS, 412, 331

Jarrett, T. H., Chester, T., Cutri, R., Schneider, S. E., & Huchra, J. P. 2003, AJ, 125, 525

Joung, M. R., Putman, M. E., Bryan, G. L., Fernández, X., & Peek, J. E. G. 2012, ApJ, 759, 137

Kamphuis, P., Peletier, R. F., Dettmar, R.-J., van der Hulst, J. M., van der Kruit, P. C., & Allen, R. J. 2007, A&A, 468, 951

Kamphuis, P., et al. 2013, MNRAS, 434, 2069

Kennicutt, Jr., R. C., et al. 2003, PASP, 115, 928

Kewley, L. J., Groves, B., Kauffmann, G., & Heckman, T. 2006, MNRAS, 372, 961

Kodilkar, J., Kantharia, N., & Ananthakrishnan, S. 2008, in Bulletin of the Astronomical Society of India Proceedings, Vol. 25, Bulletin of the Astronomical Society of India Proceedings, 67

Kormendy, J., & Barentine, J. C. 2010, ApJ, 715, L176

Kregel, M., & van der Kruit, P. C. 2004, MNRAS, 352, 787

—. 2005, MNRAS, 358, 481

Laine, S., Appleton, P. N., Gottesman, S. T., Ashby, M. L. N., & Garland, C. A. 2010, AJ, 140, 753

Larson, R. B., Tinsley, B. M., & Caldwell, C. N. 1980, ApJ, 237, 692

Lehner, N., & Howk, J. C. 2011, Science, 334, 955

Lehnert, M. D., & Heckman, T. M. 1996, ApJ, 462, 651

Lockman, F. J. 2004, in Astrophysics and Space Science Library, Vol. 315, How Does the Galaxy Work?, ed. E. J. Alfaro, E. Pérez, & J. Franco, 17

Marinacci, F., Fraternali, F., Nipoti, C., Binney, J., Ciotti, L., & Londrillo, P. 2011, MNRAS, 415, 1534

Martin, C., & Kern, B. 2001, ApJ, 555, 258

Martin, C. L., & Sawicki, M. 2004, ApJ, 603, 414

Martinez-Delgado, D., D'Onghia, E., Chonis, T. S., Beaton, R. L., Teuwen, K., GaBany, R. J., Grebel, E. K., & Morales, G. 2014, ArXiv e-prints

Martínez-Delgado, D., Peñarrubia, J., Gabany, R. J., Trujillo, I., Majewski, S. R., & Pohlen, M. 2008, ApJ, 689, 184

Martínez-Delgado, D., Pohlen, M., Gabany, R. J., Majewski, S. R., Peñarrubia, J., & Palma, C. 2009, ApJ, 692, 955

Matthews, L. D., & Uson, J. M. 2008, AJ, 135, 291

Matthews, L. D., & Wood, K. 2001, ApJ, 548, 150

—. 2003, ApJ, 593, 721

Ménard, B., Scranton, R., Fukugita, M., & Richards, G. 2010, MNRAS, 405, 1025

Miller, S. T., & Veilleux, S. 2003, ApJ, 592, 79

Morrison, H. L., Boroson, T. A., & Harding, P. 1994, AJ, 108, 1191

Neininger, N., & Dumke, M. 1999, Proceedings of the National Academy of Science, 96, 5360

Neininger, N., Guelin, M., Garcia-Burillo, S., Zylka, R., & Wielebinski, R. 1996, A&A, 310, 725

Oosterloo, T., Fraternali, F., & Sancisi, R. 2007, AJ, 134, 1019

Patterson, M. T. 2013, PhD thesis, NEW MEXICO STATE UNIVERSITY

Patterson, M. T., & Walterbos, R. 2013, in American Astronomical Society Meeting Abstracts, Vol. 221

Paturel, G., Petit, C., Prugniel, P., Theureau, G., Rousseau, J., Brouty, M., Dubois, P., & Cambresy, L. 2003, VizieR Online Data Catalog, 7237, 0

Pierce, M. J. 1994, ApJ, 430, 53

Popescu, C. C., Tuffs, R. J., Kylafis, N. D., & Madore, B. F. 2004, A&A, 414, 45

Rand, R. J. 1994, A&A, 285, 833

—. 1996, ApJ, 462, 712

—. 1997, ApJ, 474, 129

—. 1998, ApJ, 501, 137

—. 2000a, ApJ, 535, 663

—. 2000b, ApJ, 537, L13

Rand, R. J., Kulkarni, S. R., & Hester, J. J. 1990, ApJ, 352, L1

—. 1992, ApJ, 396, 97

Rand, R. J., & Stone, J. M. 1996, AJ, 111, 190

Rand, R. J., & van der Hulst, J. M. 1993, AJ, 105, 2098

Reynolds, R. J. 1990, in Lecture Notes in Physics, Berlin Springer Verlag, Vol. 362, Low Frequency Astrophysics from Space, ed. N. E. Kassim & K. W. Weiler, 121–129

Richter, P. 2012, ApJ, 750, 165

Roberts, M. S. 1968, ApJ, 151, 117

Rossa, J., & Dettmar, R.-J. 2000, A&A, 359, 433

Rueff, K. M., Howk, J. C., Pitterle, M., Hirschauer, A. S., Fox, A. J., & Savage, B. D. 2013, AJ, 145, 62

Rupen, M. P., van Gorkom, J. H., Knapp, G. R., Gunn, J. E., & Schneider, D. P. 1987, AJ, 94, 61

Sancisi, R. 1976, A&A, 53, 159

Sancisi, R., & Allen, R. J. 1979, A&A, 74, 73

Sancisi, R., & van Albada, T. S. 1987, in IAU Symposium, Vol. 117, Dark matter in the universe, ed. J. Kormendy & G. R. Knapp, 67–80

Sasaki, T. 1987, PASJ, 39, 849

Schweizer, F. 1979, PASP, 91, 149

Seth, A., Agüeros, M., Lee, D., & Basu-Zych, A. 2008, ApJ, 678, 116

Seth, A. C., Dalcanton, J. J., & de Jong, R. S. 2005, AJ, 129, 1331

Shang, Z., et al. 1998, ApJ, 504, L23

Shapiro, P. R., & Field, G. B. 1976, ApJ, 205, 762

Solomon, P. M., & Sage, L. J. 1988, ApJ, 334, 613

Stockton, A. 1999, Ap&SS, 269, 209

Strickland, D. K., Heckman, T. M., Colbert, E. J. M., Hoopes, C. G., & Weaver, K. A. 2004a, ApJS, 151, 193

—. 2004b, ApJ, 606, 829

Swaters, R. A., Sancisi, R., & van der Hulst, J. M. 1997, ApJ, 491, 140

Taylor, V. A., Jansen, R. A., Windhorst, R. A., Odewahn, S. C., & Hibbard, J. E. 2005, ApJ, 630, 784

Thilker, D. A., Braun, R., Walterbos, R. A. M., Corbelli, E., Lockman, F. J., Murphy, E., & Maddalena, R. 2004, ApJ, 601, L39

Tikhonov, N. A., Galazutdinova, O. A., & Drozdovsky, I. O. 2006, ArXiv Astrophysics e-prints

Tomisaka, K., & Ikeuchi, S. 1988, ApJ, 330, 695

Tran, K.-V. H., Lilly, S. J., Crampton, D., & Brodwin, M. 2004, ApJ, 612, L89

Tüllmann, R., Dettmar, R.-J., Soida, M., Urbanik, M., & Rossa, J. 2000, A&A, 364, L36

Tüllmann, R., Pietsch, W., Rossa, J., Breitschwerdt, D., & Dettmar, R.-J. 2006, A&A, 448, 43

Tully, R. B. 1994, VizieR Online Data Catalog, 7145, 0

Tully, R. B., Rizzi, L., Shaya, E. J., Courtois, H. M., Makarov, D. I., & Jacobs, B. A. 2009, AJ, 138, 323

Uson, J. M., & Matthews, L. D. 2003, AJ, 125, 2455

van der Hulst, J. M., & Sancisi, R. 2005, in Astronomical Society of the Pacific Conference Series, Vol. 331, Extra-Planar Gas, ed. R. Braun, 139

van der Hulst, J. M., Terlouw, J. P., Begeman, K. G., Zwitser, W., & Roelfsema, P. R. 1992, in Astronomical Society of the Pacific Conference Series, Vol. 25, Astronomical Data Analysis Software and Systems I, ed. D. M. Worrall, C. Biemesderfer, & J. Barnes, 131

van der Kruit, P. C., & Searle, L. 1981a, A&A, 95, 105

—. 1981b, A&A, 95, 116

Veilleux, S., Cecil, G., Bland-Hawthorn, J., Tully, R. B., Filippenko, A. V., & Sargent, W. L. W. 1994, ApJ, 433, 48

Vogler, A., & Pietsch, W. 1996, A&A, 311, 35

Vogler, A., Pietsch, W., & Kahabka, P. 1996, A&A, 305, 74

Wakker, B. P., & van Woerden, H. 1997, ARA&A, 35, 217

Walton, D. J., Gladstone, J. C., Roberts, T. P., Fabian, A. C., Caballero-Garcia, M. D., Done, C., & Middleton, M. J. 2011, MNRAS, 414, 1011

Wang, Q. D., Walterbos, R. A. M., Steakley, M. F., Norman, C. A., & Braun, R. 1995, ApJ, 439, 176

Wannier, P., & Wrixon, G. T. 1972, ApJ, 173, L119

Weliachew, L. 1969, A&A, 3, 402

Weliachew, L., Sancisi, R., & Guelin, M. 1978, A&A, 65, 37

Wilson, O. C. 1958, Reviews of Modern Physics, 30, 1025

Wilson, O. C., Minich, G., Flather, E., & Coffeen, M. F. 1959, ApJS, 4, 199

Wozniak, H. 1995, Astrophysical Letters and Communications, 31, 165

Yamasaki, N. Y., Sato, K., Mitsuishi, I., & Ohashi, T. 2009, PASJ, 61, 291

Yim, K., Wong, T., Xue, R., Rand, R. J., Rosolowsky, E., van der Hulst, J. M., Benjamin, R., & Murphy, E. J. 2014, ArXiv e-prints

Zschaechner, L. K., Rand, R. J., Heald, G. H., Gentile, G., & Józsa, G. 2012, ApJ, 760, 37

Zschaechner, L. K., Rand, R. J., Heald, G. H., Gentile, G., & Kamphuis, P. 2011, ApJ, 740, 35